SMALL HELIUM-COOLED INFRARED TELESCOPE EXPERIMENT

FOR SPACELAB-2

(IRT)

Contract NAS8-32845

Final Report

For the period 3 October 1977 through 31 December 1988

Principal Investigator

Dr. Giovanni G. Fazio

March 1990

Prepared for
National Aeronautics and Space Administration
NASA Marshall Space Flight Center
Huntsville, Alabama 35812

Smithsonian Institution
Astrophysical Observatory
Cambridge, Massachusetts 02138

The Smithsonian Astrophysical Observatory
is a member of the
Harvard-Smithsonian Center for Astrophysics

The NASA Technical Officer for this contract is Mr. Tom R. Smith, JA53, National Aeronautics and Space Administration Marshall Space Flight Center, Huntsville, Alabama 35812.

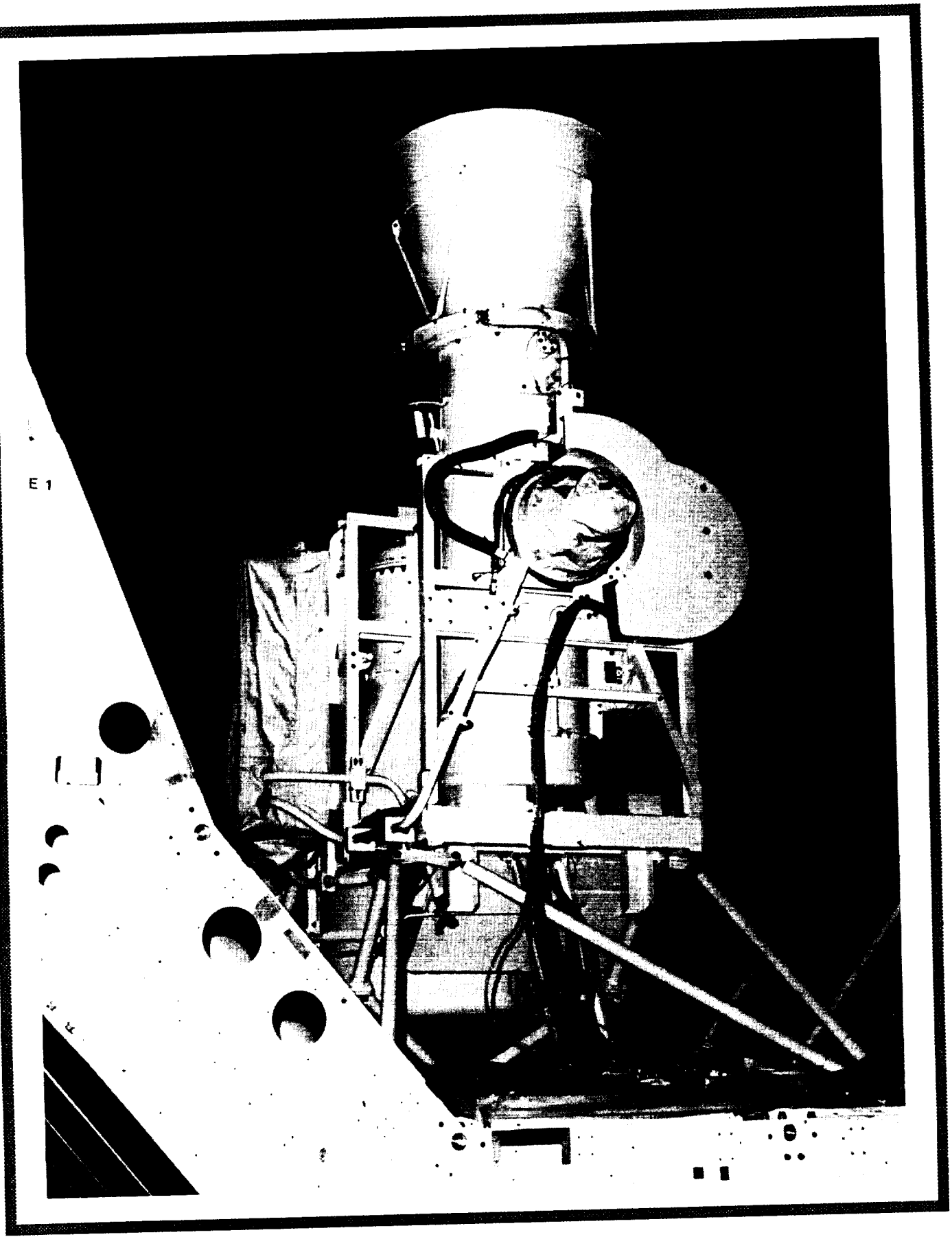

The Spacelab-2 Infrared Telescope

Abstract

The Infrared Telescope (IRT) experiment, flown on Spacelab-2 in July/August 1985, was used to make infrared measurements between 2 μm and 120 μm. The objectives were multidisciplinary in nature with astrophysical goals of mapping the diffuse cosmic emission and extended infrared sources and technical goals of measuring the induced Shuttle environment, studying properties of superfluid helium in space, and testing various infrared telescope system designs.

Astrophysically, new data were obtained on the structure of the Galaxy at near-infrared wavelengths. A summary of the large-scale diffuse near-infrared observations of the Galaxy by the IRT is presented, as well as a summary of the preliminary results obtained from this data on the structure of the galactic disk and bulge. The importance of combining CO and near-infrared maps of similar resolution to determine a three-dimensional model of galactic extinction is demonstrated. The IRT data are used, in conjunction with a proposed galactic model, to make preliminary measurements of the global scale parameters of the Galaxy.

During the mission substantial amounts of data were obtained concerning the induced Shuttle environment. Information was gathered about the gaseous and particulate matter from outgassing, thrusters, water dumps, etc. An experiment was also performed to measure spacecraft glow in the infrared region of the spectrum.

The management in zero-gravity of superfluid helium with a porous plug functioned as planned including experiments in control of the system above the lambda point.

CONTENTS

FIGURES

TABLES

Page

SPACELAB-2 INFRARED TELESCOPE (IRT)

FINAL REPORT

JANUARY 1990

1. INTRODUCTION

The Spacelab-2 Infrared Telescope (IRT) experiment was a joint program by the Smithsonian Astrophysical Observatory (SAO), the University of Arizona (UA), and the NASA Marshall Space Flight Center (MSFC) with additional support from the NASA Ames Research Center (ARC) for the purposes of studying the induced environment. The objectives were multidisciplinary in nature with astrophysical goals of mapping the diffuse cosmic emission and extended infrared (IR) sources and technical goals of measuring the induced Shuttle environment, studying properties of superfluid helium in space, and testing various approaches to IR telescope system designs. Ten IR detectors covering six broad spectral bands from 2 to 120 μm were used. The telescope was mounted in a cryostat which was scanned from side to side in the payload bay. A stationary 250-liter dewar adjacent to the cryostat held the superfluid helium. Cold vapor and liquid were separated by a porous plug in a "transfer assembly" mounted on top of the dewar. A spiral vapor line and ferrofluidic seal connected the stationary dewar to the scanning cryostat.

The IRT experiment was flown on the Spacelab-2 mission in July 1985. Maps of the galactic center and the first quadrant of the galactic plane at 2 μm were obtained with greater sensitivity, angular resolution, and positional accuracy than previously published. In the 7 μm band, a map of the Cygnus region was obtained. These results will yield new information on the stellar structure of our Galaxy.

During the mission substantial amounts of data were obtained concerning the induced Shuttle environment. Information was gathered about the gaseous and particulate matter from outgassing, thrusters, water dumps, etc. The measured environment may be representative of what may also be expected for the manned Space Station. An experiment was also performed to measure spacecraft glow in

the IR. These measurements were important because they defined the environment expected for future astronomical telescopes on the Shuttle as well as the Space Station.

The management in zero-G of superfluid helium with a porous plug functioned as planned and experiments to control the system above the lambda point were highly successful. These liquid helium measurements were important for the design of future IR telescopes in space.

Part way through the mission a strip of mylar, which served as a thermal baffle in the telescope cover cavity, was scorched by overexposure to the sun and cracked during cover actuation. Ripped loose from its moorings as a result of the crack, this strip found its way into the aperture of the telescope during some observations. The 100 μm data were an unequivocal indicator of the mylar strip position. Those times when the mylar strip was in the beam have been identified and the effects on the IR signal determined. The 2 μm data were unaffected but the intermediate wavelength bands were saturated by emission from the mylar strip. An additional baseline shift at 100 μm when the mylar strip was not in the beam was also seen except during two short intervals. This was later determined to be due to the radiation from the 50K upper telescope tube scattering into the beam. Even for those times on each day of the mission when the mylar strip was not in the beam, the intermediate wavelength bands remained saturated as a result of the induced Shuttle environment.

This report is the final report under contract NAS8-32845. Instrument development took place during the period from 1977 to 1984. From 1984 until launch on 25 July 1985 the instrument underwent extensive testing, and from the end of the mission in August 1985 until the middle of 1988 data from the mission were reduced and analyzed.

2. EXPERIMENT DESCRIPTION

2.1 Experimental Objectives

Ground-based IR astronomical observations are severely limited by atmospheric absorption and emission as well as by thermal emission from the telescope mirror. It is virtually impossible to perform measurements of low surface brightness IR emission from ground-based observatories, although discrete sources have been observed successfully from the ground by judicious selection of bandpasses and chopping of the signal against adjacent portions of the sky. Observations from a space platform have the virtue of no atmospheric effects and permit the telescope mirror to be cooled, but other problems become significant. In the case of the Shuttle and its payload, local IR background radiation can be generated due to the release of gases and particulates from the pressurized cabin, the Orbiter surfaces, fuel cell purges, flash evaporators and thrusters, and from the payload and any of its effluents. Even if these sources can be made insignificant, the ultimate limit is set by the zodiacal light resulting from scattered and radiated emission from the interplanetary dust. The purpose of this experiment in addition to its astrophysical goals was to evaluate the induced background of the Orbiter-Spacelab configuration and measure the zodiacal emission. The potential sources of background are thermal emission from local particles and molecular line emission, principally water vapor and carbon dioxide. These line emission spectra are shown in Figure 1. Assuming that the column density of water can be kept to 10^{12}mol/cm^2 and that of carbon dioxide to 10^{11}mol/cm^2 the zodiacal background will be dominant. Figure 1 also shows the anticipated spectrum of the zodiacal light contribution for scattered and emitted light. The amount due to scattered sunlight has included the contribution from galactic starlight. The zodiacal thermal emission is also shown assuming a $1/\lambda$ emissivity dependence. An analysis and discussion of the sources of gases and particulates from the Orbiter is presented in great detail by Simpson and Witteborn (1977; 1978). In particular, they described the micrometeoroid-cratering mechanism for producing particles from the Orbiter tiles and gave total expected particle sighting frequencies and ambient gas pressure. To evaluate these sources it is necessary to have a cold telescope capable of measuring absolute fluxes. The background emission from a telescope with a mirror cooled to 8K is also shown in Figure 1.

In addition to the IR background produced by the induced environment, another concern is the buildup of contaminants on the low-emissivity cold surfaces, which would limit the useful observing time. The emissivity can increase by about 0.1 for each of the first few microns of water deposited. This buildup, due

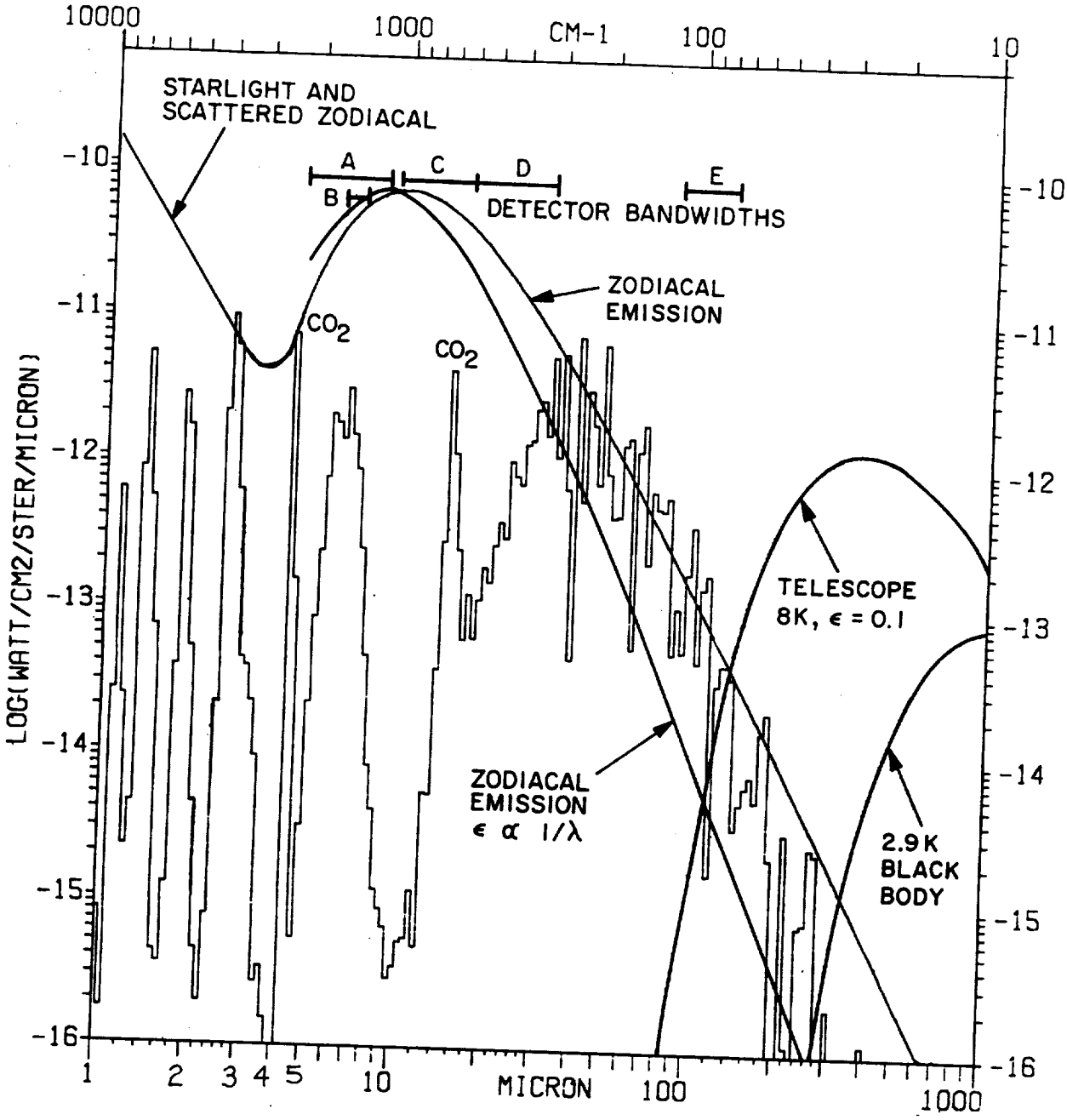

Figure 1. Emission Spectrum from 10^{11} mol/cm^2 of CO_2 (two peaks indicated) and 10^{12} mol/cm^2 of H_2O (remaining peaks) assuming a 300K vibration-rotation temperature for a 5800K solar spectrum and 246K earth. The zodiacal light curves are for a direction 90 degrees from the sun in the ecliptic. The scattered light curve assumes a 5800K blackbody and a dilution factor of 7.8×10^{-14}. The zodiacal emission assumes a 300K blackbody and a dilution factor of 6×10^{-11}. The emission assuming a $1/\lambda$ dependence is also shown. The contribution from galactic starlight has been included in the scattered light curve. The cosmic and telescope background are also indicated.

to the return flux of gases, can be kept insignificant if the column density of all gases is kept to less than 10^{12}mol/cm^2.

The ultimate limit to the background is set by the zodiacal light resulting from scattered and radiated emission from the interplanetary dust.

The original scientific objectives as set forth in December 1976 were:

1. measurement and mapping of diffuse IR radiation from the Galaxy;

2. measurement of diffuse IR emission from intergalactic material, and integrated emission from distant galaxies and QSO's;

3. measurement of the zodiacal light emission;

4. measurement of a large number of discrete IR sources which will overlap with the results of the Infrared Astronomy Satellite (IRAS).

The original technological objectives were:

5. to determine the effects of the induced Shuttle environment (e.g., H_2O, CO_2, particulates, etc.) on the performance of cooled IR telescopes;

6. to prove out the design of a cooled IR telescope that can be applied to larger scale instruments for the Shuttle (e.g., design of a shield or cover for a cooled telescope, and protection of cooled optics against condensates);

7. to demonstrate the performance of a large superfluid helium dewar system and measure certain properties of superfluid helium in space.

Over the time span from the inception of the experiment until launch, additional objectives evolved. These included:

8. search for spacecraft glow in the IR;

9. search for variability in IRAS sources;

10. provide absolute photometric measurements of the cosmic IR background using a cold shutter for reference;

11. map the zodiacal light in the IR at angles other than 90 degrees from the sun;

12. measure fluxes from sources that were saturated for IRAS.

2.2 Telescope Design Consideration

In designing an instrument to make absolute background measurements, it was found prudent to choose a highly baffled Herschelian telescope. This was to provide adequate off-axis rejection of scattered and diffracted radiation. It was also desirable to obtain as much sky coverage as quickly as possible with the system. The minimum time required to map a large portion of the sky is dictated by the orbital period of 92 minutes. In this period a 90-degree band centered on the orbit plane or 60% of the sky exclusive of the sun can be scanned. By rolling the Orbiter to +20 degrees from the local vertical, 75% of the sky can be scanned in one mission. The instrument mounting is illustrated in Figure 2, where V is the velocity vector and the payload +Z-axis is in the direction of the local vertical when the IRT is scanning. To provide rapid redundant coverage not only were data to be taken on contiguous orbits for each of the three roll attitudes (+20, 0 and −20), but the scan rate and field of view were chosen to insure overlapping of scans. The Orbiter pitch rate of four degrees per minute, telescope scan rate of six degrees per second, scan length of 90 degrees, and detector geometry resulted in scanning all accessible areas of the sky (for zero roll) an average of 3.4 times on each orbit, with small regions being scanned as many as six times. For the ±20 degree roll attitudes, the overlap is even greater. The focal-plane geometry used to accomplish this is shown in Figure 3. The overlapping scans, contiguous orbits, and distribution of the various roll attitudes a number of times throughout the mission were to provide redundancy in the data on time scales of minutes, hours, and days.

In order to make a true IR background map, all discrete sources must be identified and removed. Besides cosmic IR sources whose celestial positions will remain fixed, it was also desirable to discriminate between local dust, which would have a large spectrum of angular velocities and not be seen in redundant scans or contiguous orbits and asteroids and whose celestial positions would vary over the mission. To eliminate the possibility of electronic transients mimicking a signal

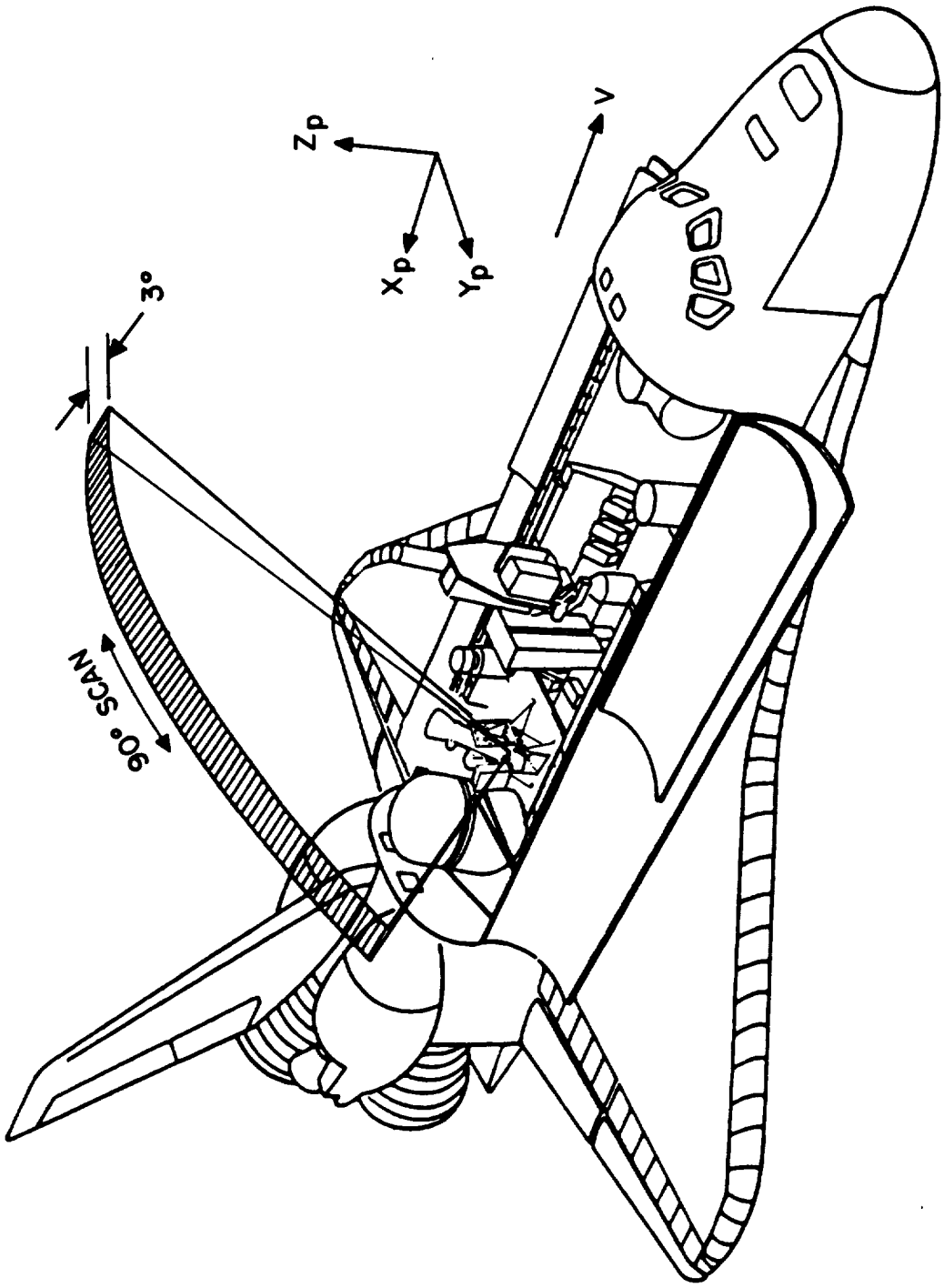

Figure 2. Telescope scan pattern in relation to the Spacelab

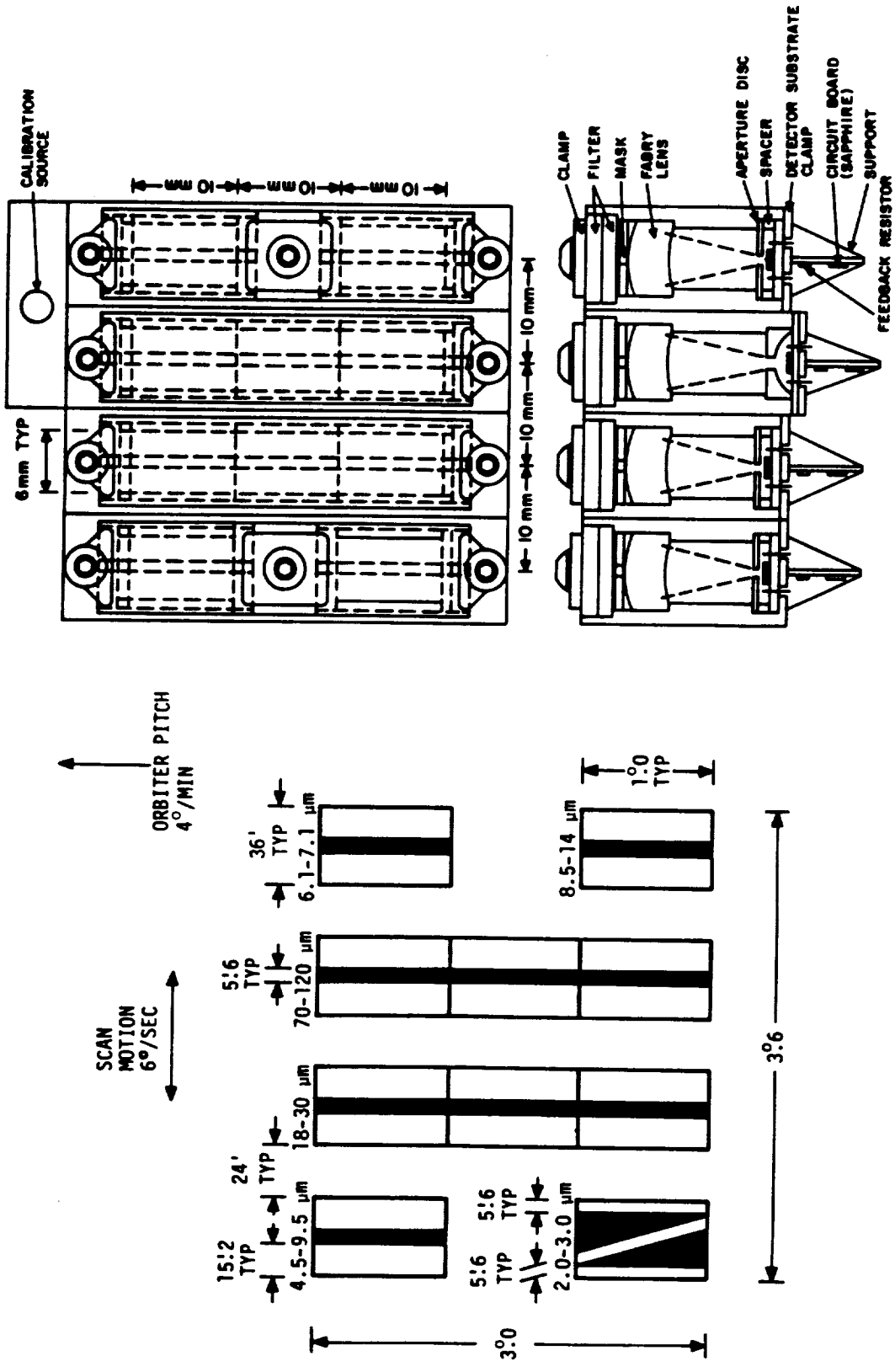

Figure 3. Projection of the focal plane onto the sky. The masks, bandwidths, sizes, and orientation of the ten detectors are shown on the left. The mechanical layout of the components is shown on the right.

from a discrete source, the IR signal was spatially chopped by masking the focal plane (see Figure 3). Thus a discrete cosmic source should appear "on" for 42 msec, "off" for 16 msec, then "on" again for 42 msec.

The selection of the detector bandpass widths was based upon the available detector types, the requirement to evaluate the induced environment, and our objective, the requirement to make astrophysically meaningful observations. The particular bands chosen are given in Table 1. Several of these were similar to IRAS bands (Low 1979). As illustrated in Figure 1, water could be unambiguously detected by comparing the flux in the 6–7 micron band due to the strong ν_2 vibration-rotation fundamental at 6.3 microns with the overall flux in the 4.5 and 9.5 micron band. Also, the E-band was to be very sensitive to the water vapor rotational emission lines. The ν_2 vibration-rotation lines of carbon dioxide occur just short of 15 microns and a band from 8.5–14.5 microns (half power points) was used for identifying any excessive amounts of this molecule. The D- and E-bands were chosen because of their potentially exciting astrophysical significance. The complete set of bands permits spectral measurement; hence, color temperature determination of IR sources roughly from 50K to 500K. To establish the absolute flux of the low surface brightness of the IR background, a cold shutter was moved in front of the focal plane at various times throughout the mission to verify the zero reference of the detectors.

2.3 Hardware Description

The IRT can be divided into several hardware components, shown in a cross sectional view of the instrument in Figure 4. The major components were the focal-plane assembly, telescope, dewar, transfer assembly, cryostat, scan drive, and electronics assemblies.

Table 1. Infrared Detector Bands

Band	$\Delta\lambda$ (μm)	Effective $\lambda^{\dagger}$ (μm)	Pseudonym	Material	Quantity	IRAS Equivalent
S	1.7–3.0	2.15	2 μm	Si:Ga	1	
A	4.5–9.5	7.5	7 μm	Si:Ga	1	
B	6.1–7.1	6.6		Si:Ga	1	
C	8.5–14	11.1		Si:Ga	1	12 μm Band
D	18–30	22.7	23 μm	Si:Sb	3	25 μm Band
E	77–115	91	100 μm	Ge:Ga	3	100 μm Band

$\Delta\lambda$ Wavelength range between half power points of effective filter transmission curve, including spectral characteristics of detectors, blockers, and optics.

† Assumed 300K blackbody; except for 2 μm band, assumed 5500K.

2.3.1 Focal-Plane Assembly

The focal-plane assembly consisted of the detector block shown in Figure 3, which contained the various detectors and their load resistors, bandpass filters, Fabry lenses, and aperture stops. A cold finger attached to the detector block was used to maintain the detectors at 3K. Helium gas flowing through the cold finger was used as the coolant. A shutter maintained at 8K and a heater to anneal the detectors after exposure to large radiation doses due to passage through the South Atlantic Anomaly (SAA) were provided.

The detectors (See Young *et al.* 1981 for a detailed evaluation of their performance) were photoconductive devices with NEP's less than the background NEP except for the S-band, which was originally to be used only as an aspect sensor, but was eventually used to make 2 μm maps. The characteristics of the various detectors are given in Table 2. The long wavelength E-band detectors were placed in integration cavities to improve their efficiency. Each detector output was fed into a JFET preamp operated in the balanced-DC-TIA mode. The electrical power for the JFET's was derived from isolated lithium batteries. The JFET's were cooled to 70K. The effective capacitance of about 0.02 pF

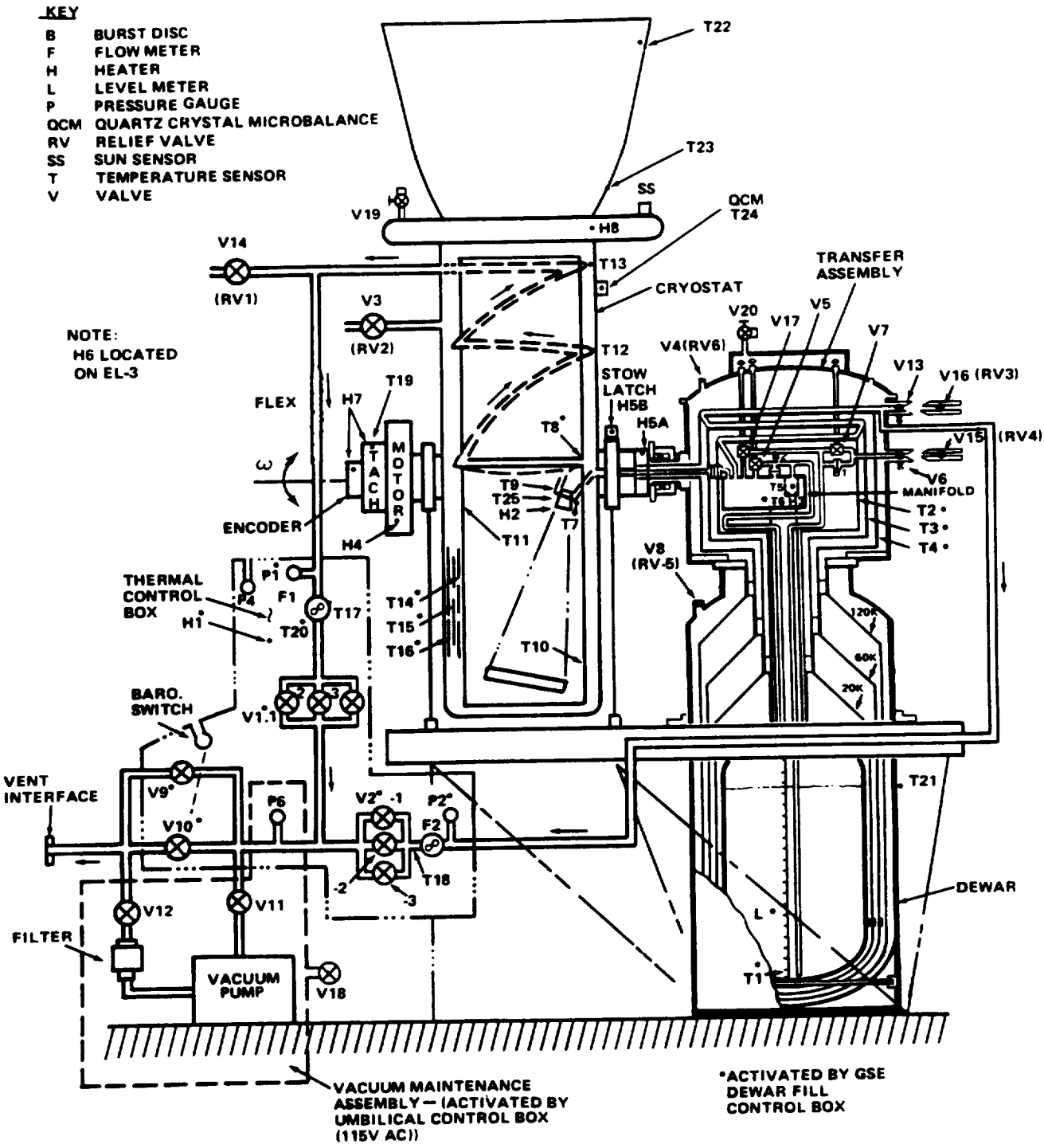

Figure 4. Cryogenic system layout of the IRT

Table 2. Characteristics of Spacelab-2 IR Telescope Detector Channels

Band	V_B (Volts)	S (A/W)	η (%)	ϵ (%)	R_f (Ω)	Q (W)	NEP_Q ($W/Hz^{1/2}$)	NEP_D ($W/Hz^{1/2}$)	NEFD (W/cm^2 μm $Hz^{1/2}$)
S	22	0.03	6	70	1.7×10^{10}	1.2×10^{-13}	$8.\times10^{-16}$	3×10^{-15}	2.4×10^{-17}
A	14	0.45	40	50	$3.\times10^{9}$	2.4×10^{-12}	$8.\times10^{-16}$	5×10^{-16}	1.8×10^{-18}
B	14	0.45	40	70	1.7×10^{10}	4.4×10^{-13}	3.6×10^{-16}	2×10^{-16}	2.9×10^{-18}
C	19	0.85	45	70	$9.\times10^{8}$	4.7×10^{-12}	$9.\times10^{-16}$	5×10^{-16}	1.3×10^{-18}
D	4	1.4	60	40	$3.\times10^{9}$	1.7×10^{-12}	3.4×10^{-16}	2×10^{-16}	4.0×10^{-19}
E	0.15	3	3	50	$3.\times10^{9}$	3.7×10^{-14}	1.5×10^{-16}	7×10^{-17}	3.4×10^{-20}

V_B detector bias voltage

S detector responsivity in the spectral band, 1 – 100 Hz

η detector quantum efficiency in the spectral band

ϵ optical efficiency

R_f feedback resistor

Q background flux (zodiacal) incident on the detector – zodiacal thermal emission has been taken to be zodiacal background at 2.5×10^{-6} $B_\lambda(230)/\lambda(\mu)$ W/cm^2 ster μ, zodiacal background at 2.5 μm to be 10^{-11} W/cm^2 ster μ

NEP_Q background limited NEP

NEP_D zero-background NEP, 1 – 100 Hz

NEFD noise equivalent spectral flux density, background limited

and load resistances on the order of 10^9 to 10^{10} ohms resulted in time constants of approximately 20 – 200 microseconds. This permitted reduction of the instantaneously rising saturated pulses due to energetic particles to the noise level within a few sample periods. During data reduction these spikes were readily identified and removed without severely affecting the deadtime or requiring baseline restoration because of their rapid rise and small full width at half maximum (FWHM).

Fabry lenses of 10-mm focal length were utilized so that the detectors could be only 2.5 mm square and yet have a 0.6 by 1.0 degree field of view. These lenses also insured that the detectors only viewed the single cold mirror, which in turn only viewed the sky, without any obscuration. The mask which provided spatial filtering for source discrimination was evaporated directly onto the lenses. The lenses with high indices of refraction to control aberration were made from

either optical-grade germanium or silicon with an extremely small focal ratio, an f-number of 0.8. The lenses were anti-reflection coated. Bandpasses were determined with multilayer interference filters, and additional blocking was accomplished with crystalline elements. A single aspect sensor sensitive in the 2.0–3.0 micron region with a Z-slit mask was used to obtain absolute aspect information.

The layout of the focal plane was dictated by our need for complete coverage in the two longer wavelength bands and our requirement that the two bands used for detection of water scan the same track on the sky. The off-axis distortions, image quality, and aspect accuracy permitted us to achieve a resolution of a few arcminutes in the scan direction.

A shutter cooled to 8K which covered the entire focal plane when closed provided a zero flux reference. A solenoid was used to pull it into position and a return spring pulled it away. A redundant means for removing the shutter from the field of view was provided by use of a much more powerful solenoid, although this was not used during the mission. A pulsed hot wire bilevel calibration source provided scattered radiation from the back side of the shutter when it was closed, and a commandable heater element attached to the detector block permitted annealing of the detectors after passage through the SAA.

2.3.2 Telescope

The telescope shown in Figure 4 was an f/4 15.2-cm diameter highly baffled telescope of the Herschelian type. The off-axis paraboloid mirror was made of aluminum and was gold coated to provide an emissivity near 0.1. The aperture was protected by a specular sunshade. The basic requirement imposed on a satellite sunshade is to reject light from the sun, earth, and moon. Free-flying telescopes can be held with one side towards the sun and a truncated shade can be used (see, for example, Lemke 1981 or Low 1979). In this way the far edge of the shade would always be below the horizon provided by the near edge and never illuminated. On Spacelab the sun could be incident from any side, thus a truncated shade could not be used for the IRT and the sun could shine onto the inside of the shade when it was less than 90 degrees off axis. For a cooled telescope, there was an additional requirement that the shade not produce an unacceptable thermal load on the telescope (cryostat). Thus, a specular sunshade with low emissivity was chosen. The geometries of the sunshade, telescope, and payload envelope were interrelated and the constraints were the following:

1. The length of the 8K telescope section was governed by the focal length of 61 cm.

2. The 8K telescope section must not see the sunshade or any other surface warmer than 60K.

3. The sunshade must prevent the 60K section from being directly illuminated while providing the minimum avoidance angle consistent with all other requirements.

4. The complete assembly must not violate the Orbiter payload envelope at any scan angle.

5. The moment of inertia (hence sunshade mass) must be kept as small as possible to limit the peak power required to reverse the scan.

The final design met these constraints with a sun avoidance angle of 35 degrees and a thermal load onto the upper telescope section of about 1.3 watts. To minimize the weight of the shade, it was fabricated of fiberglass honeycomb. Cooling the upper telescope section to 60K limited the thermal load onto the lower section and mirror to a few milliwatts. The lower telescope section and mirror were cooled to 8K so as not to be a significant source of background. Having achieved the proper thermal design of the telescope, the optical design was analyzed by the Breault Research Organization for scattered and diffracted radiation, which was exceedingly important in the IR. The APART (Arizona Paraxial Analysis of Radiation Transfer) program was used to analyze the scattered radiation and the Perkin Elmer program GUERAP II (General Unwanted Energy Rejection Analysis Program) was used to analyze diffraction effects. For a discussion of these analysis techniques, see the SPIE Proceedings 107 *Stray-Light Problems in Optical Systems* (1977), in particular the papers by Lange *et al.* (1977) and by Boyce (1977). The telescope sections were made of aluminum with the upper section highly baffled to inhibit reflection of off-axis radiation onto the lower 8K section. Both sections used Martin Marietta Black surfaces to reduce scattered light. The point source transmittance (PST) was calculated at five wavelengths, accounting for both scatter and diffraction, and the results for 6.5 and 120 microns are shown in Figure 5. Additional analysis was also carried out to demonstrate that the much less intense but extended sources, namely, the earth and Orbiter surfaces, were also adequately attenuated.

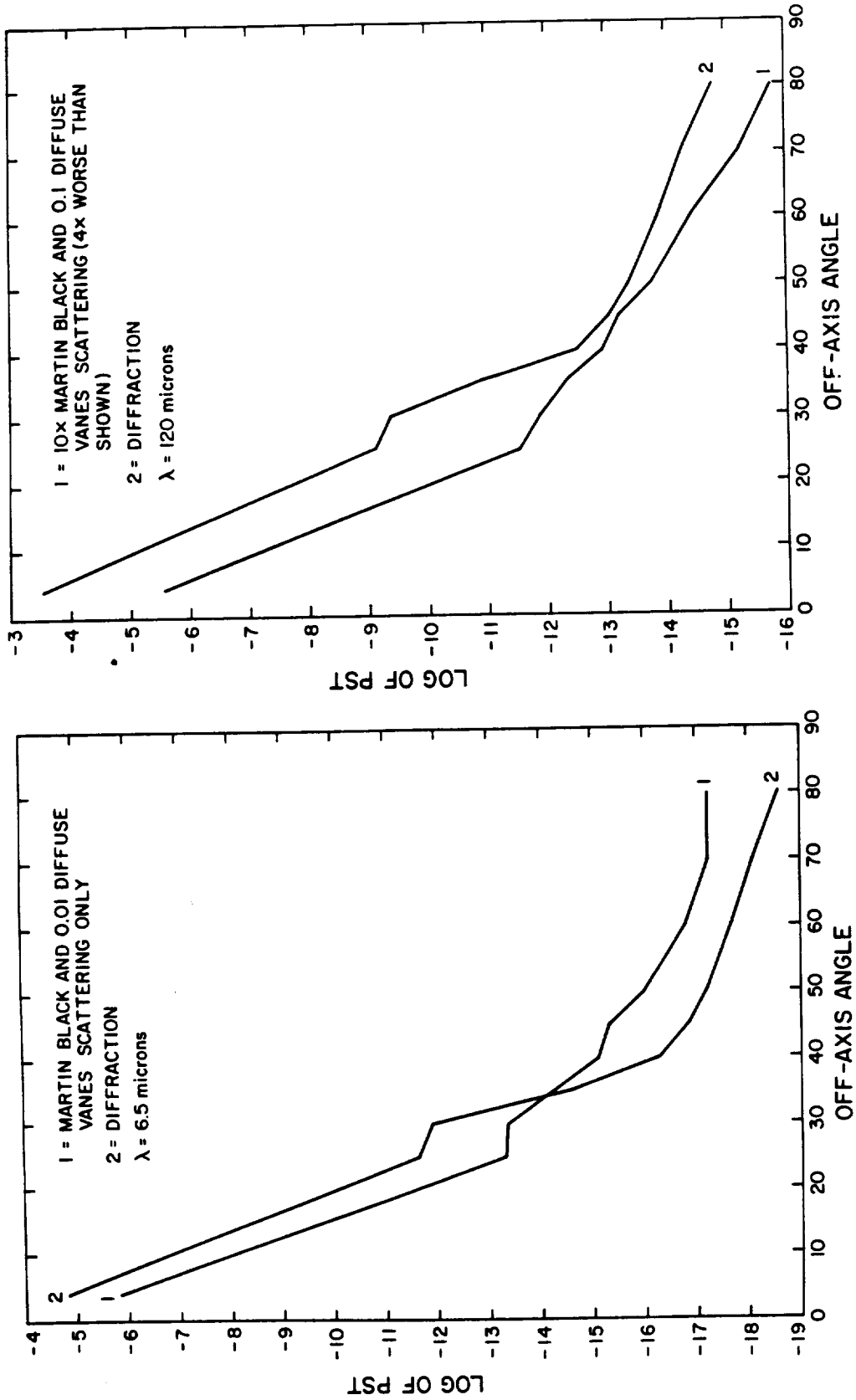

Figure 5. Point source transmittance (PST) at 6.5 μm and 120 μm based on results from the APART scattered light program and the GUERAP II diffracted light program

An independent stray light calculation since the mission has verified that all sources of non-astronomical radiation are substantially below that measured by IRAS for the sky background (Dinger 1986).

2.3.3 Dewar and Transfer Assembly

The design of the dewar and transfer assembly are discussed in detail by Urban *et al.* (1979). These components are shown in cross section in Figure 6. The dewar was a slightly modified design of a conventional 250-liter dewar with vapor-cooled shields and contained the supply of superfluid helium. The helium holdtime was anticipated to be in excess of 30 days. The transfer assembly permitted management of the helium coolant. The separation of liquid and vapor was accomplished with a porous plug (Urban *et al.* 1975). The helium was then divided between two gas lines, one to the dewar's vapor-cooled shields, the other to the cold finger and cryostat's vapor-cooled shields. Both lines had proportional valves to regulate the flow. During ground operation, a standard rotary vane pump was used to maintain continuous pumping on the superfluid helium. This pump flew with the experiment inside of its own sealed box to prevent any leakage of oil from the pump. At T−30 minutes before launch the pump was shut down and the vent lines sealed. As the Orbiter rose in altitude, a baroswitch reopened the vent line when the ambient pressure dropped to five torr (about T+2 minutes). During on-orbit operation, as additional cryostat cooling was required, the flow to the dewar was restricted, which then permitted additional heat input to the liquid helium. Filling of the dewar and pumping of the helium to the superfluid state was accomplished through the transfer assembly. Prior to moving from the Operations and Checkout (O&C) building at KSC, the dewar was filled with normal liquid helium so that the system would remain cold throughout the ground processing of the payload. On the pad, the dewar was refilled and then the liquid converted to superfluid at T−48 hours, just prior to closeout of the payload bay. The connection between the transfer assembly, which was fixed with respect to Spacelab, and the cryostat-telescope, which rotates, was accomplished with a commercially available ferrofluidic seal consisting of a ferrofluid constrained by permanent magnets. This device provided a high vacuum, low friction rotary seal. The gas line from the plug to the cold finger had several helical turns in it to accommodate the 90-degree rotation of the telescope.

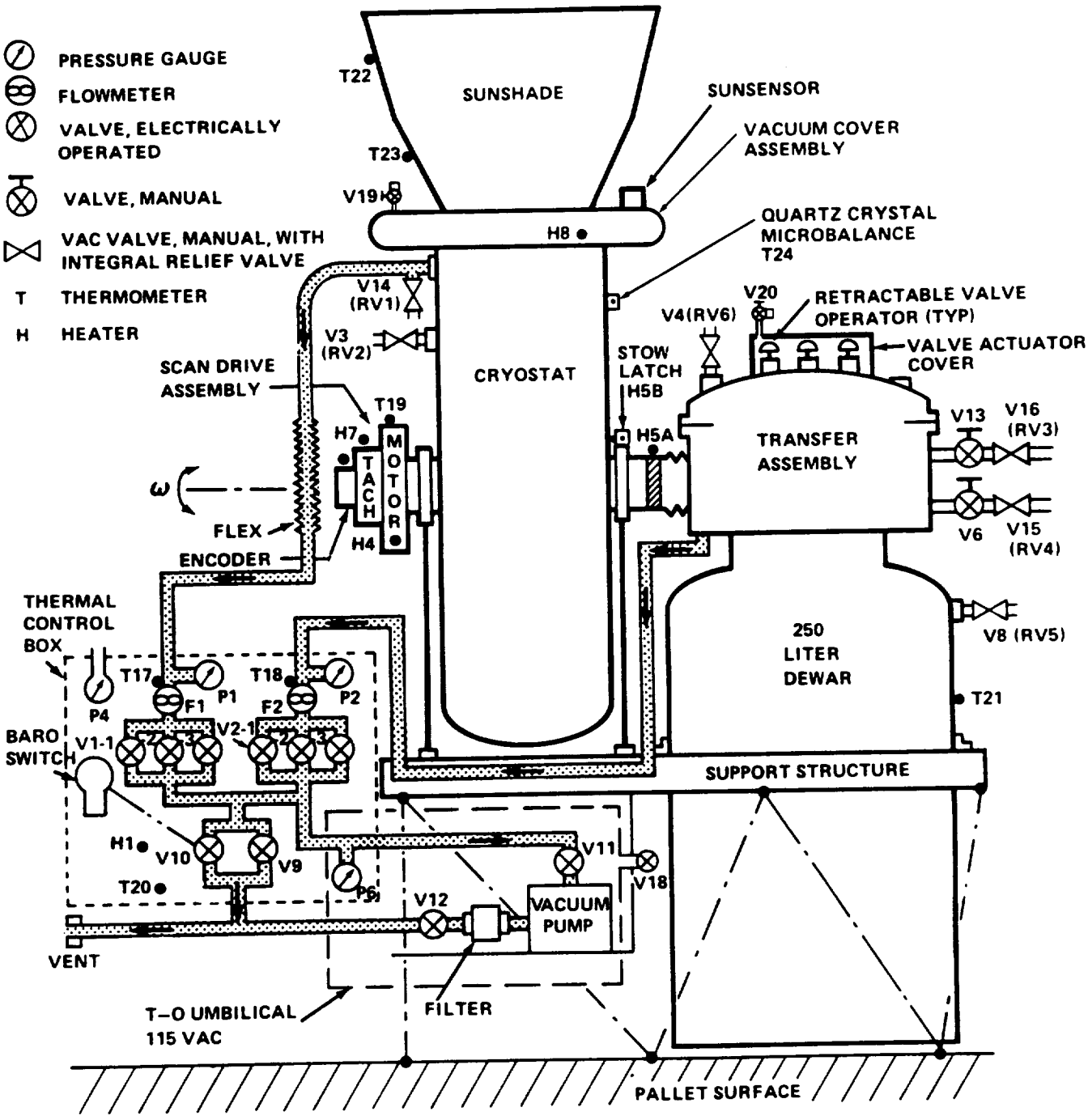

Figure 6. Overall system layout of the IRT

2.3.4 Cryostat

The cryostat contained the telescope and provided the mechanical mounting for the sunshade, the cold finger for cooling of the detector block, and cold rings for mounting of the upper and lower telescope sections. It is also described by Urban *et al.* (1979). The cryostat was a vacuum-jacketed container with several layers of vapor-cooled shields and multilayer insulation. The cold rings provided the heat transfer from the telescope. Gaseous helium from the porous plug flowed through the helical coil directly to the cold finger; then to the 8K cold ring for cooling of the lower telescope and 8K shield; then to the 60K cold ring for cooling of the upper telescope and 60K shield; then to a 120K shield; then to a fourth shield at 240K; and finally out of the cryostat at ambient temperature to the proportional valves.

A vacuum cover sealed the cryostat so that a vacuum could be maintained in the telescope while the telescope was cooled for ground operations. The cover was commanded open or closed during on-orbit operations. In particular, the cover was closed during Orbiter water dumps and burns of the Orbiter Maneuvering Subsystem (OMS) as well as other times when the attitudes precluded taking of IR data. A separate latch mechanism to unseal and reseal the cover was actuated only at the beginning and end of the mission. The vacuum cover was not actively cooled but had an insulated low-emissivity inside surface so that when closed, and after an initial radiative cooling period, it would not present a significant thermal load to the 8K telescope section. The cold shutter was closed to protect the detectors whenever the cover was closed. Separate one-time-only pyrotechnique sealed devices for unlatching and opening of the cover were provided for backup but were never needed.

2.3.5 Scan Drive System

The scan drive system provided continuous uniform back-and-forth scanning of the telescope at ± 6 deg/sec ($\pm 1\%$) about a single axis which was nominally parallel to the Orbiter X-axis (see Figure 2). The scan rate was maintained with a tachometer-torque motor servo loop. In addition a "scan hold," i.e., a zero rate of less than $\pm .0025$ deg/sec, was provided. The zero rate was necessary to ensure sun avoidance. Nominally the system scanned between 45 and 135 degrees from the Y-axis (± 45 degrees from the vertical); however, the scan could be shortened at either end independently with a resolution of 1/128 of the 90-degree arc. This was accomplished by comparing the value of the desired turnaround point with the

output of the shaft angle encoder. When the turnaround was triggered, first a zero rate was sent to the tachometer control loop for the torque motor to stop the scan and then the six deg/sec rate was sent for driving in the opposite direction. The turnaround including settling time was accomplished within 1.5 seconds and the overshoot beyond the turnaround point was less than one degree. The shaft encoder provided 12 bits of resolution over the 90-degree scan for later use in data analysis. In addition to the shaft encoder, position switches were located at the 45-, 90- (vertical) and 135-degree points. These were for use in a backup mode should the encoder, comparator, or serial commanding of the scan limits fail to work. The default startup was in the backup mode with a 45-to-135-degree scan. The three position switches also permitted selection of $45-90$ and $90-135$ degree scans. Thus there was still some degree of flexibility even in the backup mode. The scan drive consumed about 25 watts average between turnarounds and about 120 watts during a turnaround. This depended somewhat on the stiffness of the plumbing and electrical lines which could change as the ambient temperature varied throughout each orbit. A retractable pin was used to lock the telescope position for launch and landing.

2.3.6 Electronics Assemblies

There were three types of electrical interfaces with Spacelab: the Electrical Power Distribution Subsystem (EPDS) for power to the experiment, the Remote Acquisition Unit (RAU) for commanding and low-rate data from the experiment, and the High Rate Multiplexer (HRM) for high rate science data. A general block diagram of the overall electronics is given in Figure 7. The EPDS provided raw unregulated +28 VDC power. All motors, valves, and heaters were run directly off of the raw DC. All electronics were run from regulated and filtered DC-DC converters that were part of the experiment.

The RAU was used for communicating with the instrument but did not handle the detector data. The RAU could send and receive both discrete and serial commands and messages and receive analog levels. The composite data rate for all users of the RAU was 51.2 kbps. The IRT required four serial and 32 discrete command lines and two each 1024 kHz and 4 Hz clocks from the RAU, along with one serial, 16 discrete and 32 analog data lines to the RAU. The data to the RAU was available in real time to both the onboard payload specialist and to the investigators in the Payload Operations Control Center (POCC). These data provided adequate information for successful operation of the experiment even if the detector data had become inaccessible during the mission. The commands and

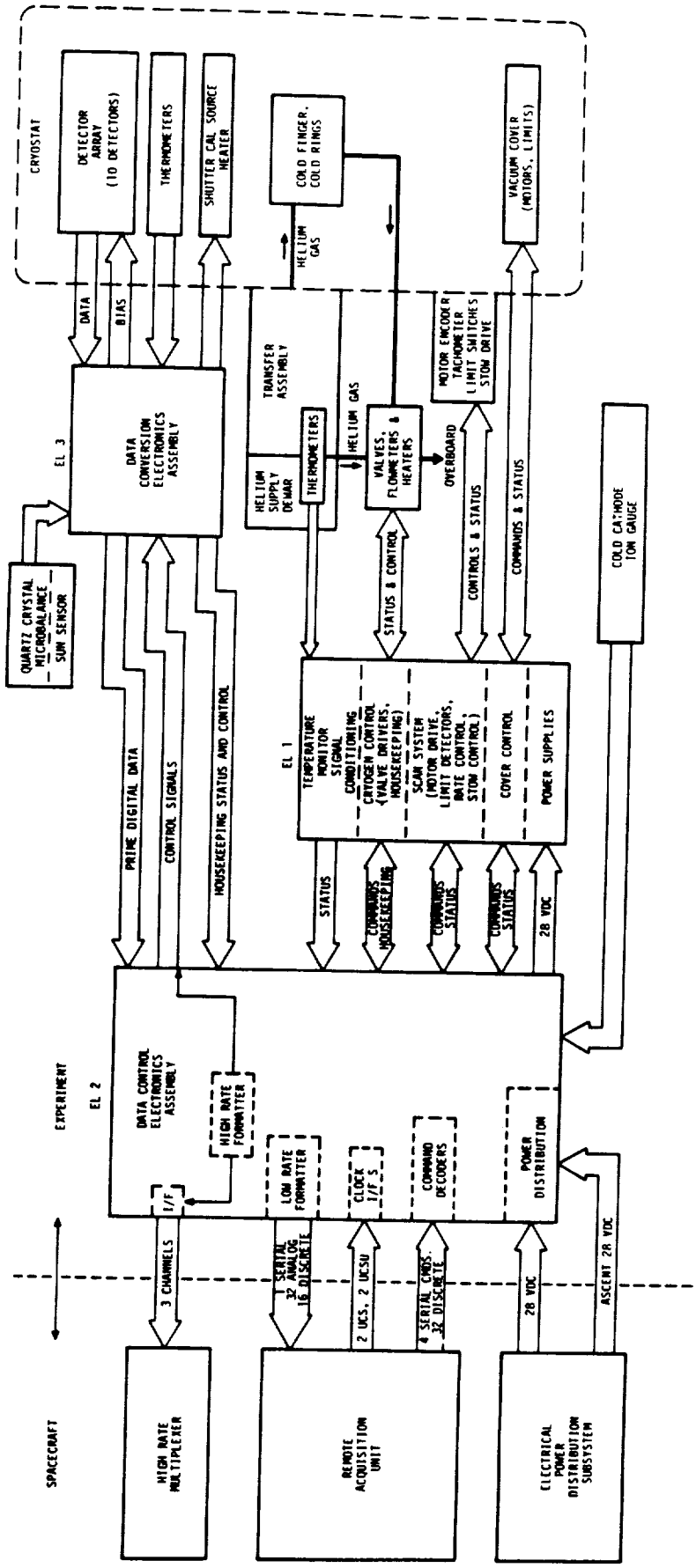

Figure 7. General block diagram showing IRT major electronic functions

data to the experiment had their origin from a number of sources. The discrete and one of the serial commands were sent by the investigators from the POCC. As the need arose, some of the same commands were issued by the payload specialist from the Orbiter aft flight deck during los of signal (LOS). The discrete and serial commands provided operation of the valves and heaters for cryogen management, control of the scan drive, cryostat cover, focal-plane shutter, calibration source, and override of the sun sensor. The sun sensor was hardwired to stop the scan and close the cover and shutter if any Orbiter maneuver caused the telescope to inadvertently scan toward the sun. A second serial command was used to define the scan limits. Normally these limits were computed in real time on board by the Experiment Computer Applications Software (ECAS) for either the primary or backup scan modes and sent to the experiment. The scan limits could also be sent from the POCC. The third and fourth serial messages contained Greenwich Mean Time (GMT) and the Orbiter attitude and position both of which came from Orbiter services. These latter two messages were merged in the instrument with the scientific data stream so that the scientific data was completely self-contained.

The HRM received the scientific data from the instrument. Three channels were used each at a data rate of 204.8 kHz. The conversion electronics that generated this stream is shown schematically in Figure 8. The signal from each of the ten detectors was fed into a set of preamps. To obtain an overall dynamic range of one million (i.e., 20-bit resolution) without requiring state-of-the-art digitization, the preamps provided three output gains. Thus, with 12-bit resolution the noise level was digitized for any signal level. The preamps also provided an absolute value flag for the lowest amplitude signal to allow for the small DC-offset characteristics of the detectors and preamps. The preamp outputs fed into thirty boxcar integrators which had about a one millisecond integration time. These were sequentially multiplexed into sample and holds before being reset. The output of each sample and hold was digitized with a 12-bit analog-to-digital converter to which a parity bit was added. The digitized signal was formatted along with the GMT, Orbiter attitude and position, the output of the shaft angle encoder, and housekeeping status bits, and transmitted via the HRM.

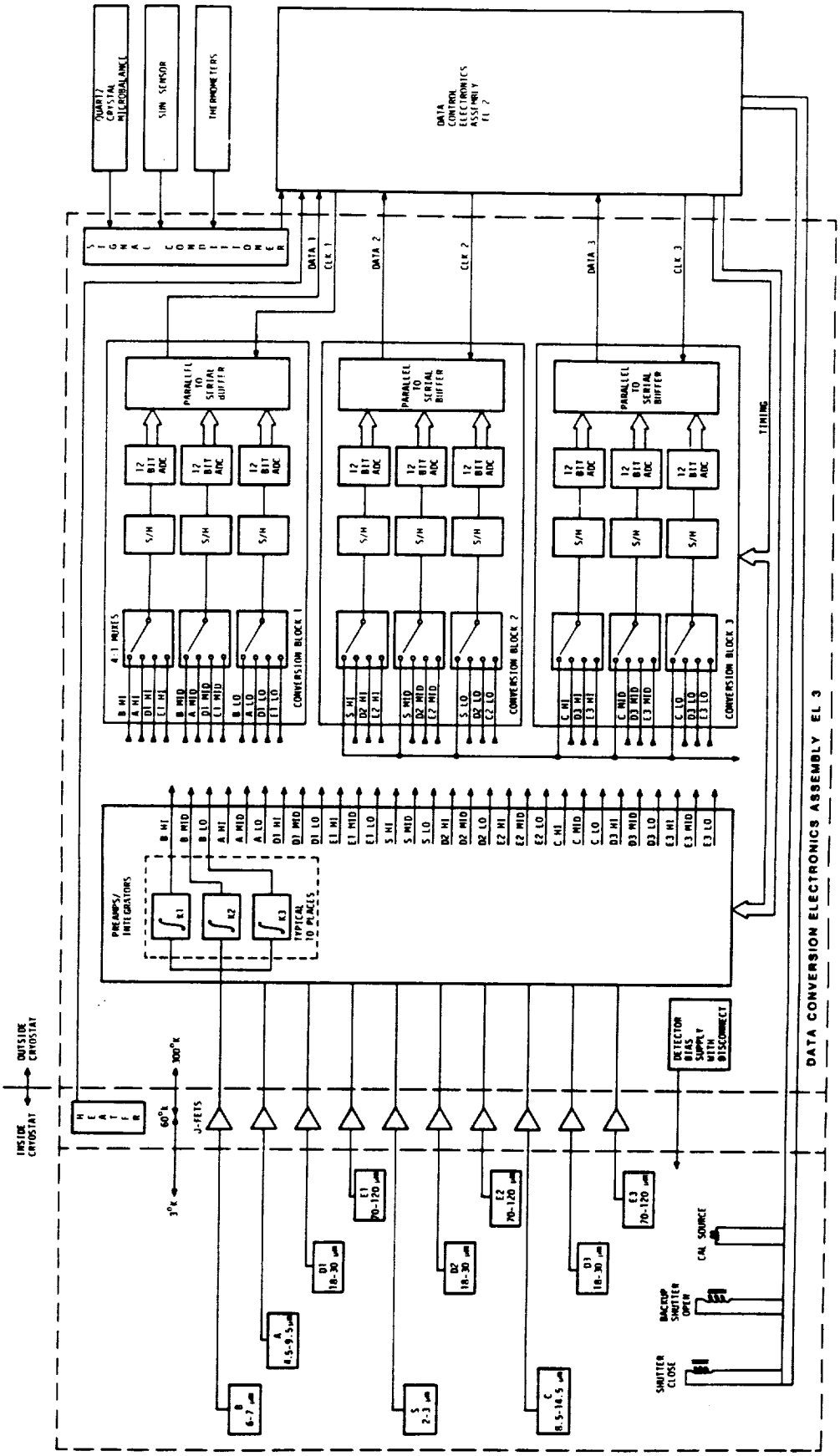

Figure 8. Electronic flow diagram of IRT detector data

2.3.7 Electronic Ground Support Equipment

For operation and checkout of the instrument, electronic ground support equipment was built using a Nova 3/12 computer with two 75 ips 1600 bpi digital recorders and an electrostatic printer/plotter. The system provided real-time strip chart output of any four detectors at once as well as recording all three HRM channels at the full input data rate of 614 kbps. With this equipment it was possible to make real-time evaluation of the instrument performance as well as provide quick-look recordings for off-line processing during the mission. The software for this system was written in SAO Forth.

3. OPERATIONS

3.1 Observing Plan

The basic observing mode required the Orbiter to be in the XVV/ZLV attitude, that is, with the nose in the direction of the velocity and the payload bay pointing toward the local vertical, and that the telescope scan over 90 degrees in the plane normal to the velocity vector. This is illustrated in Figure 2. The scan plane rotated at the Orbiter orbital pitch rate about an axis orthogonal to the scan axis. By taking data with the Orbiter rolled to ± 20 degrees, a 130-degree band of the sky centered on the orbital plane could be mapped. A scanning period of 0.5 minute, a pitch rate of 4 deg/minute, and detector fields of view of one degree in the pitch direction (see Figure 2) provided redundant overlapping coverage from scan to scan. This permitted identification of transient events by noting their appearance or lack thereof on subsequent scans. Transients were further characterized as cosmic ray hits, due to their instantaneous rise and rapid decay of less than two msec, or as particulate sightings, based on spectral characteristics, relative velocity, spatially extended nature, and intensity. The information about the particulates was utilized in understanding the induced Orbiter environment. In addition to detection of discrete transient events, thruster firings and other bursts of gases were seen as background transients. The thrusters were particularly bright, exceeding the cosmic sources by many orders of magnitude in brightness.

In order to distinguish between non-cosmic discrete objects and astronomical discrete sources and to measure the Orbiter gaseous "halo," data were taken on adjacent revolutions so as to be able to look for variability. An IR source that is sufficiently far from the telescope so as not to be defocussed but is not at a cosmic distance will not reappear on a subsequent orbit, at least not in the same place.

3.2 Avoidance Criteria

In the process of mapping the sky, there were a number of very intense IR objects which had to be avoided for a number of reasons:

1. They would have damaged the detectors if imaged onto the focal plane,

2. Their direct radiation into the aperture (but not on axis) would have

produced a thermal imbalance within the cryostat,

3. Their off-axis signal strength would significantly increase the IR background level and change the DC offset of the detectors.

The bright objects to be avoided were the sun, moon, earth, and any surfaces of the Orbiter or its payload.

3.3 Accessible Sky

The maximum sky coverage available for any given mission is dictated by the avoidance criteria for the sun, moon, and earth. For the 314-km altitude flown, for a 35-degree avoidance angle for the sun and earth, and in utilizing ±20-degree rolls, 75% of the sky could have been mapped on this mission. Most of the inaccessible sky on Spacelab-2 was due to the solar avoidance requirements.

Figure 9 shows the portion of the sky that was typically accessible for a given orbit for the XVV−20 attitude on Day 3 of the mission in orbital plane coordinates. For planning purposes, the information was shown in a coordinate system with the mean orbital plane as the equator. The scan paths are nominally parallel to the lines of longitude in this system. Orbit noon is at the center of the plot; the orbit poles are at the poles of the plot; orbit midnight is at the extreme left and right edges of the plot. The position of local vertical for various times in the orbit are indicated with time marks. Orbital sunset (SS) and sunrise (SR) are marked. The scanning minimum (45°) and maximum (135°) limits are shown for the −20° roll. The large cone near the center of the plot is the sun avoidance cone and the smaller cone near the right edge is the moon avoidance cone. The ecliptic plane (passing through both the sun and moon avoidance cones), equatorial plane (with RA shown at 0°, +90°, 180°, and −90°), galactic plane (with galactic longitude shown at GC = 0°, +90°, 180°, and −90°), and orbital plane are indicated.

Figure 10 contains most of the same information as Figure 9 except that this plot shows an inertial attitude and the scan path of the telescope on the sky. For example, attitude number 11 was the eleventh inertial attitude in the file for Day 3. The +11 on the plot indicates the 135° end of the scan and the −11 indicates the 45° end of the scan. The attitude name Vela refers to the attitude required for the Spacelab-2 X-ray experiment to view Vela SN, not where the IRT was pointed. This particular time was one of the two times that a low

	Long	Lat
EQUATORIAL POLE	90.00	40.52
GALACTIC POLE	60.27	-15.66
ECLIPTIC POLE	107.60	22.52
ORBITAL PL POLE	0.	90.00
Sun 46.0 avoid	12.33	12.93
Moon 10.0 avoid	-155.98	2.97
Limb 40.0 avoid		
VelV 75.0 avoid		

Classical orbital elem at 17:20:26 MET

Orbital inclination	49.4795	deg
Argument of perigee	65.1880	deg
RA of ascending node	151.6185	deg
Mean anomaly	145.7787	deg
Equatorial altitude	314.6550	km
Argument of latitude	210.9667	deg
Regression rate	-5.4644	deg/day
Argument of lat rate	3.9656	deg

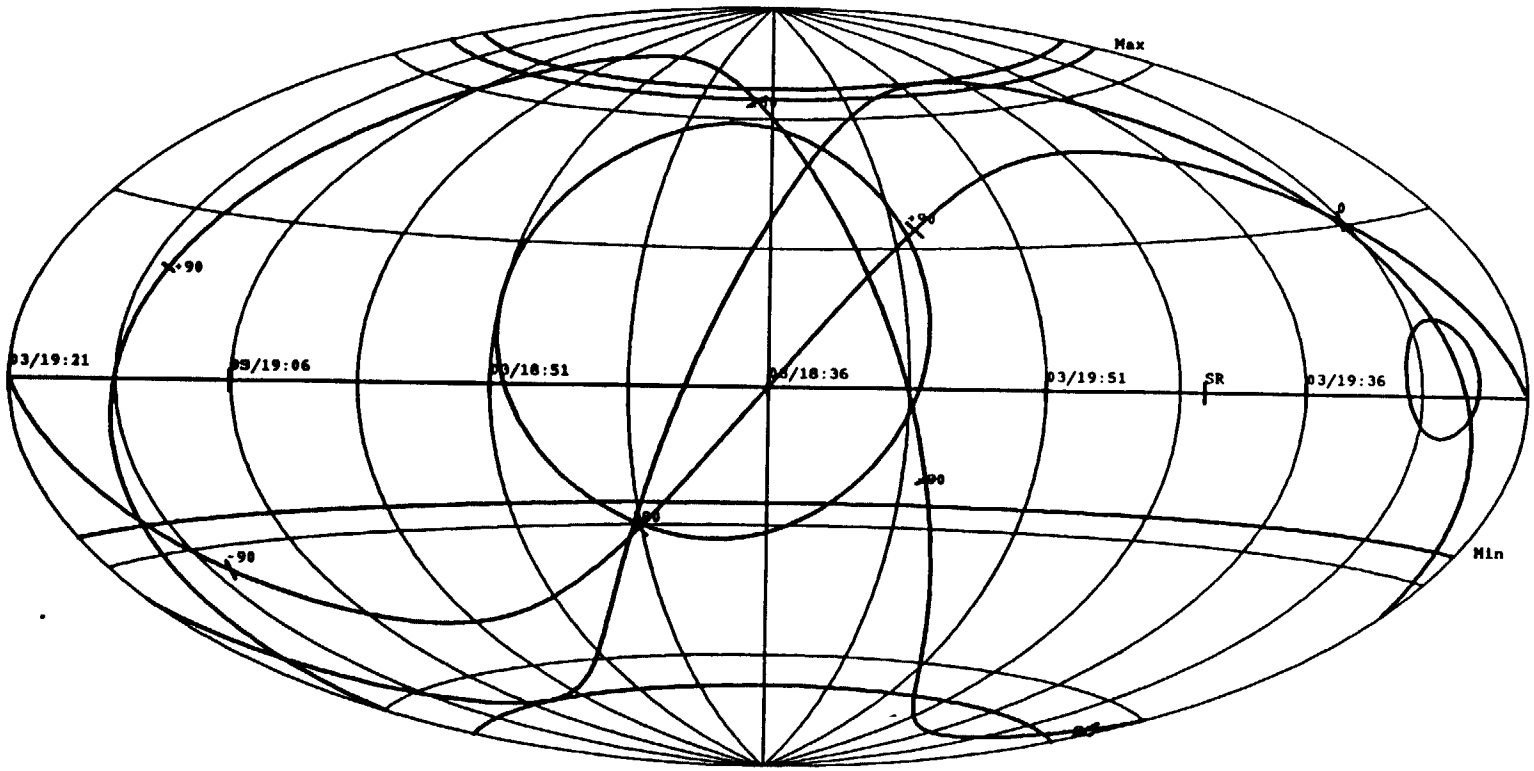

Pitch about orbiter +Y	2.50	deg
Roll about orbiter +X	-20.00	deg
Minimum scan limit	45.00	deg
Maximum scan limit	135.00	deg

ORBITAL PL COORDINATES

Plot interval 03/18:31 to 03/20:02
Launch 1985 JUL 29 at 21:00:00 GMT
JD @12H GMT for above date is 2446276
Plot generated Fri Aug 2 11:12:15 1985

Figure 9. Portion of the sky in Orbital plane coordinates that was typically accessible for a given orbit, in this case for the XVV−20 attitude on Day 3 of the mission

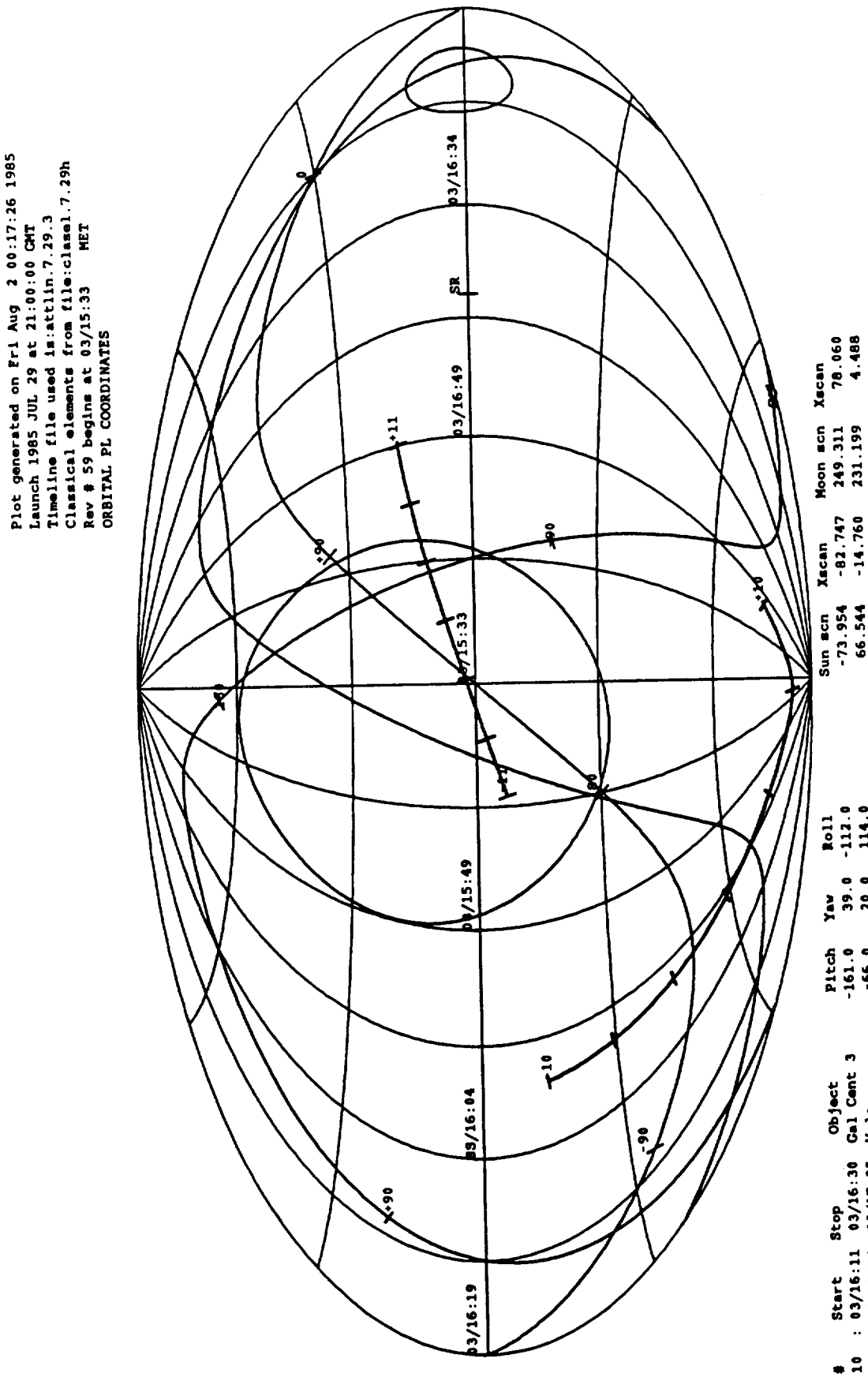

Figure 10. Similar to Figure 9, except that this plot is for an inertial attitude and the scan path of the telescope on the sky is indicated

background was seen in all IRT detectors and it is referred to later as the Vela 2 attitude.

3.4 Thruster Activity

Of prime concern for a mapping or pointed instrument is the stability of the space platform. Since the Orbiter does not have any momentum wheels, the only stable attitude is in gravity gradient mode with the X-axis along the local vertical vector. This would not have been a satisfactory attitude for this experiment. Thus considerable Vernier Reaction Control System (VRCS) activity was required to maintain the desired attitude.

The activity of the VRCS was of prime interest for three reasons:

1. The frequency at which a new equation of motion would have to be derived for data reduction;

2. The IR signal generated by the hot burst of gas; and

3. The effects of contamination that result from the VRCS plume deposition on the telescope.

From simulations of the VRCS for the IRT attitude with a ± 2-degree deadband and a 30-degree roll (worse than 0-degree roll) about two dozen firings per revolution were to be anticipated. This is about what was eventually observed, averaging periods of 10 to 20 minutes of no firings and with other times when there would be a burst of thruster activity.

The thermal emission from the thruster plumes was not of great concern from an astronomical data-taking standpoint since the emission had a rapid decay time constant of a few seconds and the typical firings where on the order of a fraction of a second to several seconds. However, as will be described later, the detector system, especially in the S-band, exhibited very long-term memory problems on the order of $5-10$ minutes after those very bright thruster firings which saturated the detectors. The location of the thrusters, the directions of the nozzles, and the angular size of the plumes were such that the plumes were not expected to appear in the field of view (JSC 07700). The direction cosines of the thruster vectors in payload coordinates (see Figure 2) for the six thrusters are given in Table 3.

Table 3. Direction Cosines of the VRCS Thrusters in Payload Coordinates

	Location	$\text{Cos}\theta_x$	$\text{Cos}\theta_y$	$\text{Cos}\theta_z$
F5R	Forward Right	-.033	.694	-.719
F5L	Forward Left	-.033	-.694	-.719
R5R	Aft Right	0.000	1.000	-.025
L5L	Aft Left	0.000	-1.000	-.025
R5D	Aft Right Down	0.000	.000	-1.000
L5D	Aft Left Down	0.000	0.000	-1.000

Since the telescope only scanned ±45 degrees from the X-Z plane and the plumes extended out only 41 degrees from the thruster axis, the telescope could not view a L5L or R5R plume directly. However, the R5D and L5D plumes were reflected off the wings, causing these plumes to be much brighter and of greater concern. All the plumes scatter off the residual O_2 resulting in measurable column densities and return fluxes (see Rantanen and Strange Jensen 1977).

The back-scattered VRCS gases were of concern from a contamination standpoint as well, since they would enter the telescope aperture and might adhere to the cryogenically cooled surfaces. Deposits of only a few microns would degrade the optical performance of the telescope significantly. In particular, the emissivity of the mirror could have been raised and the ability to reject scattered radiation from bright sources outside the field of view would be reduced. However, due to the high background described later, it is impossible to determine if there was any substantial buildup on the mirror.

3.5 ECAS Support

In order to determine the scan limits in real time, onboard computation with the Spacelab computer was necessary. This provided the data to avoid the sun, moon, and earth. Further, any Orbiter attitude where the telescope axis could come within 75 degrees of the velocity vector could cause excessive contamination buildup on the mirror and sunshade. This added a fourth constraint to the scan limits. The scan limits were determined using Spacelab ECAS. The algorithm devised for this purpose was called the Bright Object Avoidance Algorithm (BOAA). BOAA was divided into four functions; the first two were also utilized by the solar experiments on SL-2 to acquire the sun.

The first function of BOAA was to use the standard Orbiter-supplied state vector containing GMT, Orbiter position, velocity, attitude quaternion, and rotation rates in the Aries Mean 1950 (AM50) coordinate system for computing the Orbiter altitude, nadir, and velocity direction cosine vectors in AM50 and to convert the quaternion into the attitude direction cosine matrix.

The second function was to use an ephemeris to get the sun and moon direction cosines and then to convert the direction cosines for the sun, moon, nadir, and velocity vector into payload coordinates using the direction cosines matrix.

The third function was to determine if any of the four avoidance cones intercepted the scan plane and then where each would intercept to set the scan limits at this angle. The nominal avoidance angles are given in Table 4.

Orbital parallax for the moon was ignored. The angle used to avoid the earth was the sum of the angles from the nadir to the horizon based on the computed altitude plus the earth avoidance angle given in Table 4.

As an object approached the scan plane the scan angle was reduced so as keep the object well away from the telescope axis. Then, as the bright object(s) moved away, the scan limits were increased. If the scan range had contracted substantially (θ_M nominally equal to 22.5°), the average power consumption would become large due to the 120 watts used at turnaround. Hence, scanning was stopped when the scan range was less than θ_M. If the sun got to within θ_M of the stopped position, the shutter and cover were commanded closed. If scanning had stopped it would resume automatically unless the cover had to be closed.

Table 4. BOAA Scan Limit Input Parameters

(All angles in degrees)

Parameter	BOAA Var.	Default Range	Nominal Value	Final Value
Minimum Scan Range	θ_M	0 to 90	22.5	0
Minimum Shaft Angle	$\theta_{\min}$	40 to 140	45	42
Maximum Shaft Angle	$\theta_{\max}$	40 to 140	135	135
Sun Avoidance Angle	θ_S	0 to 180	35	50
Moon Avoidance Angle	θ_L	0 to 180	20	1
Earth Limb Avoidance Angle	θ_E	0 to 180	35	30
Velocity Avoidance Angle	θ_V	0 to 180	75	75

The final function of BOAA was to format the scan limits into a single 16-bit serial word, which was sent via standard Experiment Computer Operating System (ECOS) services to the experiment to control the scan limits. The scan limits were computed at a 1-Hz rate.

3.6 Displays

Figure 11 shows one of the two onboard displays that were used in support of this experiment. This display was used for scan system and BOAA monitoring. The upper right section of the display was for monitoring and control of the mechanical functions associated with the scan drive. The lower section displayed the corresponding avoidance angles for each of the four objects. The locations of these four object vectors were given in coordinates relative to the scan plane and with respect to the shaft encoder reading. The "TELESCOPE ENCODER" and "SWITCHES" values were a measure of the actual telescope motion and were updated once every second. "ENCODER" displayed the actual angle in degrees with 90° being along the Z-axis; the "SWITCHES" values toggled between 1 and 0 with the following correspondence: 100 = 45, 45 < 110 < 90, 010 = 90, 90 < 011 < 135 and 001 = 135. The upper left section of the

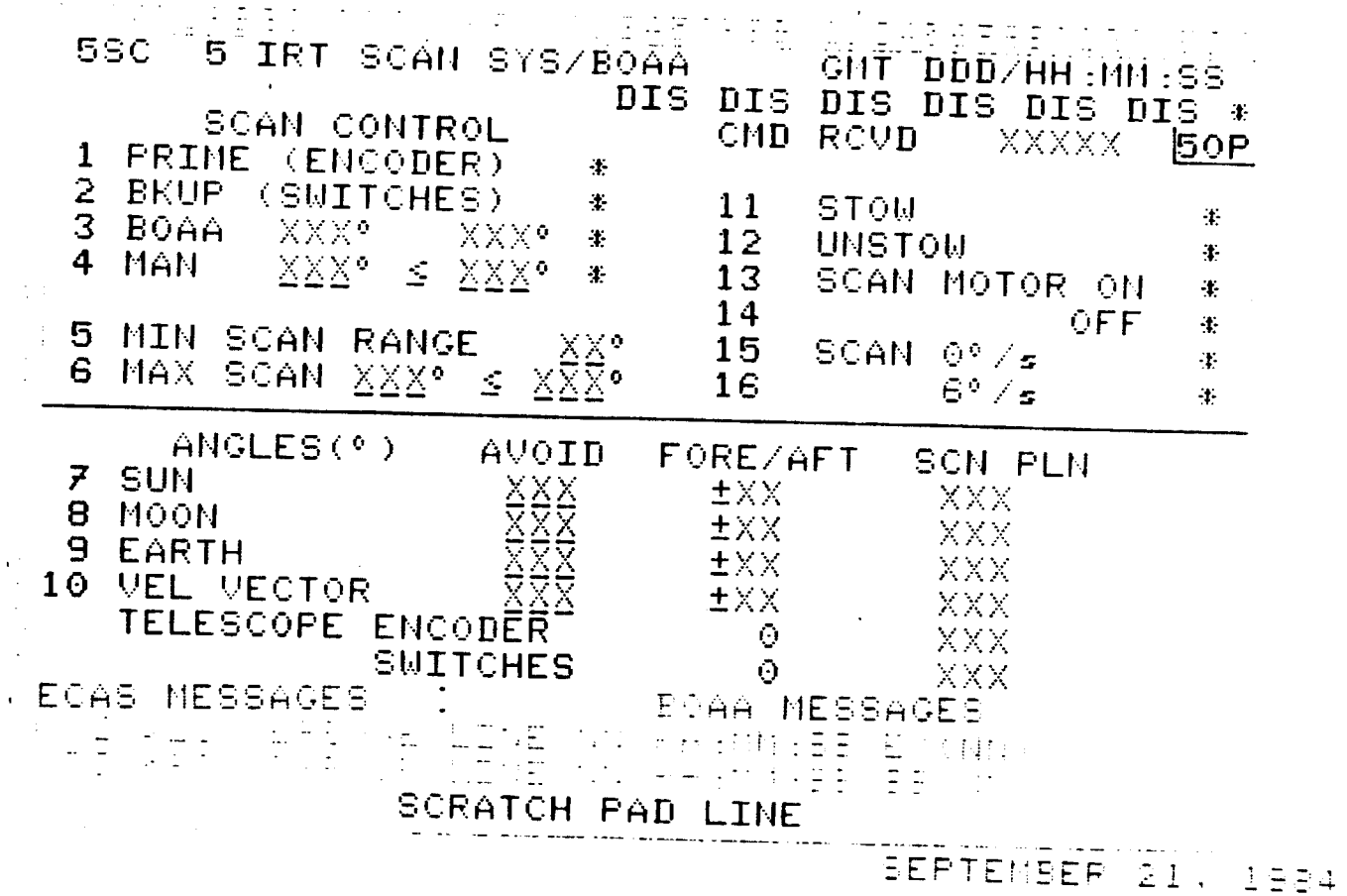

Figure 11. On-board display used for support of the scan system and Bright Object Avoidance Algorithm

display was for monitoring the scan and manual control. Item entries 1 and 2 selected either the shaft angle encoder or the position switches as the means by which the scan drive logic determined the turnaround point. Item entry 3 selected BOAA as the origin of the scan limits and the computed scan limits were displayed. Item entry 4 selected manual entry as the origin of the scan limits and with item entry 4 two parameters were entered for the minimum and maximum scan angles. Items 1 and 3 were the default modes. Item entry 5 allowed for changing the minimum scan range used by BOAA, nominally 22.5°. Item entry 6 required two input values and allowed for changing the normal turnaround values used by BOAA, nominally 45 and 135.

All of the above functions – parameter input, commanding, and display of measured parameters – could also be performed from the ground, since BOAA was in permanent ECAS and commanding and parameter measurement were done with standard ECOS. However, due to the limited amount of onboard memory, ECAS, in order to support the onboard displays, had to share permanent memory with the other display for this experiment. As an example, a software timer which turned a heater on and off to anneal the detectors for a pre-selected interval could be exercised either from on board or the ground when the operations display was allocated. Non-permanent ECAS used as part of a display could not be run unless the display was allocated. However, the ECOS-supported on/off commands could still be sent independent of which display was allocated. It should be noted that on SL-2 there was only enough space in memory to allocate simultaneously one display for each experiment plus other necessary permanent ECAS for the payload. The display that was to appear on the CRT was selected from the set that had been allocated in memory. If the required display was not in memory, it had to be first read into memory from the tape storage unit before it could be allocated. Normally, the BOAA display was left allocated in memory. The operations display for IRT is shown in Figure 12.

3.7 Original Observing Sequence

The optimum way to achieve the necessary uniform sky coverage was to fly the Orbiter in the XVV attitude. Other attitudes, such as inertial, were not useful for the survey. Any attitude where the payload bay was not well away from the sun or the earth was almost totally useless for doing any IR observations. Due to the recent importance of making measurements of spacecraft glow in the IR, two of the XVV revs were changed to XPOP. In the end the mission was planned to provide 18 revs of IR observing spread over Days 2 through 6 as

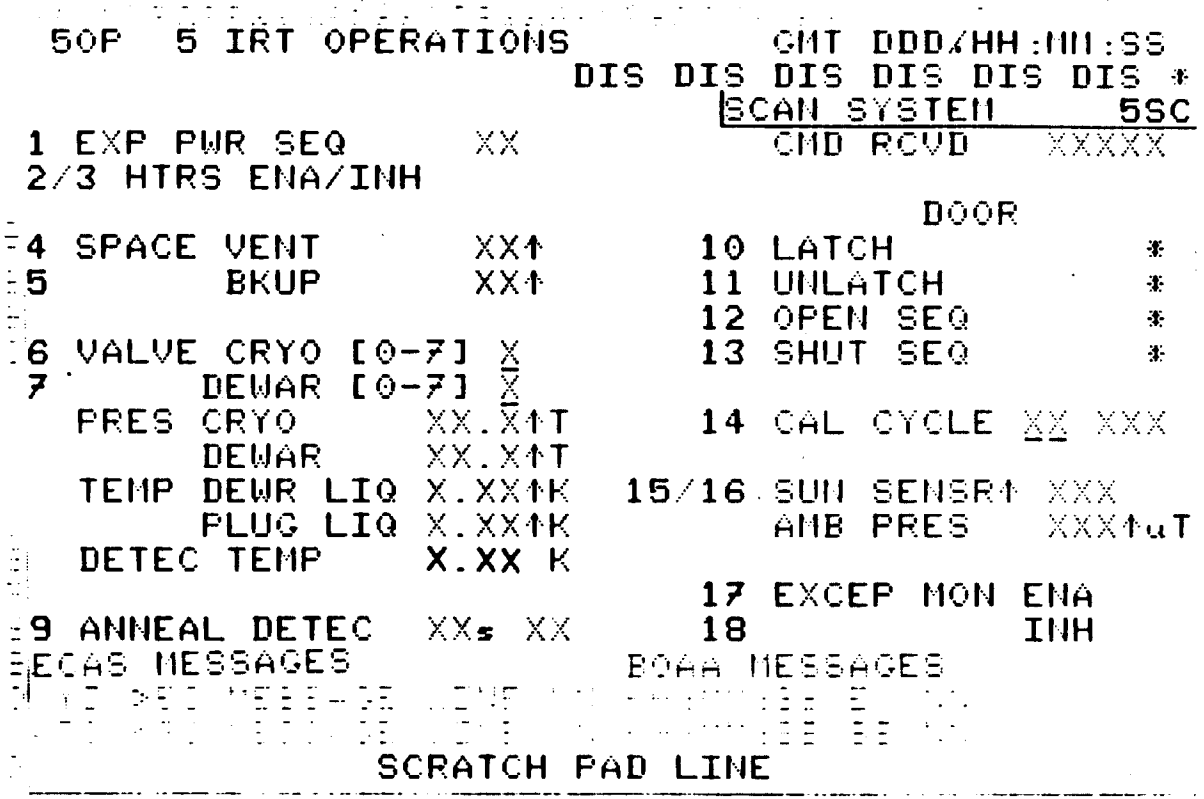

DECEMBER 11, 1984

Figure 12. IRT operations display format

shown in Table 5.

Table 5. Planned IRT Observing Attitudes

MET Start	Attitude	# of Revs
1/23:00	XVV	2+
2/20:30	XVV	2
3/00:00	XVV +20 roll	2
3/19:40	XVV −20 roll	2
3/23:00	XPOP	2
4/18:40	XVV −20 roll	2
4/22:00	XVV +20 roll	2
5/19:20	XVV −20 roll	2
5/22:40	XVV +20 roll	2
		Total 18

XVV: Orbiter X-axis along the velocity vector
XPOP: Orbiter X-axis perpendicular to orbit plane
MET: Mission elapsed time

3.8 Instrument Turn-On and Checkout

The turn-on and checkout of the IRT went smoothly. At three hours mission elapsed time (MET) the IRT was turned on. It was determined that the helium vent line valve did open during ascent as planned and that the helium temperature and pressure were nominal. The scientific operation of the instrument was not to begin until about 47 hours MET to permit the Shuttle-induced contamination to decay and the time until then was used checking out the instrument. Inspection of the housekeeping data verified that all aspects of the instrument were functioning as anticipated. Then software was verified and all hardware functions checked. Measurements taken from the quick-look data indicated that all of the IR detectors were functioning and the levels while viewing

the cold shutter were reasonable, although the bias in the C-band was seen to be shifted from its baseline value so that about one-third of its useful range was lost. The levels in the detectors while viewing the cold shutter were uniformly the same throughout the entire mission. In summary, the instrument had no detectable failures as a result of launch.

3.9 Initial Observations

Upon opening the telescope cover for the first time at 212/19:40 a much higher background was observed in the IR than expected. This high level persisted throughout the rest of the mission in one form or another. The remainder of the observing and the changes made to the observing plan were aimed at trying to understand the background and attempting to find conditions under which it would be less. Appendix B provides sample plots of the data.

3.10 Changes in Observing

It was and still is not clear what the induced environmental conditions were that caused the high background. During the mission many attempts were made to track down the cause of the effect or effects. To test various hypotheses regarding the levels and the variability of the background, some of the later observing attitudes were changed. The planned XPOP attitude was of particular interest since the streaming over the Orbiter was to be from a completely different direction from that during the XVV attitude. However, it does not appear that there was a substantial difference in background among the various attitudes. One of the hypotheses regarding the high background was that the Orbiter was flying in its own toroid of contaminants, so measurements were taken before, during, and after the Hobart burn in hopes of seeing a change associated with the change in the orbital plane. No substantial change was seen. The as-flown IRT observing attitudes, which also reflect the slip in launch time and major reallocation of time towards the end of the mission, are given in Table 6.

During each of the attitude intervals the cover was opened and closed a number of times:

1. At the end of an attitude interval by command from the POCC,

2. By BOAA due to the sun, moon, earth, or velocity vector avoidance, or

Table 6. As-Flown IRT Observing Attitudes

GMT Start	MET Start	Attitude	# of Revs
212/19:30	1/22:30	XVV	>2
213/17:00	2/20:00	XVV	2
213/20:10	2/23:10	XVV +20 roll	2
214/15:40	3/18:40	XVV −20 roll	2
214/19:00	3/22:00	XPOP	<2
215/14:25	4/17:25	P=−40	1
215/16:00	4/19:00	P=+50	1
215/17:40	4/20:40	Y=+45 R=+30	1
215/19:10	4/22:10	Y=−45 R=−30	<1
			Total 14

See the notes to Table 5

P,Y,R: Refer to pitch, yaw, and roll relative to XVV

GMT: Greenwich Mean Time

MET: Mission elapsed Time (0/0:00:00 MET = 210/21:00:00 GMT)

3. Via hardwired control from the sun alarm when scanning too close to the sun.

A detailed breakout of the attitude start and stop times, cover open and close times, the method used to close the cover, and whether or not the telescope was scanning are given in Table 7 for all of the observing for which data were obtained. During each of these observing intervals some but not all of the detectors were usable. The quality of the data is tabulated in Table 8.

Table 7. Observing Intervals

	Attitude Start GMT	Stop GMT	*Cover Cycling* Open GMT	Close GMT	Close Method	*Scanning*
Day 212						
XVV/0	entire	time	19:40	23:35	POCC cmd	Yes
Day 213						
Gal Cen 1	entire	time	7:04	7:09	POCC cmd	No
Vela 1	entire	time	13:42	13:50	POCC cmd	No
Vela 1	entire	time	13:54	13:57	POCC cmd	No
XVV/0	16:47	19:51	17:02	cont.		Yes
X8 view	19:51	20:08	cont.	20:07	BOAA	Yes
XVV/20	20:08	23:07	20:15	23:15	BOAA	Yes
Day 214						
Vela 2	entire	time	13:59	14:14	Sun alarm	No
XVV/-20	15:31	cont.	15:40	17:02	BOAA	Yes
	cont.	18:33	17:06	cont.		Yes
X8 view	18:35	18:55	cont.	18:50	Sun alarm	Yes
Glow	18:55	21:30	19:03	cont.		No
Vela 3	entire	time	cont.	21:50	Sun alarm	Yes
Day 215						
Gal Cen 3	7:21	7:41	7:19	7:28	BOAA	Yes
Vela 4	entire	time	12:23	13:01	POCC cmd	Yes
P-40	14:11	15:52	14:26	cont.		Yes
P+50	16:00	17:08	cont.	17:33	Sun alarm	Yes
Y+45R+30	17:24	18:52	17:41	19:00	BOAA jump	Yes
Y-45R-30	19:02	20:24	19:11	20:10		Yes
Gal Cen 4	20:33	21:18	20:54	21:25		Yes
TDRS/A754	22:31	25:58	22:37	26:00	Sun alarm	Yes
Day 216						
Vela 5	12:20	cont.	12:37	13:05	POCC cmd	Yes
Vela 6	cont.	cont.	14:09	14:38	POCC cmd	Yes
Vela 7	cont.	16:36	15:40	15:48	POCC cmd	Yes
OMS 6	16:50	17:12	16:32	17:12		Yes
Therm 1	17:12	18:59	17:20	cont.		Yes
OMS 7	19:11	19:20	cont.	19:34	Pwr on/off	
Therm 1	19:32	24:40	19:37	21:26		Yes

Table 8. Summary of Prime Observing Data

		Det	S	A	B	C	D	E††
		λ,μm	2–3	4.5–9.5	6.1–7.1	8.5–14	18–30	77–115
Day	Attitude	# Revs						
212	XVV/0	2+	G	G	G	SB‡	SB	G
213	Gal Cen 1	5 min	G	G	G	G	SB	G
213	Vela 1	15 min	G	G	G	G	G	G
213	XVV/0	2–	G†1	M	M†1	M	M†1	UM
213*	XVV/20	2	G	M	M	M	M	UM
214	Vela 2	15 min	G	G	G	G	G	G
214	XVV/–20	2	G†2	M	M†2	M	M†2	UM
215	P=–40	1	G	SM	SM	SM	SB	G
215	P=50	0.7	G	SM	SM	SM	SB	G
215	Y=45,R=30	0.7	G†3	SM	SM†3	SM	SB†3	G
215	Y=–45,R=–30	0.7	G	SM	SM	SM	SB	G

†† E1 detector appeared to be anomalously low on Day 212 and thereafter essentially dead.

†1 S, B and D1 data bimodal from 18:23 to 19:13 due to overheating.

†2 S, B and D1 data bimodal prior to 16:45 and from 17:32 to 18:18 due to overheating.

†3 S, B and D1 data bimodal from 17:25 to 18:20 due to overheating.

‡ During Day 212, the A and B levels were decreasing precipitously. By the end of the day the C level was very close to coming out of saturation.

* Only attitude with galactic center coverage.

G Data is good.

SB Channel is saturated by high background.

M Mylar strip in beam. Channel is saturated.

UM Data is usable but mylar strip caused a higher background.

SM Channel is saturated. May be either high background or mylar strip.

3.11 Co-Observing

There were several co-observing times planned with other experiments. In some cases the test was to use one instrument to cause an observable effect on another. In other cases the test was to take simultaneous and complementary data. The first test was to perform a scan of the telescope as part of the Superfluid Helium Experiment's disturbance tests. This was carried out by the mission specialist operating the IRT scan drive. Another test was to look for effects of noise in the IRT data from the Vehicle Charging and Potential Experiment (VCAP) firing and then to see if the electron beam was visible in the IR. Since the IRT background was substantially higher than anticipated, there was no observable effect in the quick-look data. This essentially relieved the constraints on the use of VCAP during IR observing. One planned co-observing effort was to map clusters of galaxies in the IR simultaneous with the X-Ray Telescope (XRT). However, due to the viewing constraints imposed on the X-ray experiment because of potential Instrument Pointing System (IPS) failure modes, it was impossible to arrange the Orbiter attitude so that both the IRT and the XRT could view the same region of the sky. A second co-observing objective to measure spacecraft glow did result in acquisition of some useful IR data. The measurements were made using the base of the Plasma Diagnostics Package (PDP) as a stimulant above the IRT aperture.

3.12 Cryogenic Operations

The cryogenic achievements of the IRT can be divided into two categories:

1. The success of its observing operations, and

2. The outcome of the superfluid helium management tests conducted during the final 1-½ days on orbit.

The purpose of the cryogenic subsystem of the IRT was to provide sufficient cooling to keep the IR detectors at a stable temperature near 3K, while also keeping the mirror and telescope tube cold enough to prevent thermal loading from these surfaces onto the detectors. Moreover, the cryogenic system had to maintain these conditions throughout the 8-day mission.

Before and during the mission the performance of the cryogenic system exceeded all expectations. The on-pad servicing both for the aborted launch and the actual launch on 29 July 1985 went very smoothly. The onboard GSE pump in both cases maintained the superfluid for the two days between payload closeout and T−30 minutes. All of the critical temperatures were found to be at or below their intended values when the instrument was activated on orbit. It was found to be possible to maintain the detector block at a temperature of 3.1K to a stability of better than 2 percent. Further, it was possible to do so without requiring frequent valve adjustments. In essence, the system was able to deliver vapor flow efficiently and at a very stable rate. A total of 83 liters of liquid helium was used during the first six days of the mission. The final 35 hours prior to deactivation were devoted to the helium management portion of our flight objectives and will be discussed in the section on results. In spite of the fact that one day was added to the mission, the IRT landed with an estimated 30 liters of superfluid helium.

3.13 Sunshade and Vacuum Cover Damage During Flight

The telescope sunshade was made out of fiberglas honeycomb and lined with gold-coated mylar to keep the IR emissivity low. Due to concern over the high IR background the interior liner of the sunshade was inspected with the Remote Manipulator System (RMS) TV camera during the middle of the mission as well as being visible during the IR glow measurements. The aperture of the telescope (and liner) were inspected after the mission. There was a distinct change in the appearance of the liner between these two times. In the early inspection there did not appear to be anything unusual, whereas at the end of the mission the liner had a distinctly wrinkled appearance. The exact mechanism of this change is still unknown, although we believe it was due to solar heating.

3.14 The Broken Mylar Strip

In addition to the deterioration of the sunshade liner, a strip of mylar (part of the vacuum cover thermal baffle) was discovered to be torn and in the telescope field of view when viewed with the RMS wrist camera at the end of the mission. The flexible mylar strip was floating inside the vacuum cover shroud. This strip was designed to prevent a high thermal load entering the telescope from the inside of the cover cavity by presenting a low emissivity surface to the telescope. It was hinged at diametrically opposite locations and folded against the rigid baffle

on the far side of the aperture when the cover was closed. When the cover was commanded to the open position, the mylar strip was pulled into place by a lanyard. At the location where the damaged strip bent over the cover, the mylar appeared to be severely scorched. Following the mission, the mylar was very stiff, almost brittle. This may be why it "cracked" at its narrowest point. Also there are two very localized scorch marks at the base of the sunshade. One is directly above the position of the scorch on the strip. The origin of the concentrated energy needed to cause this is still a mystery, since the sunshade itself is not a focusing device. Based on the arguments given below it is shown that the strip was not in the field of view on Day 212 or during the Vela 1 and Vela 2 attitudes. On the other hand, during the prime observing on Days 213, 214, and 215 the strip was to some extent within the field of view.

3.14.1 D-Band Evidence for the Position of the Strip

The D-band detectors were on scale only during the non-prime non-scanning attitudes that are referred to as Vela 1 and Vela 2 (see Table 7). The bandpasses are near the peak of the emission for blackbodies in the range of 200 to 350K. Hence, these are the most sensitive to any obstruction at ambient temperature. The field of view of the three D detectors are spatially diverging. Therefore, the only way the three D detectors could have the same signal strength is if either the mylar strip was stretched across all three (causing saturation) or not visible to any of them. Since the DC signal measured in the three separate D detectors was essentially the same, taking into account their different responsivities, this implies that no part of the mylar strip was in the field of view during the Vela 1 and Vela 2 attitudes and the signals measured were exclusively due to the sky plus any contribution from the local environment.

3.14.2 E-Band Evidence for the Position of the Strip

The position of the torn mylar was such that it would enter the beam of the telescope from the corner with the B-band detector (refer to Figure 3). Thus, when the strip was in the field of view it would be expected that more of the strip would be visible to the E2 detector than the E3 detector, causing dissimilar signal strengths. This was evident when comparing the E2 and E3 data on Days 213, 214, and 215 (when A, B, C, and D were all saturated) (see Figure 13). In these data the E2 signal was greater than E3, implying that a source of substantially more radiation was in the E2 beam than in that of E3. In addition to the cover

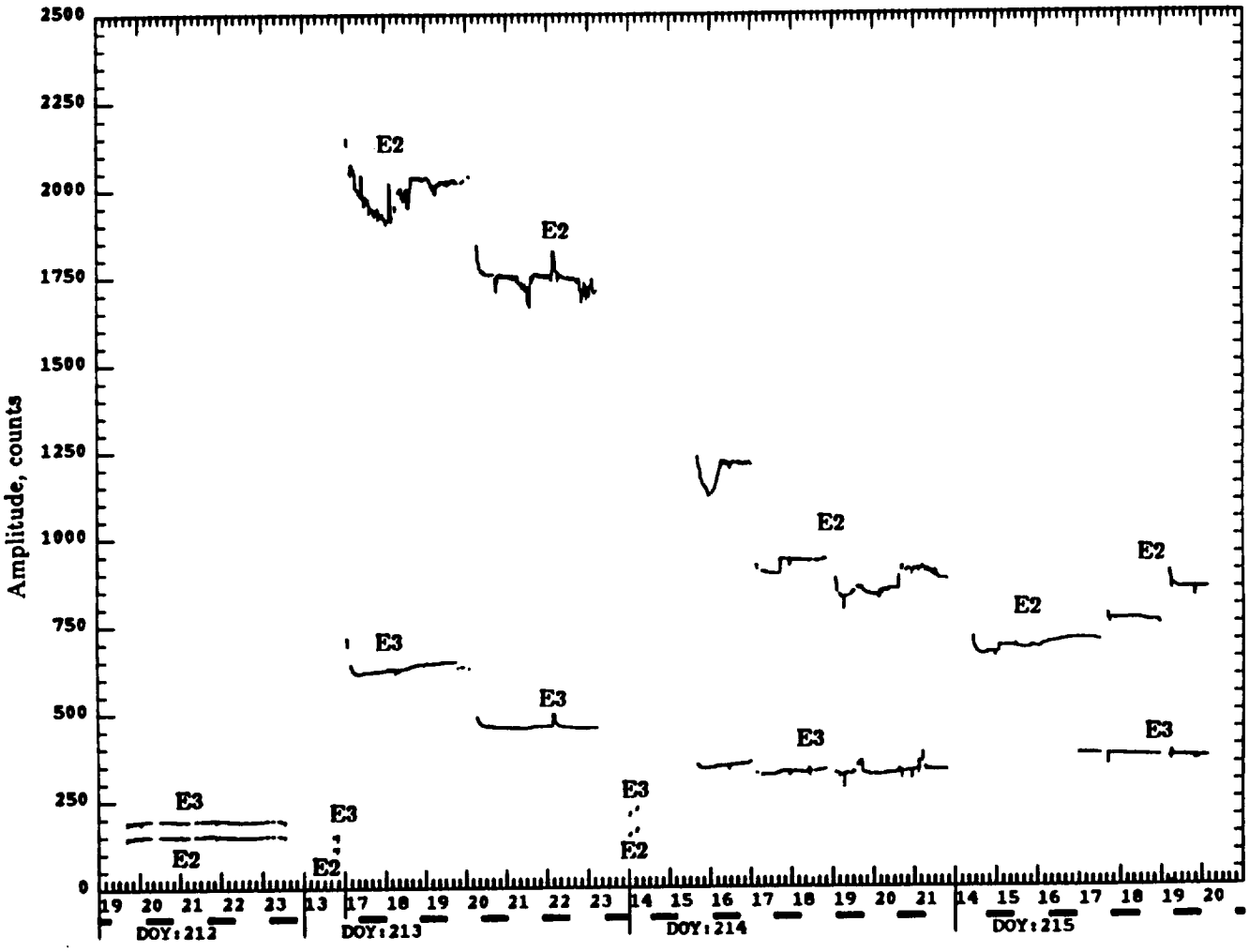

Figure 13. Samples of the minimum fluxes for two of the E-band (77 – 115 μm) detectors. The zero flux levels were at about 10 counts. Note the splits in the time scale. The dark bars indicate orbital night. The very high and erratic levels for E2 and E3 detectors on DOY 213 and 214 and for E2 on DOY 215 were caused by a strip of warm mylar protruding into the detector beam. The marked amplitude jumps at discontinuities from day to day and within each day occurred each time the vacuum cover was cycled, resulting in the repositioning of the mylar strip. The basic DC level is most likely due to radiation from the telescope forebaffle scattering off contamination in the mirror. The forebaffle temperature changes (over 40 – 60K) correlate well with the variations of the in-band flux that would be seen by the E-band detectors.

open and close operations performed at the beginning and end of each prime observing period, there were a number of other unplanned cover cycles caused by attitude changes and subsequent sun alarms. These occurred on Day 213 at 20:07, on Day 214 at 17:04 and 18:50, and on Day 215 at 17:33 and 19:00 (again see Figure 13). At each of these times there was a change in the DC level which can be attributed to the mylar repositioning after the cover cycle. Considering that the signal strengths in E2 and E3 were comparable during Day 212, GC1, Vela 1, and Vela 2, we conclude that no part of the mylar strip was in the field of view during these intervals. In addition, near the end of Day 212 there is evidence that the C detector was just into saturation, which would not be possible if even a square centimeter of mylar were in the beam.

Unlike its behavior during Days 213 and 214, the DC signal in the E3 detector on Day 215 was very uniform throughout the whole observing period. Also, E3 did not vary with each cover cycle as E2 did. Hence, we conclude that E3 was not affected by the mylar strip on Day 215 although E2, which was closer to the strip, was affected by it. The conclusions about the data quality summarized in Table 8 are based on the above arguments.

3.15 Re-Entry and De-Integration

At the end of the mission the vent lines were sealed prior to de-activation to prevent ingestion of air during re-entry. The telescope vacuum cover was also closed and latched to prevent buildup of ice on the cold telescope and possible damage to the instrument. The Orbiter landed with the remaining liquid helium. When tested at MSFC and after the mission, a vacuum of 0.5 Torr still existed within the instrument.

4. DIFFICULTIES WITH THE DATA

There were three major categories of problems in processing the data:

1. Those associated with reading and formatting the flight data tapes;
2. Those resulting from instrumentation problems;
3. Those that were a result of the non-astronomical signals encountered during observing.

4.1 Flight Data Tapes

Many problems occurred with the flight data tapes. The HRM-to-user system fell far short of the original Spacelab program goal of complete transparency to the user. This was true during hardwired connections of our Digital Ground Support Equipment (DGSE) to the test system (HITS/ECEP) at KSC, and it was also true during system checks using test tapes generated by GSFC from the KSC system. Worse, the GSFC test tapes did not even come close to representing the data errors that were experienced with the flight data tapes. Many of the problems were completely unexpected and in many cases the errors found violated Spacelab Data Processing Facility processing rules. Specifically:

1. There were gaps in the GMT which did not cause a break in the file, and should have.
2. There were times when the recorded GMT jumped backwards.
3. There were different GMT jumps between the three IRT HRM channels. This caused our processing system to lose time synchronization.
4. There were frequent unflagged synchronization word losses.
5. There were errors in the SECT tape header values.
6. There were errors in state vector values which threw into question the validity of other data on the tape.

7. There were occasional bursts of parity errors in the detector data which also left doubt about the quality of the data at those times.

Content and parameter definition on the OANC and SANC tapes was in many cases either obscure or non-existent. Also, about 1/4 of the tapes could not be read at all. Getting copies made which could be read caused additional processing delays. We had our tape drive manufacturer come in and spend a great deal of time tuning up the drives, but to no avail. The manufacturer even asked to send some of the tapes to his factory in California to see if they could determine the cause of the problem. No solution was ever found.

4.2 Missing Data

Although the IRT instrument was turned on for most of the mission, except for some periods when the EL-3 electronics box got dangerously hot in the solar attitudes, only HRM data from Days 212–215 have been processed. This amounts to about 24 hours of data. During these times a number of significant gaps in the data have been found. The gaps on Day 212 were particularly disturbing, since this was the only day when there were usable A- and B-band data. Worse, the gaps just happened to occur during the times of galactic plane crossings. After working with GSFC, some of these data were filled in. Table 9 is a list of the gaps of concern. A few of the shorter gaps have been acknowledged as permanently missing intervals (PMI) and are indicated as such.

Unprocessed Spacelab digital data tapes containing all the HRM channels were obtained from GSFC for some of the data gap times, including the galactic plane crossing data gap on Day 212. Special processing programs were written at SAO to read these tapes and recover the missing data. Although this required considerable effort, we were finally successful in recovering the more important data to fill the gaps. Basically, we found that the GSFC SECT tapes were filled with zeros whenever the processing software encountered all but the simplest data anomalies, a result no doubt of a GSFC processing algorithm designed for speed, not accuracy.

4.3 Bimodal Data

Due to the high heat input into the payload bay during the solar inertial pointing for many orbits between the XVV orbits, the temperature in the payload bay got very high and in particular the temperature of the IRT electronics box on the side of the cryostat, which had to be close to the detectors and could not be placed on a cold plate, got extremely hot. During the XVV attitudes EL-3 was running at about 270−290K. At the end of the solar attitudes just before switching back to the XVV attitudes the EL-3 temperature was running at 320−330K. When this occurred, one of the integrating IC's became unstable and caused the integrators for the S, B, and D1 channels not to reset properly. The data exhibited cyclic variations with a period of 8 samples and appeared to have a bimodal distribution. These data were processed separately to eliminate the bad values. The times when the data were bimodal are indicated in Table 8.

4.4 Non-Astronomical Artifacts

These problems fell into a number of categories. Some were expected, others were not expected at all. Some of these problems were isolated and to some extent removed during data processing. Others resulted in complete loss of useful data.

4.4.1 Saturated Signals

For several reasons the A-, B-, C-, and D-band outputs were saturated at various times during the mission. On Day 212 the output of C- and D-bands were saturated because of the high Shuttle-induced background. The data indicate that the induced environment signal was decaying with time. By the time of the two Vela attitudes on Days 213 and 214, it appeared that this induced environment signal had stabilized. However, as described above, during the remaining observing periods the mylar strip was in the aperture saturating the A-, B-, and D-bands. Thus, on Days 213, 214, and 215 the only unsaturated data were for the S- and E3-bands.

Table 9. SECT Data Gaps during IRT Periods of Interest

Start GMT	End GMT	Duration min:sec	
Day 212 XVV			
19:42:03	19:43:34	1:31	PMI
20:16:54	20:21:23	4:29	
20:21:23	20:22:58	1:35	
21:10:13	21:11:57	1:44	PMI
21:12:24	21:18:01	5:37	
21:24:08	21:24:44	0:36	PMI
21:25:31	21:30:19	4:48	
21:57:29	21:58:17	0:48	
22:57:05	22:57:53	0:48	PMI
23:04:00	23:04:50	0:50	PMI
23:16:37	23:23:19	6:42†	galc plane
23:33:52	23:35:46	1:54	
23:36:55	23:37:55	1:00	
	Total	32:22	
Day 213 XVV			
19:47:15	19:47:35	0:20	
19:47:59	19:48:26	0:27	
19:48:51	19:49:18	0:27	
19:50:05	19:50:30	0:25	
19:50:41	19:51:05	0:24	
19:51:13	19:51:56	0:43	
19:52:00	19:53:02	1:02	
20:08:42	20:09:20	0:38	
20:41:00	20:43:12	2:12	
22:45:19	22:45:29	0:10	
22:45:40	22:45:52	0:12	
22:45:56	22:46:58	1:02	
22:47:15	22:47:27	0:12	
22:48:11	22:48:27	0:16	
22:48:30	22:49:29	0:59	
23:06:25	23:07:06	0:41	PMI
	Total	10:10	
Day 214 XVV			
18:29:02	18:30:03	1:01	
18:33:14	18:35:34	2:20	
18:40:07	18:41:18	1:11	PMI
18:58:33	19:04:09	5:36	
	Total	11:08	
Day 215 XVV			
14:59:58	15:00:15	0:17	
15:25:20	15:25:40	0:20	PMI
15:47:01	15:48:53	1:52	PMI
18:44:29	18:45:17	0:48	PMI
18:55:05	18:55:37	0:32	PMI
	Total	3:49	

PMI: Permanently Missing Interval
† Only one of two times where A- and B-bands usable while scanning the galactic plane.

4.4.2 Variations Due to the Induced Environment

The effects of the Shuttle-induced environment superimposed on the astronomical data caused an asymmetry in the signal relative to the Shuttle payload. This amounted to about 10% of the overall signal level. This asymmetry was present in the A-, B-, and E-bands, but not in the S-band (see Figure 14). There was no scanning when the C- and D-band data were not saturated. Further, this signal decayed with time and was also modulated by the orbital period in such a way as to show a day/night effect. Signal level dropped after orbital sunset and continued to decline after sunrise with a minimum occurring about five minutes after sunrise (see Figure 15). This effect was separate from another data artifact, solar glare, which is described below. It had been anticipated prior to the mission that these effects would be faint and difficult to see and it was surprising to find them dominating the data.

4.4.3 Thruster Firings and Detector System Memory

Based on the known properties of the hydrazine thrusters, it was expected that there would be very strong signals from the thrusters and it was anticipated that the astronomical data during the thruster firings would be lost. This was the reason for selecting the XVV attitudes, which minimized the thruster activity to maintain stability, and for requiring multiple orbits in each attitude to help fill in any lost data. As expected, during the thruster firing itself the data were unusable both because the torques from the thrusters made it impossible to obtain an aspect equation and also because the signal from the thruster overwhelmed that from the sky by many orders of magnitude. What was not expected was that after the firing stopped there would be a long decaying tail in the data. Initial analysis of these data indicated that the tail had two time constants: one of a few seconds and another of about 20 seconds. From a serendipitous situation in which the focal-plane shutter just happened to be commanded closed immediately following a thruster firing, it was learned that the tail persisted even though there was no IR signal on the focal plane (see Figure 16). In the E-band data, the thruster turn-on and turn-off are quite sharp. In the S-band the thruster is extremely bright and the persistent tail is evident. Two seconds after the thruster shut off, the focal-plane shutter was closed. From the figure, it can be seen that closing the shutter had little effect on the S-band signal, indicating that the output was inherent in the detector system and not caused by IR emission from the plume. Thus one can conclusively state that the tail in the data which was predominant in the S-band, but also slightly present in the longer wavelengths, was

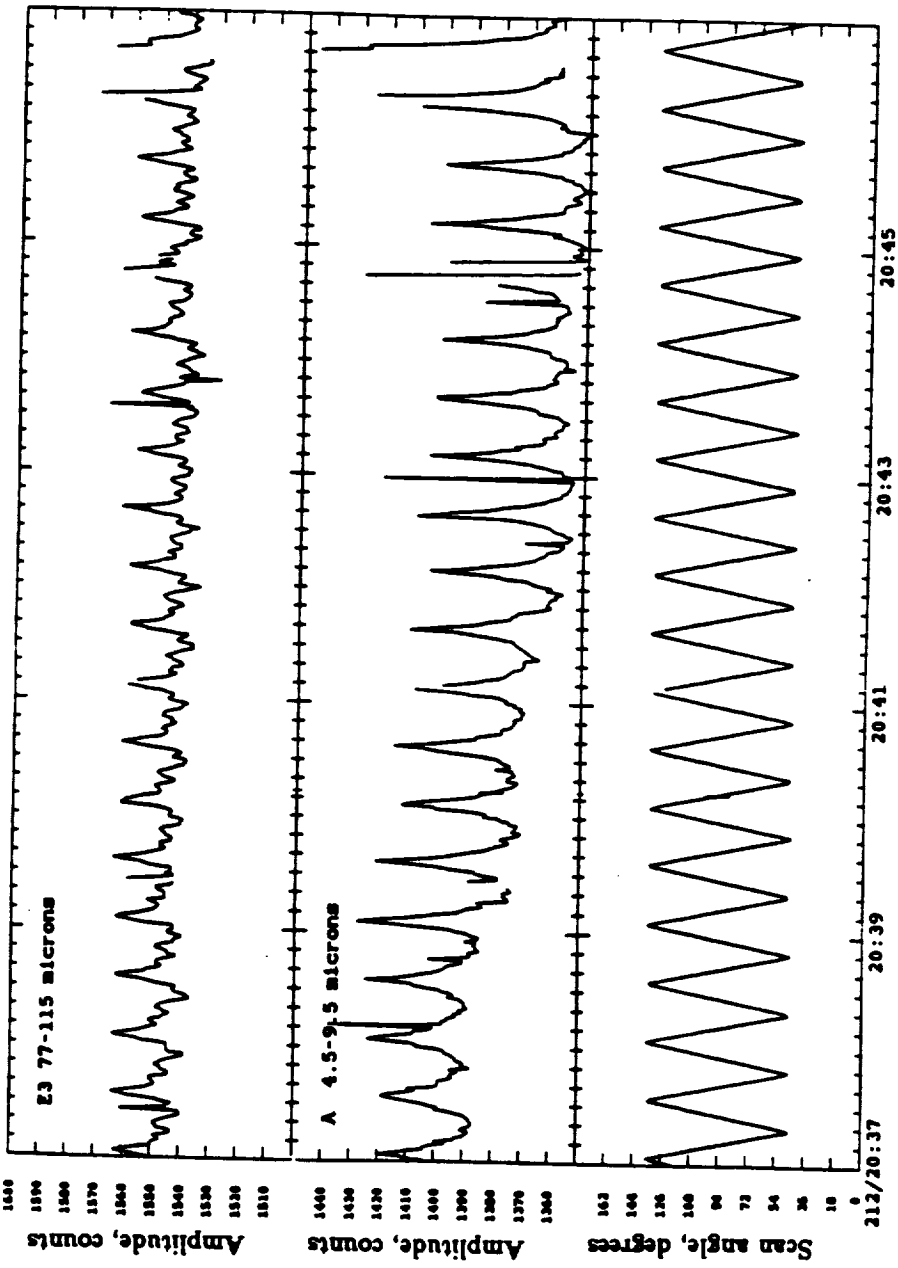

Figure 14. Variation of the background in the A- and E-bands as a function of telescope scan angle. Sunrise occurred one minute past the end of the plot at 20:47 GMT. The scan angle varied between 45° and 135° (port side) with local vertical being 90°. The pronounced asymmetry is fixed with respect to the Shuttle and not the sky. Only 8 out of every 1024 samples of data were used in these plots.

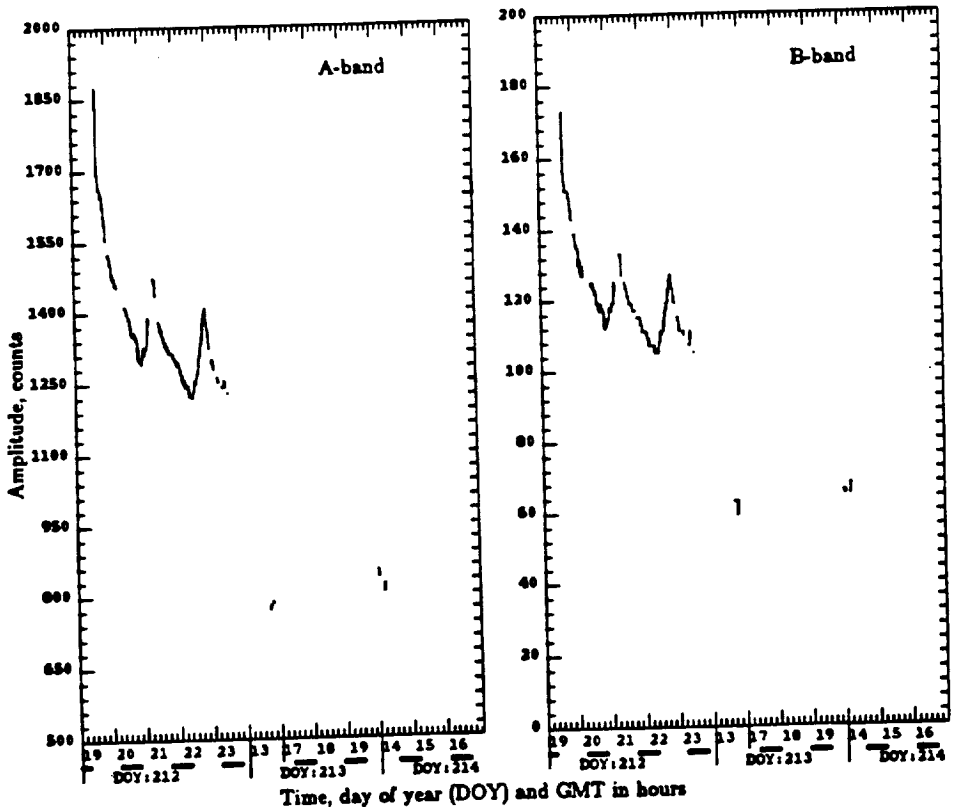

Figure 15. Samples of the minimums for the A-band (4.5−9.5 μm) and the B-band (6−7 μm) fluxes. The zero flux levels were at about 510 and 30 counts respectively. Note the splits in the time scale. The dark bars indicate orbital night. The B-band was selected in combination with the A-band to identify the broad water features at 6−7 μm. The very low levels seen for short periods on DOY 213 and 214 are very nearly at the zodiacal radiation level expected for these two pointed directions.

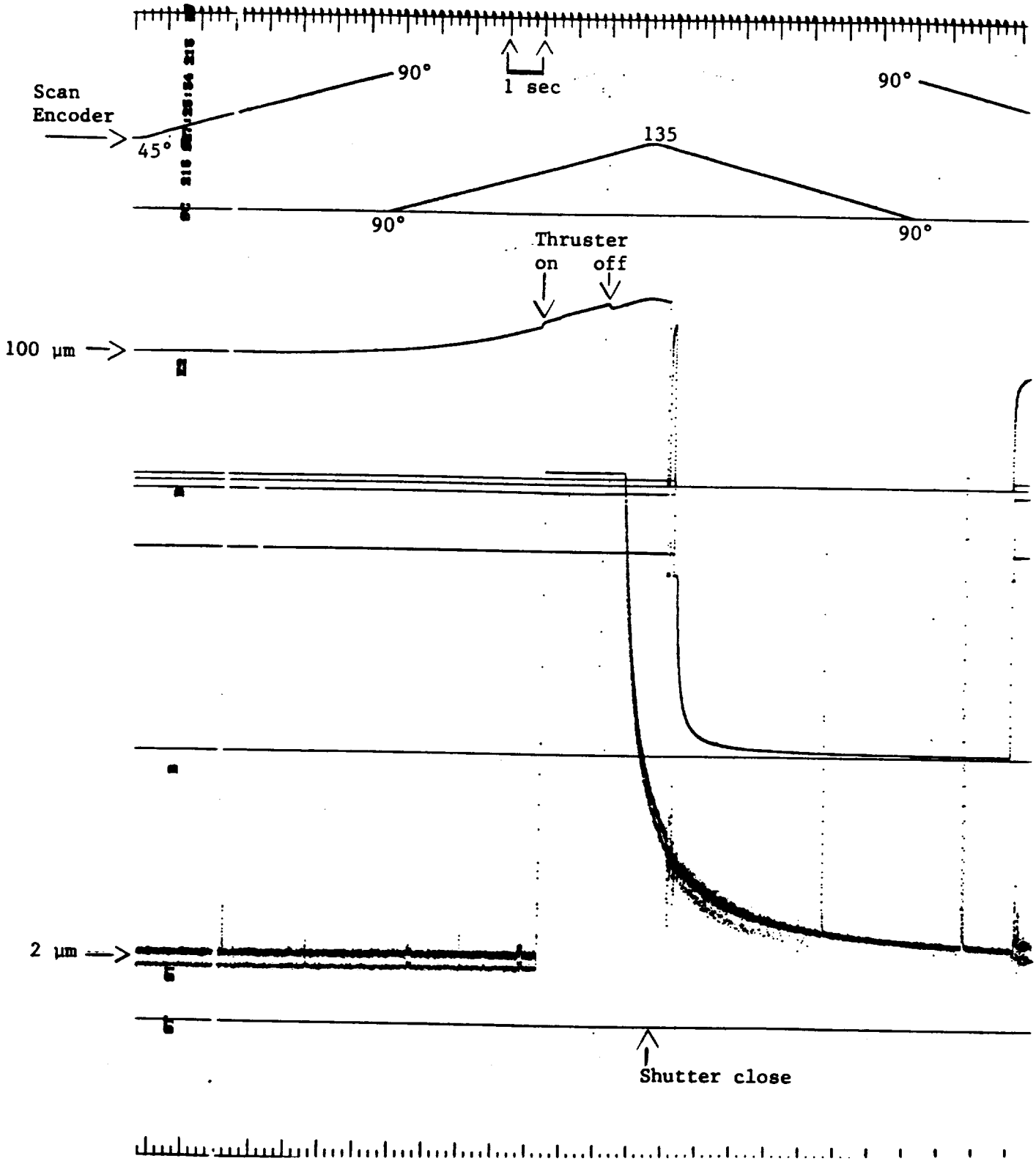

Figure 16. Evidence for detector system memory

electronic in nature and not an inherent property of the IR signal from the thrusters. This electronic tail was also seen while scanning across the very brightest galactic plane features and while scanning near the sun.

Development of a software filter to remove this fading memory effect was successful. In a few cases, however, a small amount of undershoot in the filtered signal occurred. This filter was not only important and useful in dealing with signal fading following thruster firings but also in removing hysteresis from the data when scanning across bright portions of the galactic plane and in trying to remove the effects of the "solar glare" which spread over a large portion of each scan.

4.4.4 Solar Glare

Another feature that could seen in the data was a large detectable signal from the sun well outside of the instrument rejection cone (see Figure 15). Recall that the sunshade was designed to reject light coming from greater than 45 degrees from the telescope axis. From the TV pictures taken on Day 218 we know that the inside surface of the sunshade had been damaged at some time during the mission. TV pictures taken during the glow experiment on Day 214, however, show the sunshade liner still looking pristine. Therefore, a degraded sunshade cannot be the exclusive cause of this solar glare. In addition, the analysis performed during the design of the instrument showed that the effects due to scattered and diffracted light were greater at the longer wavelengths than at shorter. This was just the opposite of what was observed: the largest effect was seen at 2 μm, a somewhat smaller effect was seen at $5-9$ μm, and no detectable effect was seen at $77-115$ μm. It is believed that this glare was due to scattered light external to the instrument. As with the thrusters, the large strength of the glare signal caused an electronic tail in the data which was removed using the software filter developed to deal with the electronic tail in the 2 μm data.

5. IRT EXPERIMENT RESULTS

5.1 Astronomical Results

5.1.1 S-Band (2 μm) Results

Observations at near- and mid-infrared wavelengths of the center and the plane of our Galaxy are important since, in contrast to visible light, the galactic plane is much more transparent at infrared wavelengths.

The observed spectrum of the infrared radiation from the galactic plane is shown in Figure 17 (Giard *et al.* 1988), presented as the average surface brightness in the inner Galaxy ($8.5° < l < 35°$, $|b| < 1°$). The spectral region from 1 to 4 μm is dominated by continuum radiation from stars. Recently, emission in a narrow band centered at 3.3 μm has been detected (Giard *et al.* 1988) which is present above the continuum emission. This feature is the characteristic signature of aromatic hydrocarbon molecules (Léger and Puget 1984). In the spectral region greater than 4 μm the radiation can be explained by emission from interstellar dust grains (graphite and silicon) heated by the ambient radiation field (Cox and Mezger 1989). Most of this energy appears in the 30 to 300 μm spectral regions, with a broad peak at 100 μm. Approximately 20% of the total infrared emission is present in an additional broad peak centered at 10 μm. This emission is too large to be explained by the usual dust grain emission mechanisms and has been ascribed also to the emission by aromatic hydrocarbon molecules (Puget *et al.* 1985). In this report we shall concentrate on observations of the continuum emission at near-infrared wavelengths, i.e., < 4 μm, from stars, and on what can be learned about the structure of the Galaxy from these observations.

Near-infrared radiation is emitted by relatively cool objects, T $\approx$ 2000 K, with the most abundant sources in the Galaxy being late-type stars. An estimate of the percentage contribution of various spectral classes to the surface brightness of the Galaxy at K-band (2.2 μm) is given by Jones *et al.* (1981) and Okuda (1983). The major contributors are late-type K- and M-giant stars, although early-type main sequence stars and extreme population I stars could also contribute. Late-type giant stars are part of the old, stellar population in the Galaxy, and hence knowledge of their distribution is important in the study of galactic structure and dynamics. At optical wavelengths, because of interstellar extinction, the study of these stars has been limited to a region within 3 kpc of the sun.

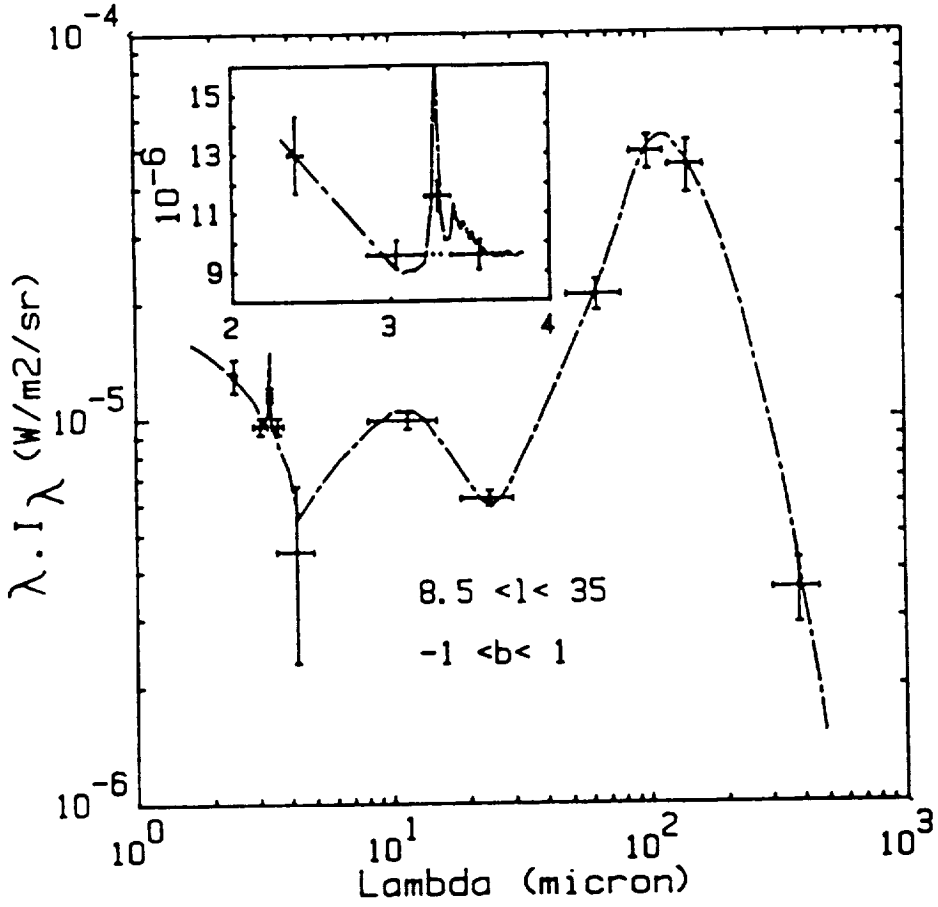

Figure 17. The averaged surface brightness (W/m^2 sr) in the inner Galaxy ($8.5° < l < 35°$, $|b| < 1°$) at infrared and submillimeter wavelengths

5.1.1.1 Results of the Near-Infrared Large-Scale Surveys

Since the early 1970's numerous observations have been performed to produce large-scale near-infrared maps of the galactic plane and center region. Most of these observations have been made by high-altitude balloon-borne telescopes of modest size, operating primarily in a relatively narrow wavelength band centered at 2.4 μm, corresponding to a spectral window in the earth's airglow

emission. A limited number of observations have also been made at longer wavelengths up to 4.8 μm; these results have been important in determining interstellar extinction. Telescope mirror diameters have been typically 20 cm or less, and angular resolutions have been in the range from 0.5 to 4 degrees.

Okuda (1981) has summarized the observational parameters of these large-scale photometric surveys conducted by groups at Nagoya University and the University of Melbourne (e.g., Matsumoto *et al.* 1982), at Kyoto University and the Institute of Space and Astronautical Science (ISAS) (e.g., Oda *et al.* 1979), the Max Planck Institute für Astronomie, Heidelberg (Hoffmann *et al.* 1978), and a combined French group (Giard *et al.* 1988). In addition, rocket-borne telescopes have been flown by the Air Force Geophysical Laboratories (AFGL; Price and Marcotte 1980) and Nagoya University/ISAS (Noguchi *et al.* 1981) and this 15-cm helium-cooled telescope was flown on the Spacelab-2 flight of the Space Shuttle by combined groups at the Smithsonian Astrophysical Observatory, the University of Arizona, and the NASA/Marshall Space Flight Center (Koch *et al.* 1988). Large-scale ground-based observations of the galactic plane using infrared source counts have been made by Kawara *et al.* (1982) using a multicolor photometer at I-, H-, K-, and L-bands; $2° \times 1°$ maps of the galactic center region in the J-, H-, and K-bands have been produced by Glass *et al.* (1987); and a 30×40 arcminute map at K-band of the galactic center by Gatley *et al.* (1989).

K-band polarization measurements have been made by Okuda (1985) at $l = 0°$, $20°$, and $30°$. The observed polarization direction was parallel to the galactic plane and the magnitude was well correlated with interstellar extinction. The dependence of polarization on H-K index varied with galactic longitude and this effect was explained by assuming the magnetic field lines are concentric with the galactic center.

The results of the balloon-borne mapping program have been summarized by Hayakawa *et al.* (1981) in a synthesized contour map of the 2.4 μm surface brightness (Figure 18*a*), extending in galactic longitude from -80° to +70°. Figure 18*b* is a blowup of the central bulge of our Galaxy as observed by a balloon-borne telescope at 2.4 μm with a spatial resolution of 0.4° (Hiromoto *et al.* 1984). A similar map of the bulge was also made earlier by Matsumoto *et al.* (1982) with an angular resolution of 0.5°.

The Spacelab-2 IRT maps at 2.4 μm (Koch *et al.* 1988), which extend in galactic longitude from $-10°$ to +130°, are presented in Figures 19*a* and 20*a*, and

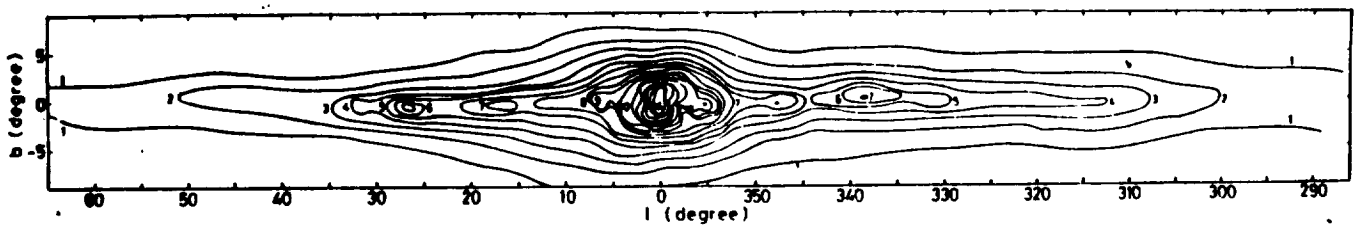

Figure 18*a*. The synthesized 2.4 μm surface-brightness map of the galactic plane

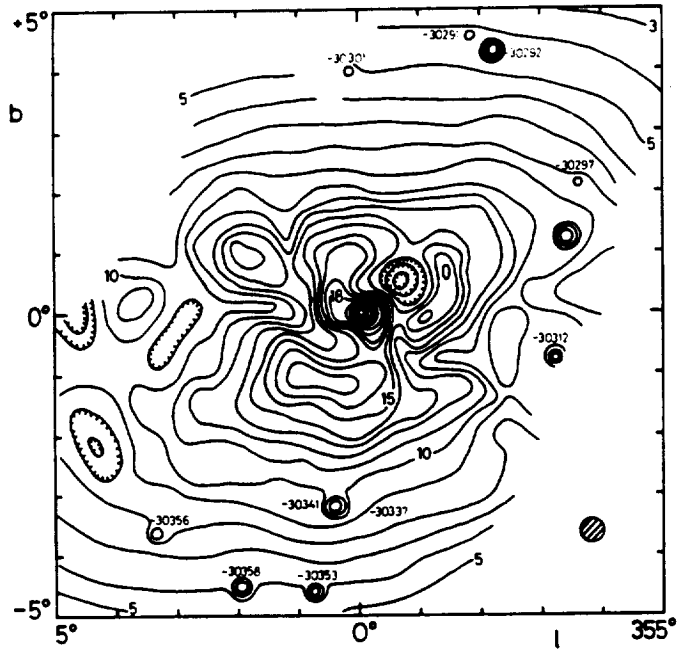

Figure 18*b*. The 2.4 μm surface-brightness map of the central 10° of the Galaxy

the region of the galactic bulge is shown in Figure 20*b* (Melnick *et al.* 1987). In the 2 μm band, coverage was obtained of approximately 60% of the galactic plane, $-10° < l < 130°$ and $250° < l < 310°$, and 75% of the sky. This band was originally intended for star identification using an N-slit mask and was not

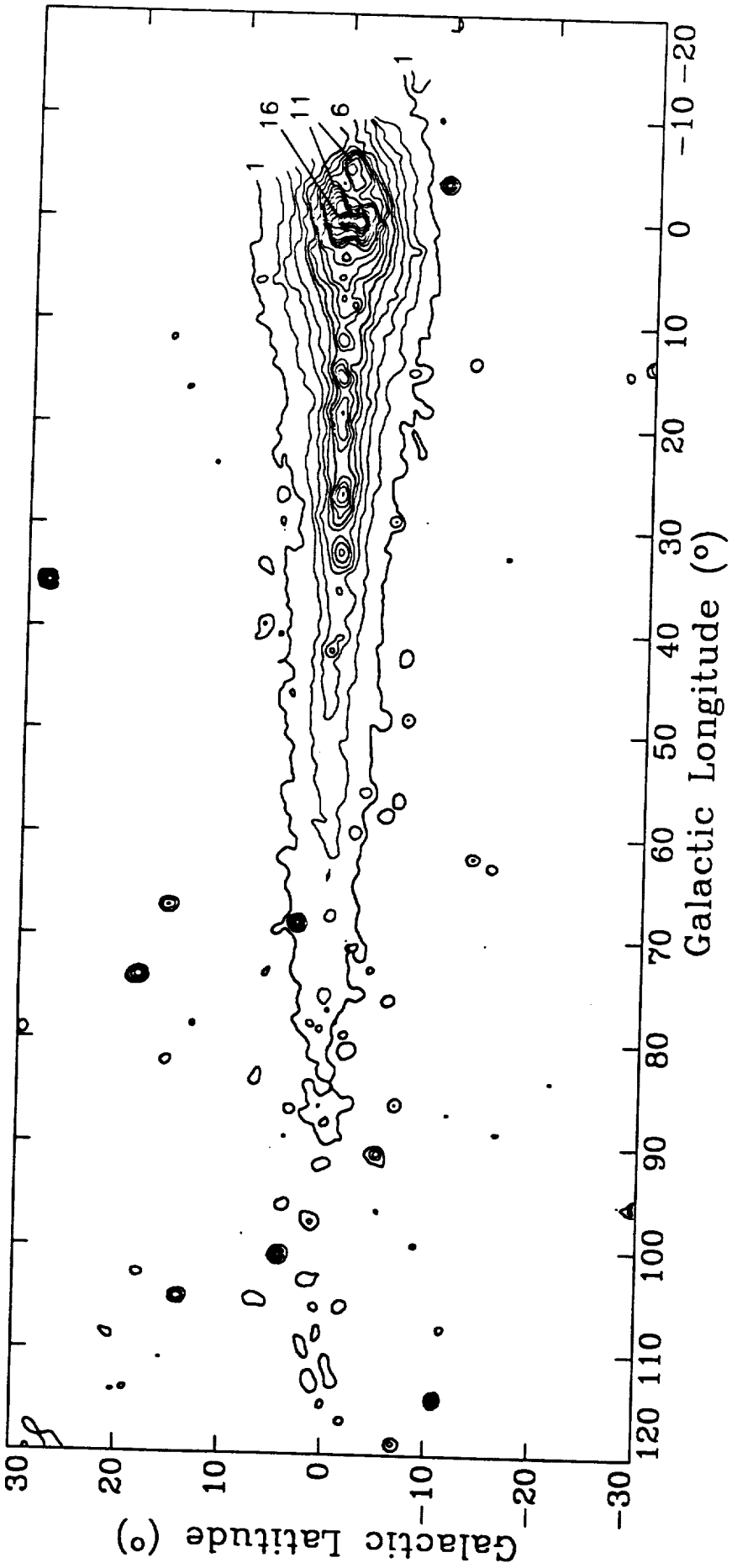

Figure 19*a*. The Spacelab-2 IRT map of the 2.4 μm surface brightness of the first quadrant of the galactic plane (Koch *et al.* 1988). The contours are labelled in units of 1.4×10^{-10} W/(cm^2 sr μm).

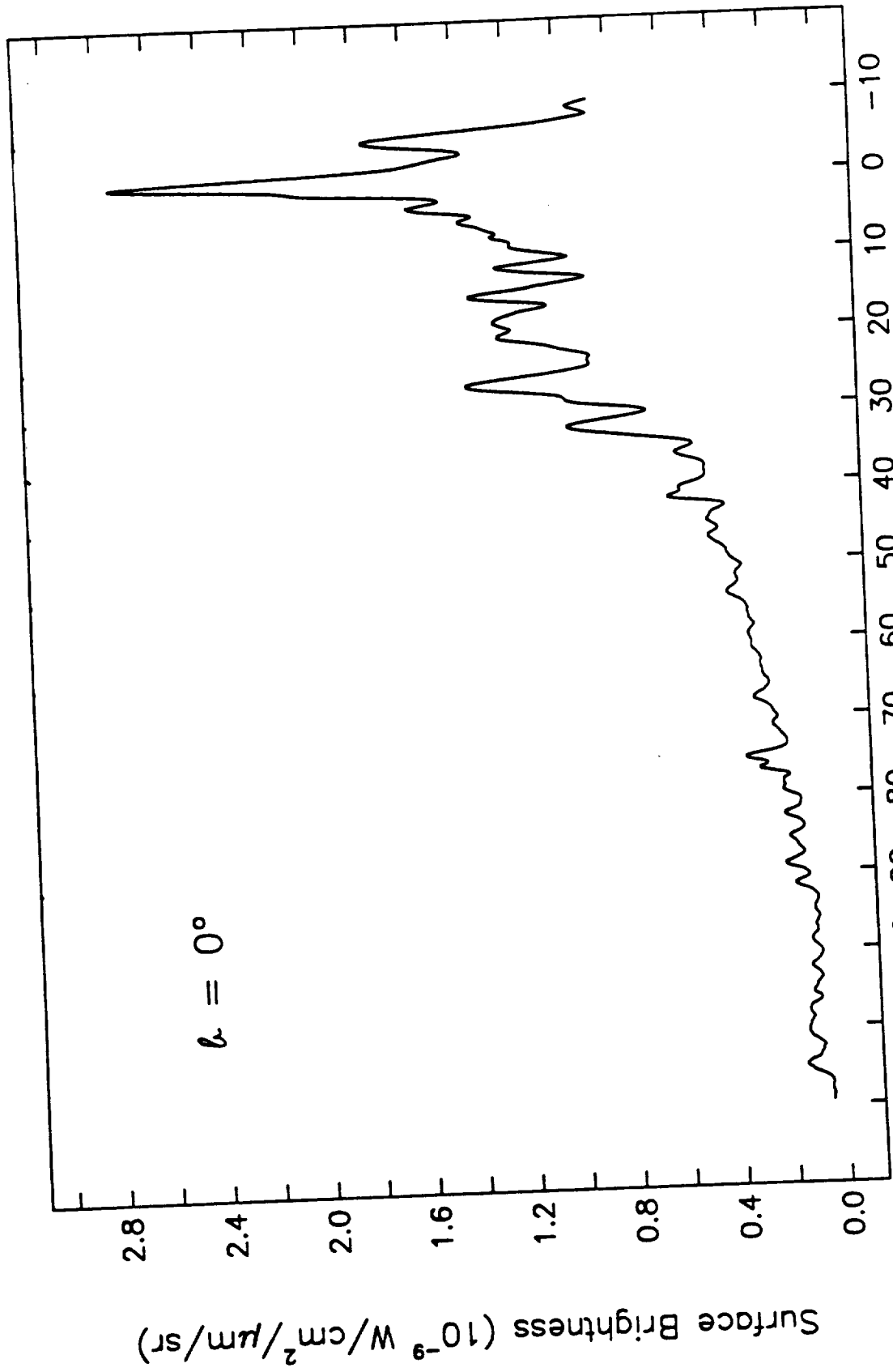

Figure 19*b*. The Spacelab-2 IRT longitudinal distribution of the 2.4 μm surface brightness at a galactic latitude b = 0° (Koch *et al.* 1988).

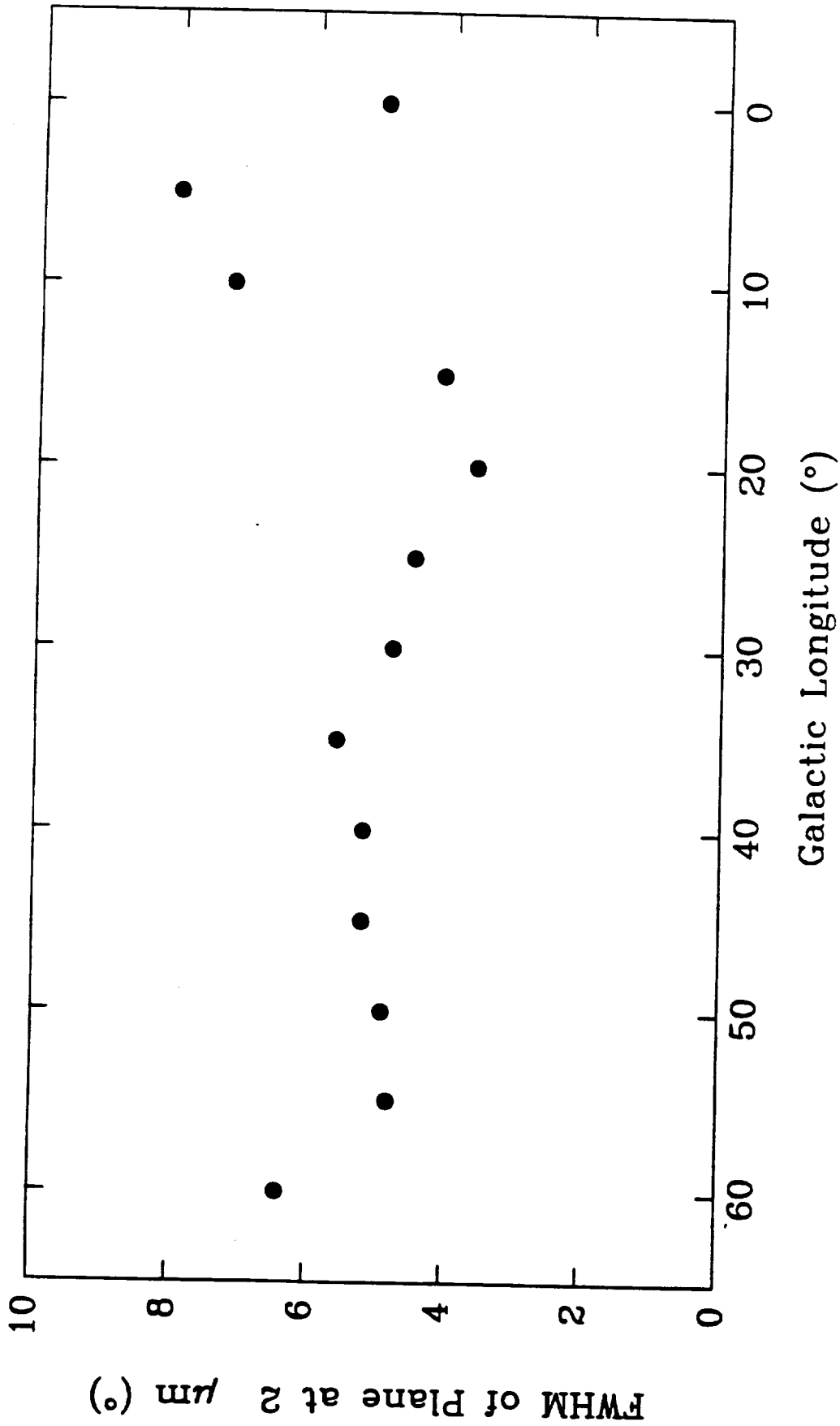

Figure 19c. The full width at half maximum in degrees of the 2 μm surface brightness perpendicular to the galactic plane as a function of galactic latitude.

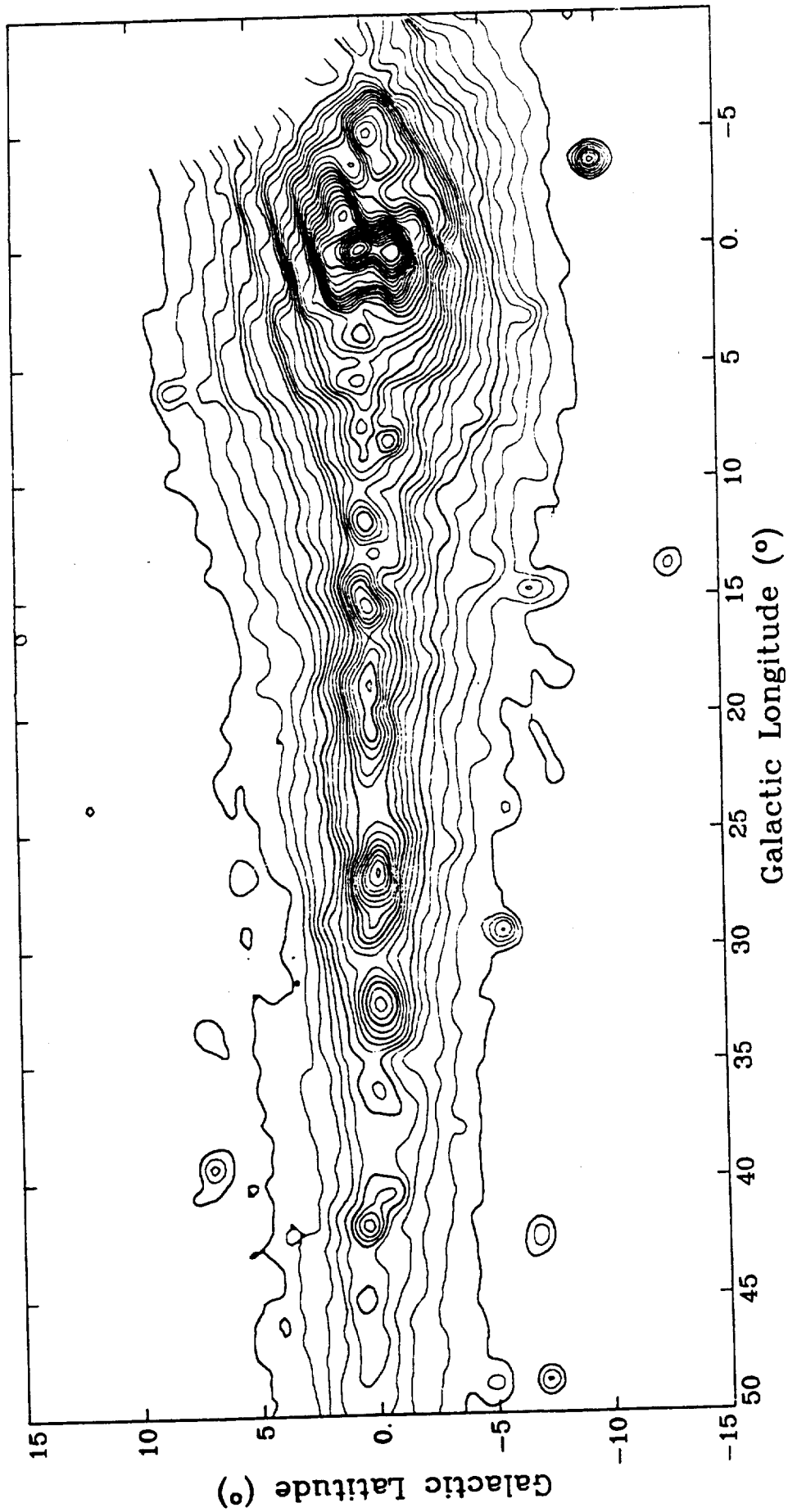

Figure 20*a*. The Spacelab-2 IRT map of the 2.4 μm surface brightness of the inner disk of the Galaxy. The contours are labelled in units of 1.4 × 10^{-10} W/(cm^2 sr μm).

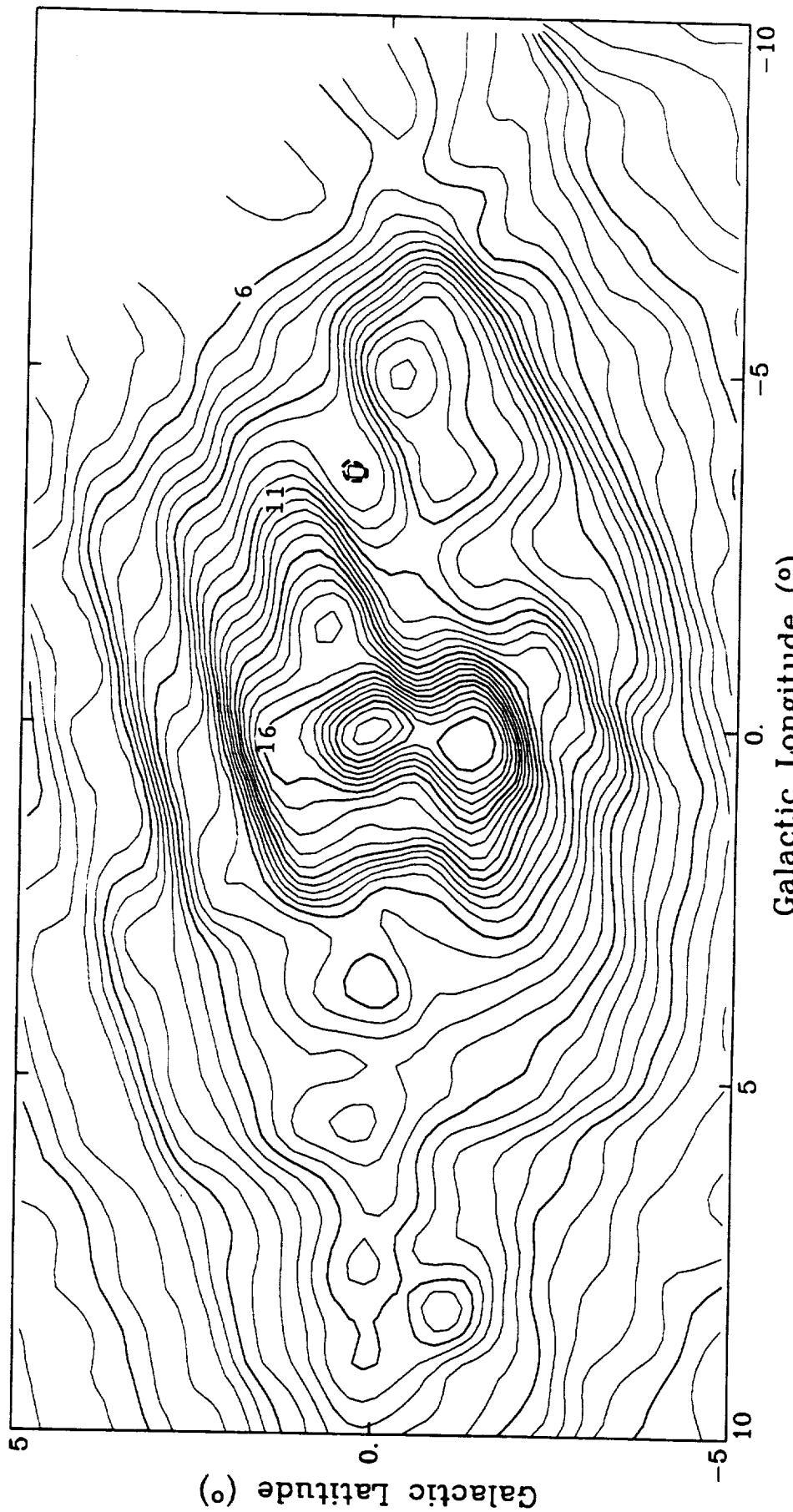

Figure 20*b*. The Spacelab-2 IRT map of the 2.4 μm surface brightness of the central 10° of the Galaxy (Melnick *et al.* 1987). The contours are labelled in units of 1.4×10^{-10} W/(cm^2 sr μm).

optimized for measuring the diffuse radiation. A large local background radiation was seen in this band, which at its lowest was 1.4×10^{-10} W/cm^2 sr μm, 20 times the zodiacal light level. The measured noise equivalent flux density (NEFD) in the region off the plane in Figure 16 was 5×10^{-17} W/cm^2 μm Hz$^{1/2}$. The angular resolution of these maps has been smoothed to approximately 1 degree. Isolated point sources can be located to several arcminutes. Point sources brighter than about -0.5 magnitude can be readily identified. The region on the map to the right of $l = -5°$ and above the plane was near the pole of the orbit ($l = -25°$, $b = 11°$) and could not be viewed. A profile of the 2 μm band surface brightness along the plane ($b = 0.0°$) is shown in Figure 19*b*.

Compared to the balloon-borne telescope maps the IRT data have the advantages of (a) being free from airglow contamination, (b) having a long baseline for photometric measurements, since scans were taken from the galactic plane to the pole, (c) excellent position information, (d) more uniform sensitivity calibration over the sky, and (e) measurements to galactic longitude 130°, which permit comparison of the luminosity distribution in the galactic center region with that in the solar neighborhood. The IRT also incorporated a cold shutter for absolute zero-point calibrations.

These maps have the general appearance of an edge-on spiral galaxy; however several important features should be noted:

(a) Galactic Bulge

The "bulge" is that volume of stars in our Galaxy surrounding the galactic center with an outer radius of about 1 kpc. Assuming a distance of 8 kpc to the galactic center, 1 kpc corresponds to a subtended angle of 7°. Frogel (1988) has summarized the optical and infrared properties of the bulge. Figures 18*b* and 20*b* show detailed near-infrared maps of this region. Additional near-infrared maps and analyses of the bulge have been made by Matsumoto *et al.* (1982); Harris *et al.* (1980); and Little and Price (1985). These maps show that the surface brightness distribution can be represented by an ellipsoid with major axis along the plane, with an axial ratio of about 0.7. At a galactic longitude of +10° the IRT data give a latitudinal width (FWHM) for the bulge of 8°. The infrared maps also show considerable structure, which can be explained by variable interstellar extinction along the line of sight, rather than by enhanced source emission. This extinction is probably due to giant molecular clouds. Ground-based near-infrared observations have shown similar results (Glass *et al.* 1987). Matsumoto *et al.* (1982) have proposed that these clouds are in a molecular ring with a radius of

300 pc around the galactic center. The infrared data can also be used to determine the bulge luminosity, mass, and mass/luminosity ratio. Previous estimates of M/L_v have ranged from 2.0 (Matsumoto *et al.* 1982) to 4.0 (Harris *et al.* 1980).

At the galactic center, within $\pm 0.2°$, there exists an additional concentration of near-infrared sources that exceeds the extrapolation of the bulge and disk stellar populations (Becklin and Neugebauer 1968; Okuda 1985; Catchpole *et al.* 1989; Gatley *et al.* 1989). Heavy, patchy extinction is also present in this region (Lebofsky 1979) and Gatley *et al.* (1989) have shown that the heavy extinction to the southwest of the nucleus correlates well with the circumnuclear molecular ring. A review of the stellar population in the galactic center has been given by Rieke (1989).

(b) Inner Thin Disk

This component of the near-infrared radiation extends from the galactic center region to a rather sharp cutoff at galactic longitude $\pm$ 30°, having a latitudinal width (FWHM) of about 3.5° as measured from the IRT data (Figure 19*c*). The width would be even thinner if corrected for extinction and line-of-sight effects; some preliminary modeling of these effects shows that the corresponding exponential scale height is of the order of 150 pc. This value is much less than the 300 – 400 pc exponential scale height of K- and M-giant stars in the solar neighborhood. Along the plane the infrared data show a peak at galactic longitude $\sim$ 27°, tangent to the broad peak in the molecular gas density at 4 kpc. At longer wavelengths both the IRAS data (11 and 25 μm) and the AFGL data, which measure primarily long period variable stars with very high mass loss rates, show similar results, with an exponential scale height of 250 pc for the inner disk (Habing 1988). Similar distributions are observed in the radio continuum, CO, far-infrared, and gamma-ray data. There are also conspicuous enhancements in the near-infrared flux in the thin disk which were once thought to correspond to tangential views of the spiral arms. But as shown later (Figures 21 and 22) these enhancements correspond to minima in the interstellar extinction, i.e., to regions between the spiral arms.

An exponential function for the radial distribution of stellar emission, fitted to the outer disk, beyond $l = \pm$ 30°, when extrapolated to the inner disk, falls well below the observed intensity. Additional sources, other than the predicted K- and M-giant population, are needed. The thinness of this disk is also difficult to explain. It is not clear whether the excess emission is due to a population of

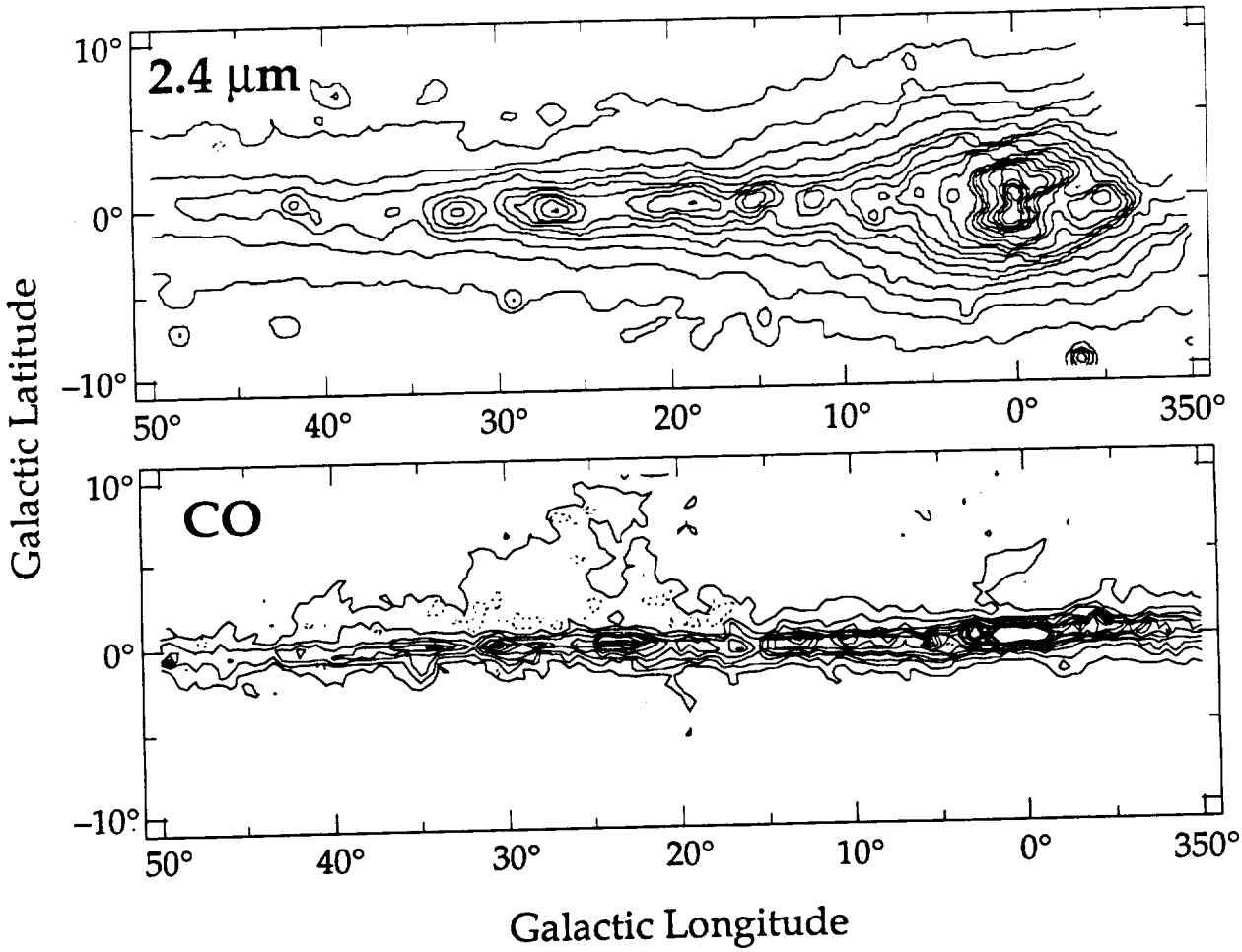

Figure 21. Comparison of the 2.4 μm and CO integrated intensity maps. The 2.4 μm contours range from 1.4 × 10^{-10} W/(cm^2 sr μm) in unit steps. The CO data were taken from the survey of Dame *et al.* (1987); the contours range from 10 to 400 K km/s in steps of 20 K km/s.

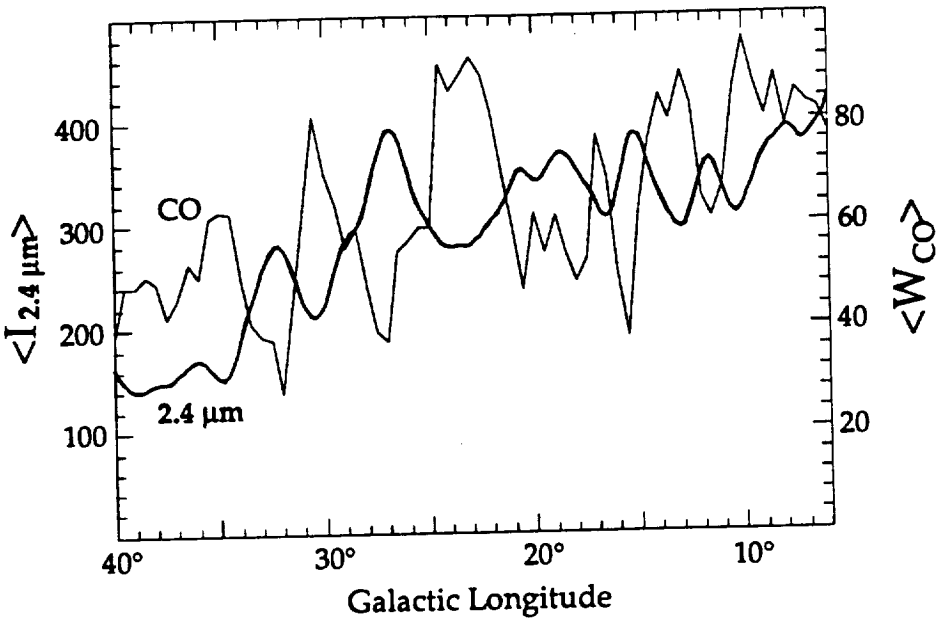

Figure 22. Comparison of the 2.4 μm and CO longitude profiles. The CO intensity, from the survey of Dame *et al.* (1987), has been integrated over all velocities, and both curves have been averaged from −1° to +1° in galactic latitude. W_{CO} is in units of K km s^{-1}; $I_{2.4}$ is in units of 2.8 × 10^{-12} W/(cm^2 sr μm).

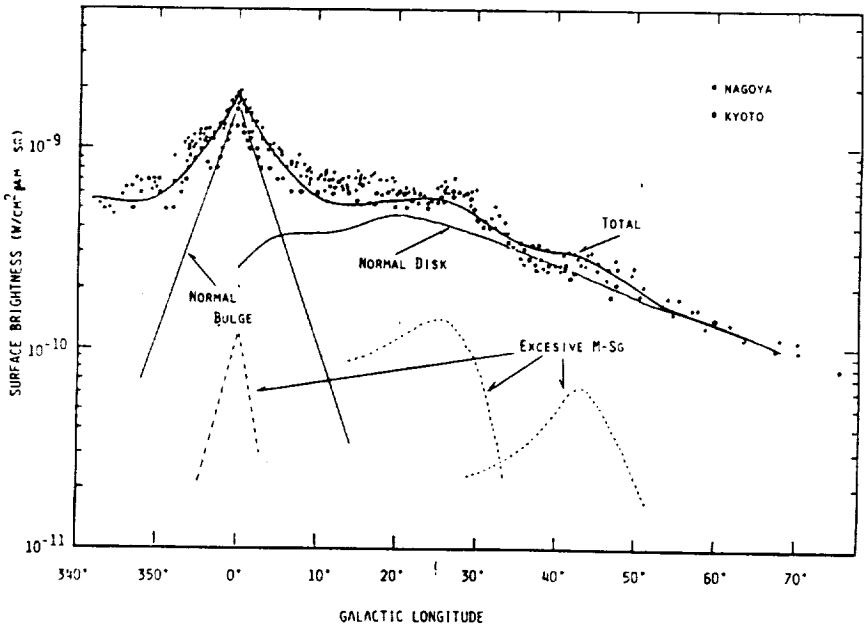

Figure 23. Model of 2.4 μm surface brightness distribution calculated by Okuda (1983) compared to the data from the Nagoya and Kyoto balloon-borne telescope experiments.

young M-supergiant stars associated with the enhanced star formation or to an overall increase in the old disk stellar density.

(c) Outer Disk

The outer disk is a more extended stellar component, detectable out past 90° in galactic longitude with a thickness of 5° (FWHM) (Figure 19*c*); preliminary modeling of the outer disk shows that the corresponding exponential scale height is about 300 pc. This thickness is comparable to the scale height of K- and M-giant stars. The outer disk is probably the same disk observed optically in the solar neighborhood. IRAS also observed a thick, more extended disk, but with an exponential scale height of 680−1600 pc. The IRAS objects cut off suddenly at about $|l| > 90°$, which corresponds approximately to the distance of the sun from the galactic center (Habing 1988).

5.1.1.2 Absolute Calibration of the Near-Infrared Flux

Frogel (1988), in his review article on the galactic bulge, suggests that a possible systematic error exists in the surface brightness (W/cm^2 sr μm) balloon measurements of Hiromoto *et al.* (1984) (Figure 18*b*), because they are a factor of two higher than the surface brightness inferred from ground-based measurements. In the galactic bulge region the IRT data agree in intensity with the data of Hiromoto *et al.* (1984). In the combined Nagoya/Kyoto balloon data (Okuda 1983; Figure 23) there exists an internal scatter of about a factor of 1.5. From $|l| = 30°$ to 40° the IRT data are about a factor of 2 higher than the balloon data summarized by Hayakawa *et al.* (1981) and shown in Figure 18*a*. These differences have to be investigated further, and the IRT data will be recalibrated.

5.1.1.3 Comparison of Near-Infrared and CO Observations

Dame *et al.* (1987) have mapped the galactic CO distribution with a resolution comparable to that of the IRT map (Figure 21). An important preliminary result of our comparison of these surveys, shown in Figure 22, is the strong anticorrelation of the intensities of CO and 2.4 μm emissions toward the inner Galaxy, the CO peaks corresponding to 2.4 μm holes and vice versa. Although this result has been suggested before (Okuda 1981; Harris *et al.* 1980; Glass *et al.* 1987), it has never been so dramatically exhibited over such a wide range of galactic longitude. It strongly suggests that the 2.4 μm emission is coming from an old population of stars not directly associated with molecular clouds. Just as small, nearby molecular clouds are silhouetted against the optical light of the disk, in Figure 22 many giant molecular complexes in the inner spiral arms of the Galaxy are evidently silhouetted against the more penetrating infrared light of the disk. Further, just as star counts provide information on the distances to very nearby molecular clouds, a detailed model of the 2.4 μm emission based on 21-cm and CO surveys and the infrared light distributions discussed below (Section 5.1.1.4) can provide information on the distances to large atomic and molecular complexes throughout the Galaxy and so yield a rough three-dimensional map of the galactic extinction. The modeling will also yield a value for the ratio of absorption at 2.4 μm, $A_{2.4}$, to the CO emissivity, W_{CO}. In a preliminary two-dimensional model of this sort, we found that the 2.4 μm emission can be reasonably well fit using standard values for the ratios $N(H_2)/W_{CO}$ (2.3×10^{20} cm^{-2} K^{-1} km^{-1} s; Strong *et al.* 1988), $N(H)/A_v$ (1.9×10^{21} cm^{-2} mag; Bohlin *et al.* (1978) and $A_{2.4}/A_v$ (13.6; van de Hulst, 1957). Future three-

dimensional models with more sophisticated infrared light distributions should provide useful constraints on these ratios.

5.1.1.4 Galactic Models

For edge-on spiral galaxies, the spatial distribution of the infrared surface brightness in cylindrical coordinates, $\nu(R,z)$, can be represented by the equation:

$$\nu(R,z) = \nu_o \exp\left(\frac{-R}{h}\right) \operatorname{sech}^2\left(\frac{z}{z_o}\right) \tag{1}$$

For $z/z_o \gg 1$:

$$\operatorname{sech}^2\left(\frac{z}{z_o}\right) \approx 4 \exp\left(\frac{-2z}{z_o}\right); \quad \text{and } z_{\exp} = \frac{z_o}{2}$$

(van der Kruit and Searle 1981), with three adjustable constants (υ_o, h, and z_o), where h and z_o are the scale lengths in the radial direction and normal to the plane, respectively.

For the galactic bulge light distribution, a reasonable approximation is that the projected light distribution or surface brightness, μ, follows the equation:

$$\mu = \mu o \exp\left(-s/h_B\right), \tag{2}$$

$$\text{where } s = \left[\frac{R^2 + z^2}{(1-\epsilon)^2}\right]^{1/2},$$

where ϵ is the ellipticity of the spheroidal bulge, and μ_o, h_B, and ϵ are adjustable parameters.

From the results of the balloon-borne large-scale near-infrared surveys various authors have inferred the stellar mass distribution of the inner Galaxy. A summary of early models and of the interpretation of the large-scale emission from the galactic plane has been presented by Drapatz (1981).

Okuda (1983; 1985), by combining balloon-borne and ground-based near-infrared observations, constructed a comprehensive model of the inner Galaxy based on a bulge plus disk contribution. To explain the large flux near the galactic center (i.e., within ~20 pc), an additional component had to be added with a population of very luminous M-giant or M-supergiant stars about 100 times higher than the fraction found in the solar neighborhood. Evidence for an overpopulation of luminous giants in the central 20 pc of the Galaxy has also been found by Lebofsky and Rieke (1987). To explain the peak in the longitudinal distribution of the surface brightness observed at l = 27°, an appreciable concentration of very luminous M-giants or M-supergiants was proposed in an annulus located at 4 kpc from the galactic center. Near-infrared star counts in this region seem to confirm this assumption. In Okuda's model the excess can be explained only by assuming a luminous M-giant overpopulation by a factor of 20 compared to the average population in the solar neighborhood. A problem with these assumptions is that the expected excess of early-type O- and B-supergiants is not present. A summary of Okuda's model is shown in Figure 23.

Oda (1985) modeled the distribution of stellar radiation in the 4-kpc ring assuming that the 2.4 μm volume emissivity is dominated by M-giant and M-supergiant stars with 80% of the emissivity due to M-giants heavier than 2 to 3 M_o, i.e., evolved late B or early A stars. This theory incorporates a bimodal star-formation model, proposed by Güsten and Mezger (1982), in which only medium and high mass stars form in spiral arms and low mass stars form in the interarm regions. All stars heavier than a few solar mass are assumed to have the same spatial distribution and hence a scale height distribution and a number density ratio similar to OB stars.

Estimates of some of the scale parameters in the above equations for our Galaxy have given amazingly disparate results. For example, the estimates of the radial exponential scale length, h, of the disk range from 2.2 kpc (Jones *et al.* 1981) and 2.3 kpc (Okuda 1983) to 5.5 kpc (van der Kruit 1986). At least three reasons for such discrepant results can be identified. First, the disk is not perfectly exponential, and the different estimates refer to different parts of the Galaxy: the 2.2 and 2.3 kpc estimates refer approximately to R < 5 kpc while the 5.5 kpc estimate refers to the solar neighborhood (R ≈ 8 kpc). There are notable deviations from the exponential law in the near-infrared emission at l = 30°, corresponding to the 4 kpc ring of molecular gas. Second, there have been variations in the absolute near-infrared flux measurements by various groups. Third, corrections for interstellar absorption have not properly allowed for the fact that the dust distribution is clumpy (effectively reducing the total opacity

compared with an assumption of uniform distribution); none of the models has included such a correction.

Using the Spacelab-2 IRT data a more accurate measure of the global scale parameters should be possible, and a new model for the three-dimensional light distribution can be derived. Using the IRT data and CO maps in tandem, a more accurate 3-dimensional map of galactic extinction for $l > 20°$ can be derived, which can then be incorporated into the model. The model will also incorporate the following features: deviations in the radial disk profile from exponential; variations in the vertical scale height, z_o, with radius; deviations of the vertical distribution of light from a sech^2 law; and geometrical considerations due to our position in the Galaxy.

Using the IRT data to fit the adjustable parameters, preliminary calculations (using a simple dust extinction model) have given the following results (Figures 24*a*,*b*,*c*). For the outer galactic disk the following parameters for equations (1) and (2) have been determined:

$$h = 4\ kpc; \quad z_o = 600\ pc; \quad z_{\exp} = 300\ pc; \quad \mu_o = 177\ \frac{L_o}{pc^2}\ ,$$

where μ_o is the V-band surface brightness, assuming a value V-K = 3.2. In the solar neighborhood the V-band surface brightness was determined to be 24 L_o/pc^2, in agreement with direct star counts (Bahcall 1984). Using $M/L_v = 3$, the total disk luminosity is 1.8×10^{10} L_o and the total disk mass is 5.3×10^{10} M_o.

For the galactic bulge, assuming $\epsilon \approx 0.35$, the parameters are:

$$h_B = 540\ pc; \quad \mu_o = 4200\ \frac{L_o}{pc^2},$$

giving a total bulge luminosity of 4×10^9 L_o. Assuming a projected stellar velocity dispersion of 122 km/s at z = 600 pc, the value of M/L_v derived is 4.6.

This model however, does not incorporate the enhanced emission in the galactic center or the excess emission in the inner disk.

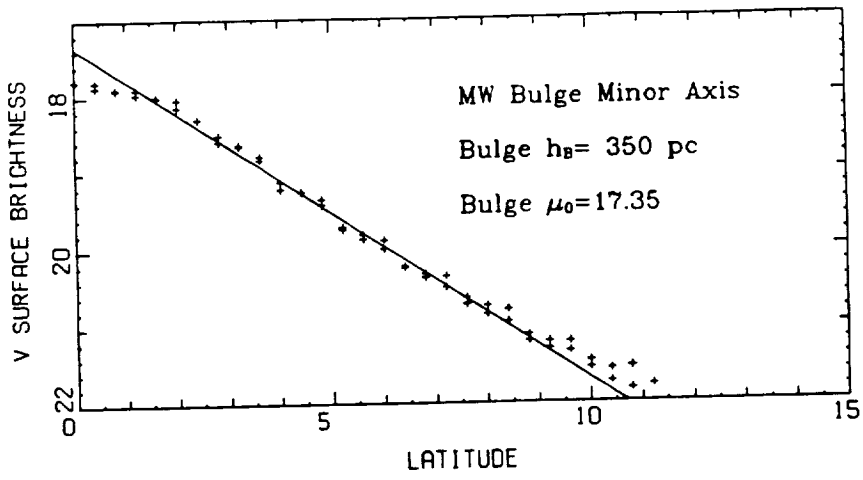

(a)

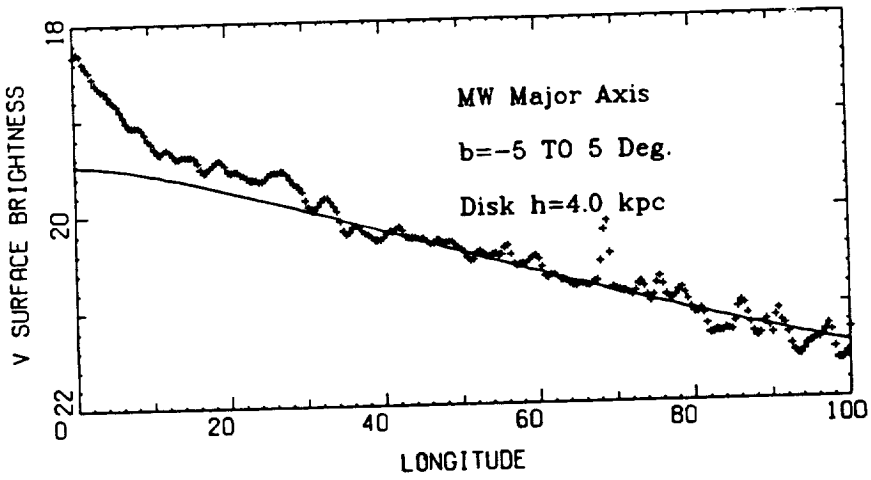

(b)

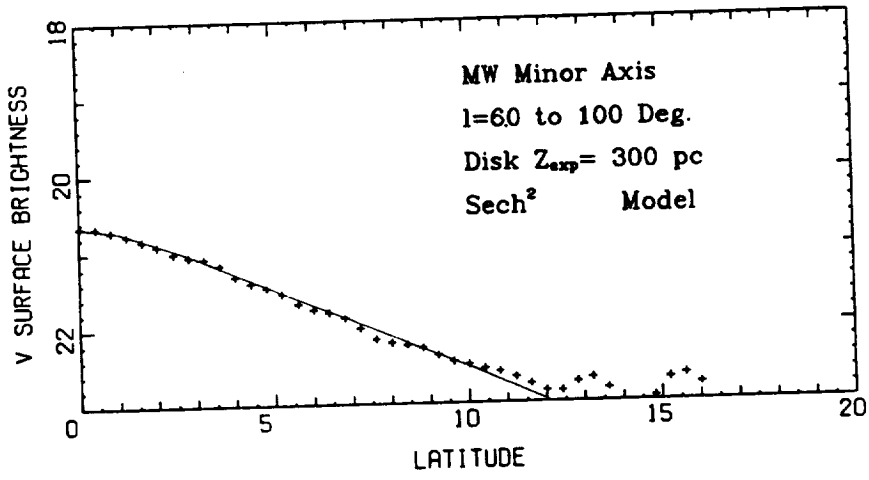

(c)

Figure 24*a,b,c*. Comparison of the model and observed 2.4 μm data from Spacelab-2 for (*a*) the galactic bulge minor axis; (*b*) the galactic disk major axis (R); and (*c*) the galactic disk minor axis (z). The ordinate is the V-band intensity in units of mag/arcsecond^2.

5.1.1.5 Future Programs

When a more careful and detailed analysis of the Spacelab-2 IRT data is carried out, we expect to be able to derive a number of useful results. These include:

(a) Distribution of dust in galactic disk;

(b) A value for the 2.4 μm absorption-to-CO emissivity ratio, $A_{2.4}/W_{CO}$, which will constrain the more important ratios $N(H_2)/W_{CO}$ and $A_{2.4}/A_v$;

(c) Structural parameters of the Galaxy;

(d) Comparison of the galactic luminosity distribution with the mass distribution.

(e) Comparison of near-infrared emission with long-wavelength IRAS emission to determine if the emission peak at $l = 30°$ is due to a population of young supergiants associated with enhanced star formation or to an overall increase in the old disk stellar density;

(f) A better understanding of bulge dynamics;

(g) Comparison of the near-infrared luminosity profiles of our Galaxy with other galaxies. As an auxiliary part of the program, ground-based optical (S. Kent) and infrared images (G. Rieke) of external galaxies similar to our Galaxy have been obtained in order to learn which galaxies have bulge and disk luminosity profiles most like those of the Milky Way, and to determine, among other things, the range of variability of bulge luminosity profiles.

These results have also been published in the Proceedings of IAU Symposium 139, *Galactic and Extragalactic Background Radiation* (Fazio *et al.* 1989).

5.1.2 A-Band (7 μm) Results

Coverage in the 7 μm band exists for approximately 40% of the galactic plane and 50% of the sky. These data are limited to observations from only the second day of the mission, which was prior to the mylar strip entering the beam. The typical background flux measured in the IRT 7 μm band was approximately 5 $\times$ 10^{-10} W cm^{-2} sr^{-1} μm^{-1}, three times higher than the lowest flux observed for a short period later in the mission. This high background is attributed to the locally induced environment. The in-flight NEFD for the 7 μm band was 8 $\times$ 10^{-18} W cm^{-2} μm^{-1} $Hz^{-1/2}$. The 1σ sensitivity was 2 $\times$ 10^{-13} W cm^{-2} sr^{-1} μm^{-1}.

The portion of the data providing coverage in the Cygnus region of the plane is shown in Figure 25. Previous observations of the diffuse emission of the galactic plane at 11 and 20 μm were obtained by Price *et al.* (1982), who mapped the plane between 73° and 87° longitude with a beam of about 11 arcminutes. The lowest contour on their 11 μm map was 1.5 $\times$ 10^{-11} W cm^{-2} sr^{-1} μm^{-1}. This region has also been mapped in CO by Cong and Thaddeus (Campbell *et al.* 1980). Many of the features seen at 7 μm in Figure 25 can be associated with the features seen in the mid-IR and radio surveys.

5.1.3 E-Band (100 μm) Results

Survey data in the 100 μm band were available from two of the three 100 μm detectors. As with the 2 μm data, approximately 60% of the galactic plane was mapped, including the galactic center and 75% of the sky. The angular resolution is approximately 0.2°. The NEFD was 9 $\times$ 10^{-20} W cm^{-2} μm^{-1} $Hz^{-1/2}$ or 6 $\times$ 10^{4} Jy/sr for 1σ sensitivity in a single scan. IRAS mapped the sky in a similar wavelength region and for comparison the IRAS 1σ flux in a 0.5 degree synthesized beam in the 100 μm band was 5.6 $\times$ 10^{4} Jy/sr. Thus, the IRT compares quite favorably with the IRAS sensitivity (Neugebauer *et al.* 1984) for a large beam. The origin of the high background in this band is now believed to be due to radiation from the 50K forebaffle being scattered off of the mirror (discussed below). In fact, had there not been this problem, the NEFD would have been a factor of two better, since with the cold focal-plane shutter closed, it was 5 $\times$ 10^{-20} W cm^{-2} μm^{-1} $Hz^{-1/2}$.

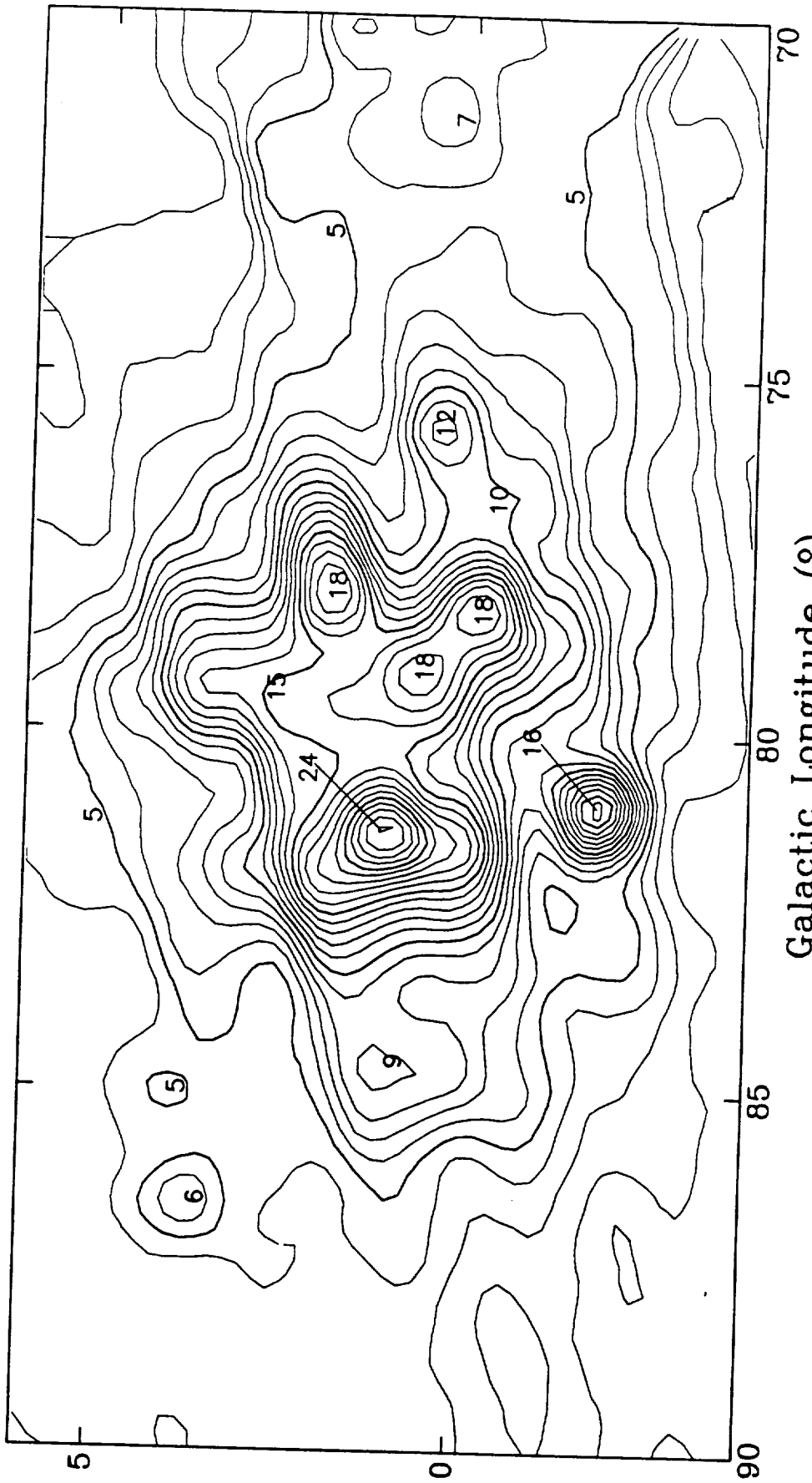

Figure 25. Map of the 7 μm surface brightness in the Cygnus region. The intensity contours are to be multiplied by 5×10^{-12} W/cm^2/μm/sr.

5.2 Shuttle-Induced Environment

One of the primary objectives of this instrument was to measure the Shuttle-induced environment and place important limits on the IR background in the vicinity of the Shuttle. The unexpectedly high background flux discussed above is presumably of local origin. The following are preliminary results on other discrete effects:

5.2.1 Observing Pre-Conditioning

There are many known and expected sources of contamination on the Shuttle, which presumably can be controlled. By anticipating these, it was hoped that they could be reduced to an acceptable level. Anticipating a tremendous amount of outgassing due to entrapped air and volatiles as well as some amount of material outgassing, the beginning of IRT observations was not planned until about two days into the mission. In addition, there were a number of controllable Shuttle effluents. These included water dumps, water from the flash evaporator system (FES) used for cooling the Shuttle, and thruster firings. The water dumps and FES had been inhibited for at least a half hour prior to IRT observing. Only vernier thruster firings were permitted. Although not a source of contamination but rather a loss of science data, radiation from the South Atlantic Anomaly was minimized by choosing those orbits each day which avoided the SAA for the most part.

Finally, the Shuttle was flown in the XVV or airplane mode with the nose in the forward velocity direction and pitched slightly up by 2.5 degrees. This attitude was selected because it is fairly stable and minimizes thruster firings and hence potential contamination. Also, in this attitude the velocity vector is below the lip of the sunshade.

5.2.2 Shuttle Specifications

The goals set by the STS Contamination Control Requirements for the gaseous environment (Simpson and Witteborn 1977) are column densities of:

10^{11} molecules/cm^2 of H_2O plus CO_2,
10^{13} molecules/cm^2 of O_2 plus N_2, and
10^{10} molecules/cm^2 of any other species.

For particulates the goal was set to be a limit of

> *"an average of less than one discernible particle per orbit entering a 1.5×10^{-5} sr field of view along any line within 60 degrees of the +Z-axis and this field contains no discernible particles for 90% of the operational period. A discernible particle is a particle with diameter of 5 microns within a range of 10 kilometers."*

Figure 1 shows the expected flux due to the zodiacal light, both scattered and emitted, as well as the emission from a column density of 10^{11} mol/cm^2 of CO_2 and 10^{12} mol/cm^2 of H_2O. In addition, the spectral bandpasses of the IRT detectors are given. If the column densities were to be less than those quoted, then the instrument should have been limited only by the zodiacal light.

5.2.3 Observing Synopsis

Launch occurred on Day 210 of 1985 at 21:00 GMT. When the cover on the telescope was opened for the first time at 212/19:40 a very high background was detected. In fact the C- and D-band detectors were saturated. During the subsequent 4 hours the flux in the A- and B-bands continued to drop and the C-band flux appeared to be just into saturation by the end of the first observing period. In an attempt to understand the background the observing plan was modified. The pre-mission attitudes are listed in Table 5 and the as-flown attitudes are given in Table 6.

In addition to the prime observing periods when the telescope was scanning and mapping, the cover was opened a number of other times to determine the background levels. At these times, there were no special constraints permitted with respect to contamination control, although there were no dumps or FES operations during these periods. These opportunities were used twelve times.

However, only during the first three were there any useful data obtained. These additional intervals are given in Table 10.

Table 10. Miscellaneous Observing During Inertial Pointing of the Shuttle

Day/GMT	Name	Day/Night	Scanning	R.A.	Dec.
213/07:04–09	GC1	Night	Yes	17^h20^m	+20 to
				20^h30^m	-21
213/13:42–57	Vela 1	Day	No	5^h40^m	-25
214/14:00–14	Vela 2	Day	No	5^h30^m	-23

5.2.4 S-Band (2–3 μm) Contamination Features

The S-band flux was consistently high on every observation that was made. Many of the synoptic features in the 2 μm data can be seen in Figure 26 (note the splits in the time scale). This figure is a result of extracting the minimum amplitudes in each one-minute interval of data. In general most of the effects of thrusters were excluded as well as any small astronomical features. What is left is the large-scale trends in the flux. The data in this band exhibited a number of general features.

1. This band did not show a large day/night effect in the background level, although the night side did typically show a small downward trend on each orbit.

2. The day side was dominated by scattered sunlight out to about 75 to 90 degrees from the sun.

3. The general background level did not exhibit any general decrease with time, although the night side level was somewhat different from day to day.

4. The 2 μm data were affected the most severely by thruster firings due to an electronic tail in the signal that had an e-folding time constant on

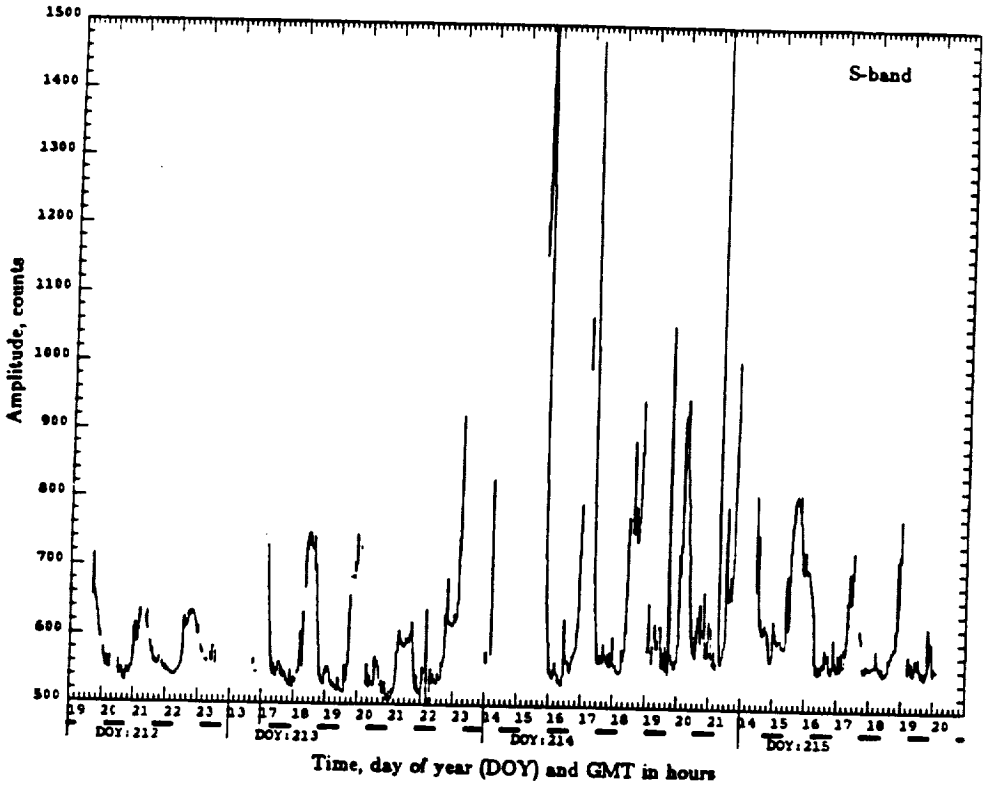

Figure 26. Samples of the minimums for the S-band (2–3 μm) flux. The zero flux (shutter closed) level was at about 510 counts. Note the splits in the time scale. The dark bars indicate orbital night. The large peaks on the day side are due to "solar glare." The small peaks on the night side are due to broad emission from the galactic plane.

the order of 20 seconds. The thruster firings drove the detector output to an amplitude that was very often many thousands of times more intense than the general background or any known astronomical source other than the sun or moon.

5. These data did not appear to show any asymmetry across the payload bay as the telescope scanned.

6. The persistent feature that appears on every night side pass is due to the galactic plane which at 2 μm has been found to be much more extended than at 100 μm.

The flux from the scattered sunlight was due entirely to material in the vicinity of the Shuttle. This was unequivocally determined on Day 215 when the Shuttle was pitched 40 degrees nose down and then 50 degrees nose up. In the nose down case, the telescope was able to scan the sky at an elongation from the sun of less than 75 degrees while the sun was below the horizon without measuring any "solar glare." Just as sunrise occurred, the "solar glare" appeared in the data. Likewise, in the nose up case, the sun set while the telescope was scanning at an elongation of 56 degrees from the sun. And just as sunset occurred, the "solar glare" disappeared from the data.

5.2.5 A-Band (4.5–9.5 μm) and B-Band (6–7 μm) Contamination Features

These two bands are treated together, since their general character is very similar. A synoptic plot of the background in the A- and B-bands is shown in Figure 15. These plots were generated in the same way as the S-band plot, by finding the minimum during each one minute of time. The only times when these bands were not saturated were during the first XVV mapping on Day 212 and during the inertial pointing times listed in Table 10. It is believed that the primary reason that these bands were saturated during the later prime XVV observing periods was due to a piece of mylar hanging in the beam. The data in these bands exhibited the following general features:

1. This band showed a large day/night effect in the background level with a large decrease during the night followed by an increase during the day side of each orbit.

2. The minimum on each orbit occurred about five minutes after sunrise. This large lag between sunrise and the turnaround in the flux decrease is most likely due to the time constant for heating of the payload bay and the resulting boil-off of water and other volatiles. Since the heating and cooling of dust in this environment is on the time scale of seconds, the long decay on the night side and lag after sunrise could not be due to dust emission.

3. The day side was dominated by scattered sunlight out to 75 to 90 degrees from the sun.

4. These data exhibited a very pronounced left/right asymmetry across

the payload bay as the telescope scanned with the maximum being on the Shuttle port side. This is shown in detail in Figure 14.

5. These data did see each thruster firing as a bright feature. But unlike the 2 μm data, the electronic tail was only a few seconds long.

5.2.6 C-Band (8.5−14 μm) and D-Band (18−30 μm) Contamination Features

Since flux levels for these bands were obtained only during the two Vela attitudes listed in Table 10 during non-prime non-scanning observing intervals, there are no features that can be reported. The C-band appeared to be just into saturation by the end of Day 212. This is based on the signal beginning to "roll-over" as the level reaches saturation when the cold shutter is opened. The flux levels measured will be discussed below.

5.2.7 E-Band (77−115 μm) Contamination Features

In the E-Band there were three detectors. However, one of them, E1, gave inconsistent results on Day 212, and, subsequent to that, essentially failed even though E1 showed a change in response when the cold shutter was cycled. The outputs from E2 and E3 were very consistent on Day 212 and during the three inertial non-prime intervals given in Table 10. Although the signal in this band did not saturate during the other prime observing periods listed in Table 7 and the instrument was able to map the sky, it is now believed that the very high levels seen in E2 on Days 213, 214, and 215 and in E3 on Days 213 and 214 were due to the piece of warm mylar getting into the beam. In addition, there now is evidence to indicate that even the lowest levels seen, which were still about 100 times above the zodiacal level, may have been due to radiation from the 40−50K forebaffle in the telescope scattering off of the mirror. A synoptic summary of the E2 and E3 data is given in Figure 13. The general features seen in this band are as follows:

1. This band showed a very small day/night effect.

2. There was no substantial variation in the background outside of the present uncertainties.

3. There was no "solar glare" seen in this band even at the closest angle

scanned to the sun of 45 degrees.

4. Like the 4.5−9.5 μm data, the 100 μm data also show a pronounced asymmetry in the data as a function of scan angle (refer to Figure 14). Like the A-band, the peak is to the port side of the Shuttle. However, unlike the A-band, the minimum is not on the starboard side but rather in between. In addition, there appears to be repeatable but somewhat varying spatial structure with two minimums and two maximums in each full scan.

5.2.8 Measured Flux Levels

The absolute flux levels in each of the bands are given in Table 11 for each of the inertial attitudes listed in Table 10 as well as for two times on Day 212. The times chosen for Day 212 are just after sunrise and are when the A- and B-band fluxes were at a minimum for the rev and the S-band flux was not yet complicated by the "solar glare." Table 11 lists the in-band flux for each detector at the time specified as well as the in-band flux from the zodiacal light at the ecliptic pole and the equivalent water column density for the residual above the zodiacal for the appropriate solar elongation angle. Assuming a zodiacal spectrum the equivalent differential fluxes for each of these times is plotted in Figure 27.

The E-band data are not included since these levels are about 100 times the zodiacal background level, and are most likely due to scattered radiation from the warm forebaffle described below. The calibration on the S-, A-, and B-bands are believed to be very good based on many known calibration star sightings. The derived calibrations are given in Table 12. However, the C- and D-band calibrations are somewhat uncertain, since no in-flight calibrators were seen during the unsaturated inertial non-scanning intervals. The pre-flight laboratory calibrations were used for C- and D-bands and are assumed to be good to within 50% uncertainty. During the Vela 1 and Vela 2 attitudes the flux measured in the C- and D-bands was at or very near the zodiacal light level for this solar elongation.

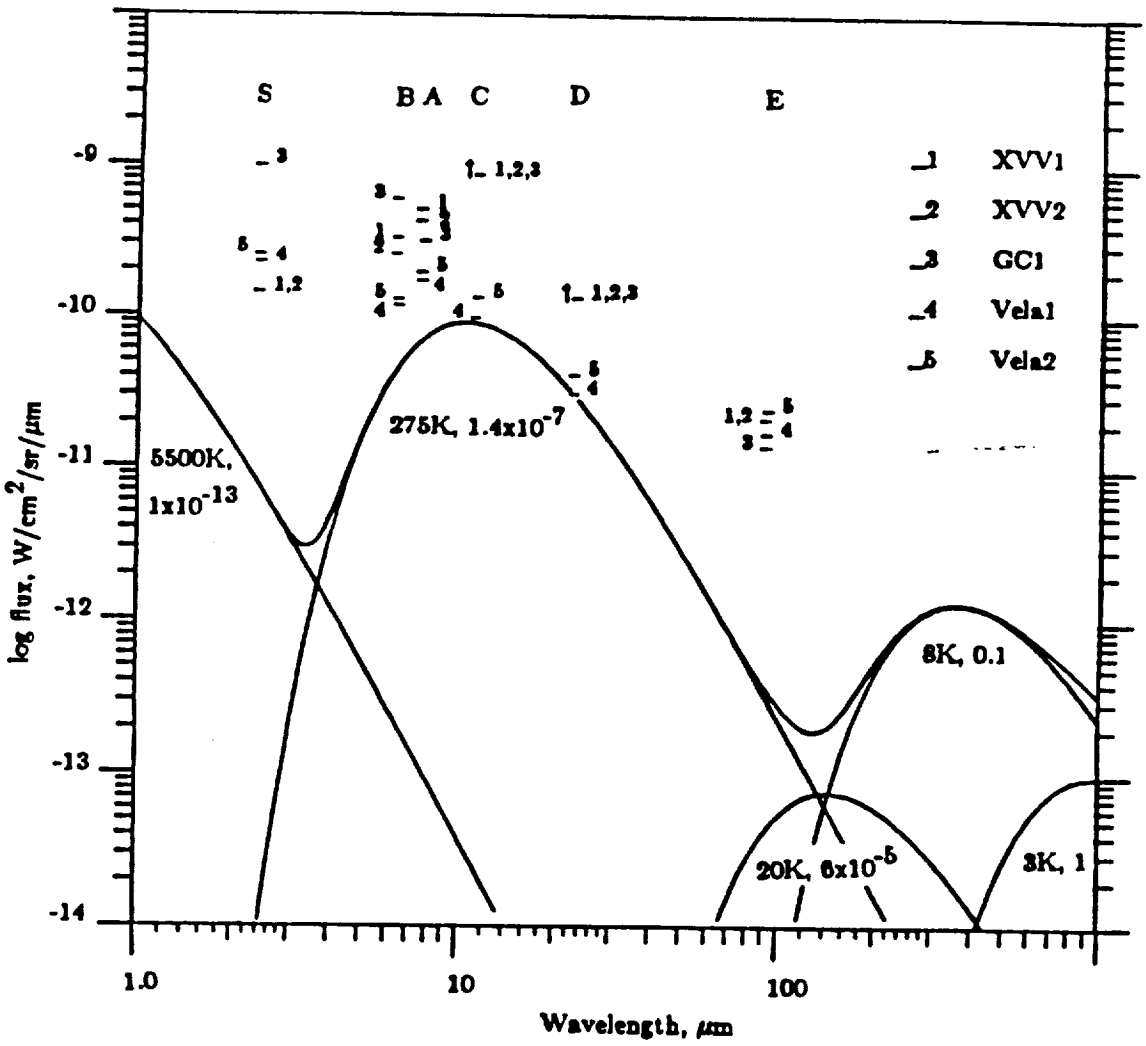

Figure 27. Measured background levels corresponding to the observing times and fluxes given in Table 11 For each band, S, B, A, C, D, and E, the flux level is shown for each of the observations designated on the right by 1 to 5. The zodiacal spectrum has been multiplied by a factor of two above the level expected for the ecliptic pole, approximating the level to be expected for the solar elongation in the Vela attitude (see Table 10).

Table 11. Measured In-Band Flux Levels

Detector	S	A	B	C	D2	Units
Bandwidth	2.0–3.0	4.5–9.5	6.1–7.1	8.5–14.5	18–30	μm
λ_{eff}	2.4	7.7	6.6	11.4	23	μm
zodiacal, pole	.037	1.28	0.24	2.6	1.75	10^{-10}W/cm^2/sr
XVV2 212/20:49	1.36	26.	3.13	>49	>14.5	10^{-10}W/cm^2/sr
mult. of zod.	37	20.	13.0	>19.3	>8.3	
H_2O (1)	4.3	22.	4.2	>420	>5.7	10^{13} mol/cm^2
CO_2 (1)				>12.8		10^{13} mol/cm^2
XVV1 212/22:19	1.36	23.	2.7	>49	>14.5	10^{-10} W/cm^2/sr
mult. of zod.	37	17.6	11.3	>19.3	>8.3	
H_2 O (1)	4.3	18.2	3.5	>420	>5.7	10^{13} mol/cm^2
CO_2 (1)				>12.8		10^{13} mol/cm^2
GC1 213/07:06	9.1	15.1	6.1	>49	>14.5	10^{-10} W/cm^2/sr
mult. of zod.	250	11.8	26.	>19.3	>8.3	
H_2O (2)	29	12.5	9.5	>450	>6.7	10^{13} mol/cm^2
CO_2 (2)				>13.8		10^{13} mol/cm^2
Vela 1 213/13:49	2.36	8.25	1.19	5.6	3.8	10^{-10} W/cm^2/sr
mult. of zod.	64	6.4	5.0	2.2	2.2	
H_2O (3)	7.5	5.1	1.09	0.0*	0.0*	10^{13} mol/cm^2
CO_2 (3)				0.0*		10^{13} mol/cm^2
Vela 2 214/14:01	2.6	9.6	1.31	6.9	5.2	10^{-10} W/cm^2/sr
mult. of zod.	71	7.5	5.4	2.7	2.9	
H_2O (3)	8.4	6.4	1.29	12.4	0.73	10^{13} mol/cm^2
CO_2 (3)				3.9		10^{13} mol/cm^2

1) A factor of 2.5 times the zodiacal flux from the pole was used for this elongation.
2) A factor of 1.5 times the zodiacal flux from the pole was used for this elongation.
3) A factor of 2.2 times the zodiacal flux from the pole was used for this elongation.
* The fluxes for the C- and D-bands are not as precise since no in-flight calibrator was available and the responsivities are based on lab measurements.

The in-band zodiacal flux is based on the following model:

For the scattered sunlight; 5500 K with dilution of 5×10^{-14}

For the emitted radiation; 275 K with a dilution of 7.1×10^{-7}

Table 12. Flux Calibrations

Detector μm	Bandpass sr	Beam $W/cm^2/count$	Conversion Factor	Gain
S	2–3	8.5×10^{-5}	3.5×10^{-16}	Hi
A	4.5–9.5	1.5×10^{-4}	1.65×10^{-16}	Mid
B	6.0–7.0	1.5×10^{-4}	1.48×10^{-16}	Mid
C	8.5–14.	1.5×10^{-4}	$1.81\times10^{-16\dagger}$	Lo
D	18.–30.	1.5×10^{-4}	$5.31\times10^{-16\dagger}$	Lo
E3	77.–115.	1.5×10^{-4}	0.85×10^{-16}	Mid

† From laboratory, not on-orbit, calibration.

5.2.9 Water Column Density

From Table 11 the lowest flux levels measured were during the Vela 1 and Vela 2 observing times. At these times the indicated level for water from the B-band is on the order of 100 times the specified goal of 10^{11} mol/cm^2. The levels in the C- and D-bands are consistent with this considering the uncertainty in the absolute calibration of these two bands. In addition, considering the uncertainties in the D-band, the flux level during both XVV1 and XVV2 is not inconsistent with the B-band water column density.

5.2.10 Other Species

Taking the indicated column density of water from the B-band as an upper limit for the flux in the other bands, it is quite clear and reasonable to conclude that some other independent mechanism is responsible for the high flux levels in the S-, A-, and C-bands. CO_2 contributes substantially to the background level only in the C-band. The indicated column densities for CO_2 in XVV1, XVV2, and GC1 are high and well above the specified goal. (Water contributes very little to the C-band.) The origin of the high levels in the S- and A-bands above that which can be attributed to water is perplexing. OH emission will contribute to both S and A without contributing to the longer wavelength bands. Even assuming this to be the case, the excess in the A-band must be from another source. No single blackbody curve can explain the various flux levels.

5.2.11 Dust Particles

Dust particles were seen throughout the mission at a much higher rate than the Shuttle goals stated above. On detailed analysis of just 10 minutes of data, 43 broad events were seen which are not characteristic of astronomical sources. A typical sighting is shown in Figure 28. The modulation of the amplitude is probably due to the particle rotation. Using only just this ten-minute interval, a sighting rate of one per minute is obtained. Even with a detector field of view being five times the solid angle defined above in the goal, the rate is still much higher than the goal. Of the 43 events identified, nine events seen in the A-, B-, and E-bands were studied in detail to obtain color temperatures and sizes. The ratio of the short to long wavelength flux is used to derive the color temperature. Assuming the particle covers the entire field of view and using an emissivity of 0.5 at both wavelengths, a lower limit to the particle size can be calculated. The results for the nine sightings for which adequate data are available are given in Table 13.

5.2.12 Spacecraft Glow Measurement

The glow phenomenon is the result of as-yet unknown processes that occur when an object, moving in low earth orbit, interacts with the ambient atmosphere. This causes the excitation of atoms and/or molecules with the subsequent release of photons. Because this induced glow is a form of UV, optical, and IR "light pollution" that could impact future observations in space, measurements of the glow have assumed a great importance in recent years (Mende and Swenson 1985 and references therein). Studies conducted during previous Shuttle missions have demonstrated that the intensity of the glow increases between 4000 and $\sim$ 7500 Å, with some evidence for a decrease between 7500 and 8000 Å. The need for data at wavelengths longer than 8000 Å prompted the addition of a study of the glow to the scientific objectives.

Beyond determining whether or not the glow intensity continues to increase into the IR, a quantitative measurement of the 2 μm flux can be quite useful in distinguishing between a number of glow models. The experiment to measure the IR glow was performed with the IRT viewing a volume adjacent to the one-meter-diameter flat base of the Plasma Diagnostic Package (PDP). The RMS was used to move the PDP base from a distance of 140 cm from the 15-cm telescope beam to within 12 cm of the beam in order to measure any modulation of the signal. The base of the PDP was exposed to both the ram direction and the anti-ram

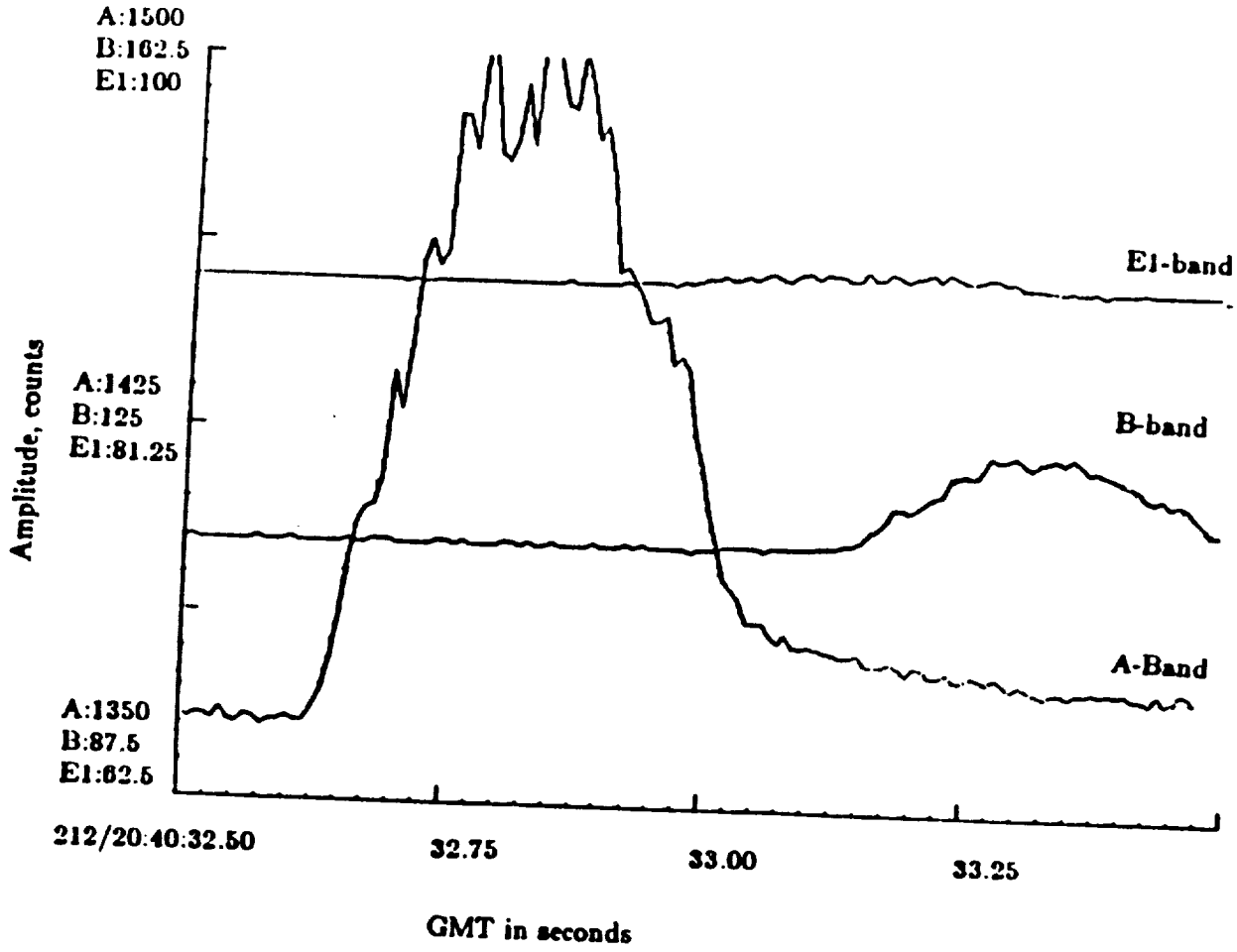

Figure 28. Dust particle sighting (096Aa/268 in Table 13). As the telescope scanned at 6°/s, the particle is first seen in the A-band, then the D-band (which was saturated at this time), then the E-band, and finally in the B-band. One full second of data is plotted. The amplitude modulation is due to particle rotation.

Table 13. Results from Nine Particle Sightings

Identifier	Temp, K	Size, μm
096Aa/84	175	515
096Aa/115	180	150
096Aa/268	210	225
096Aa/273	195	140
117Ab/5/6	175	410
117Ab/22	180	150
117Ab/41	200	140
117Ab/43	170	430
117Ab/79	185	200

direction. A comparison of the measured IR flux from the two orientations was made. In both cases the glow experiment was conducted on the night side of the orbit with the Shuttle pointed inertially and the IRT not scanning.

Problems due to thruster firings and subsequent baseline variations have made the measurements difficult to analyze. However, a definite 3σ upper limit to the 2 μm flux can be set at $< 1.5 \times 10^{-4}$ Rayleighs/Å. The results of this experiment are consistent with a sharp decrease in the glow spectrum at wavelengths between 8000 Å and 3.0 μm. This is to be compared to a glow intensity from the Shuttle tail of more than 500 Rayleighs/Å at 7500 Å measured on a previous flight (Mende *et al.* 1984). The dropoff in the glow intensity between 8000 Å and 2 μm of the magnitude observed is at variance with almost all current models of the glow, and it is anticipated that this measurement will set stringent limits on future glow models.

5.2.13 Thruster Firings

Thruster firings were observed in all the detector bands. As described above there is an electronic tail in the S-band signal that had an e-folding time constant on the order of 20 seconds. Since the detectors have 1-millisecond time resolution, the temporal history of the firing, rise time, duration, and fall time are all clearly resolved. In the XVV attitude, periods of 5−10 minutes without a firing were quite common. The effects of the thruster firings needed to be removed from the IR data before maps of the celestial sphere could be generated. Only the vernier thrusters were used during observing. These had a thrust of 24 pounds and their location and vector are given in Table 3.

5.2.14 Conclusions about the Environment

Based on the measurements of the IRT, the column density of water was at best more than 100 times above the level where its effects in the IR exceed the limiting sky background. In addition, at least three other species were necessary to account for the variations in the flux levels measured in the five spectral bands. One of these may be CO_2. The particulate sighting rate was substantially greater than the goals set for the Shuttle. For the 10-minute interval studied in detail, the sighting rate was 20 times the upper limit desired. Scattered sunlight of local origin in the shorter wavelength bands was seen out to 75 degrees from the sun. There was no observable IR glow at these altitudes which puts severe upper limits on models for the emission mechanism. All in all the environment is very poor for background-limited IR photometry. However, the induced background levels were probably acceptable for narrow-band spectrometry and observing where the background would otherwise be high, such as earth view.

5.3 Measurement of Superfluid Helium Properties

Although the primary functions of the superfluid helium storage and vent system were to cool the IR detectors, telescope mirror, and baffles, a process which worked very well during the mission, it was also planned to perform unique controlled measurements of the behavior of the fluid system in zero-G. These tests were scheduled for the final day of the mission after all astronomical observations were complete. About 35 hours of controlled tests of the superfluid storage and flow control components were conducted. These tests could not be simulated in the laboratory.

The measurements of interest were the functioning of the porous plug phase separator and its relationship to the superfluid bath. Porous plugs employ the thermomechanical or fountain effect, a quantum mechanical phenomenon existing only with superfluid helium, to hold liquid helium within a dewar and permit only vapor to vent. The characteristics which were to be determined were:

1. Whether liquid would flow uncontrollably from the dewar if venting was temporarily stopped or when venting was restarted;

2. Whether the helium bath could be warmed until it passed from the superfluid phase into the normal phase, and then be recooled to superfluidity in a controlled manner when venting was restarted; and

3. Whether heat deliberately applied to the vent side of the porous plug could reverse the fountain effect and draw more helium through the plug.

The IRT vent valves were closed a number of times for various periods; no fluid flow through the plug was detected and venting resumed smoothly when the valves were reopened. On three occasions the superfluid bath was allowed to warm above the λ-point into the normal phase (temperature >2.17K); each time when the vent valves were reopened the bath recooled in a controlled manner. Operation of a small heater on the vent side of the porous plug did not enhance fluid flow through the plug, but instead forced the liquid helium back through the plug and reduced the flow. This latter result is contrary to the laboratory experience of researchers developing fountain effect pumps for the transfer of liquid helium in space, and must be further studied. A more detailed description of the helium system performance is given by Urban and Ladner (1986).

5.4 Cryogenically Cooled Telescope Design

A high background level in the E-band was seen throughout the mission. One of the possibilities considered was detection of radiation from the forebaffle. The lower half of the telescope tube and mirror were cooled to 8K, but the forebaffle temperature was within the range of 40K to 60K during the various observing intervals. The in-band flux for a blackbody at each of the forebaffle temperatures was computed for the E-band ($77-115$ μm). This was compared with the measured power onto the detector under the best background conditions (typically near sunrise on each orbit). A linear correspondence of the measured to

the computed power based on the forebaffle temperature was found. Figure 29 is a plot of the in-flight measured power for the various forebaffle temperatures. The Space Infrared Telescope Facility (SIRTF) modeling algorithms for scattered and diffracted radiation were then applied to the IRT detector and telescope design (Dinger 1986). The parameter defining the amount of contamination on the mirror was varied and these curves are also plotted in Figure 29. It was found that the high background could be accounted for by scattering of the forebaffle radiation off the primary mirror into the detectors for a mirror areal coverage of 3.2%. As a comparison of cleanliness, the Hubble Space Telescope (HST) mirror prior to recoating had a measured areal coverage of 2.1% (Facey 1984). Immediately after cleaning the areal coverage on the HST mirror was measured to be 0.7% and estimates for two years after cleaning are at about 2.0 to 2.5%. Although the IRT mirror was not quite as clean as that of the HST, it is probably unreasonable to expect future telescopes to be significantly cleaner. Thus, in the design of cryogenically cooled telescopes, special attention needs to be given to all elements which are not cooled below the mirror temperature to ensure that they will not contribute to the background.

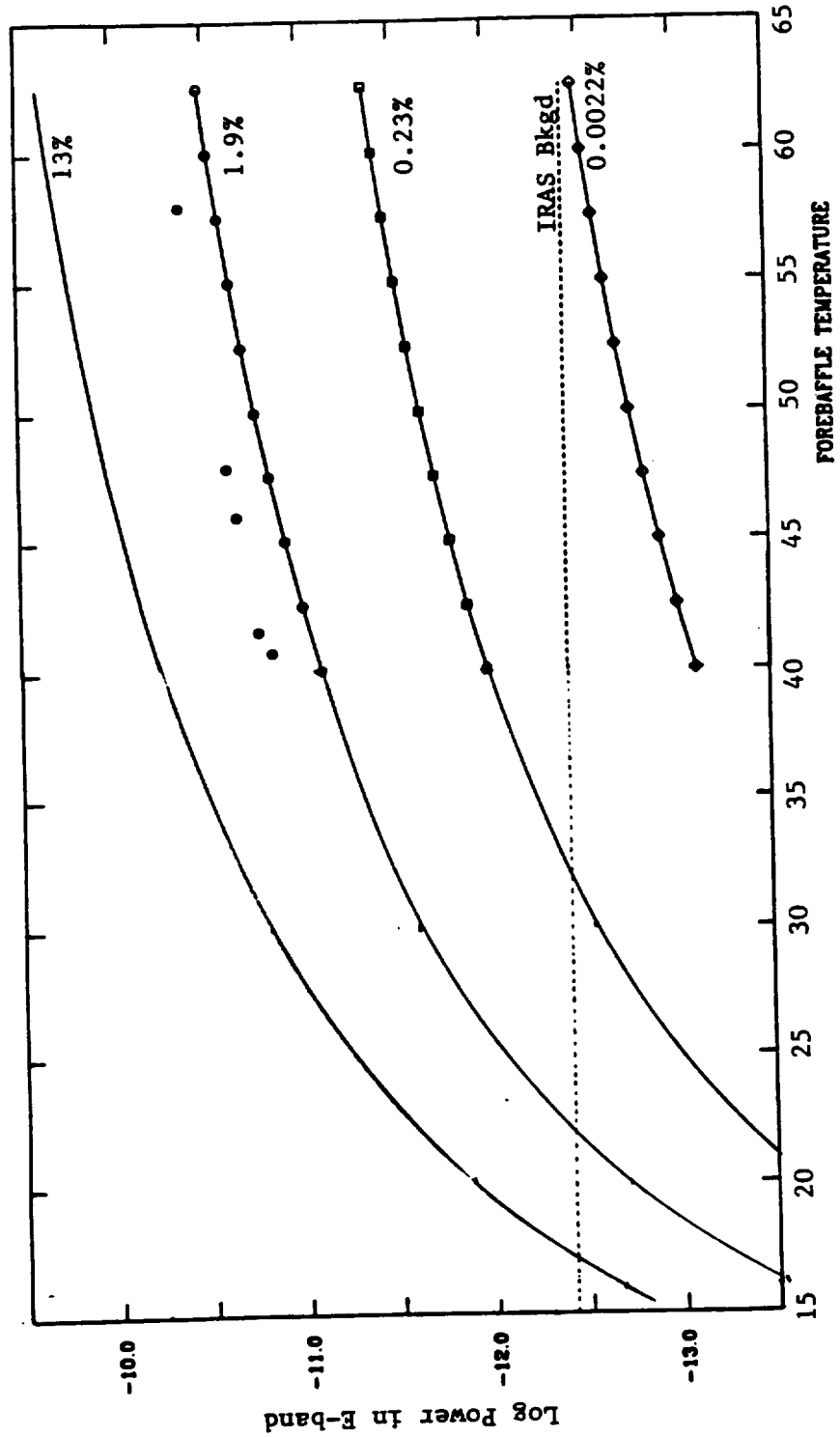

Figure 29. Measured background in E-band and modelled background. The different curves are for the different percent areal coverage indicated. The IRT background measurements are shown by the solid dots. $\Delta\lambda$ = 77−115 μm.

6. REFERENCES

Bahcall, J. N. 1984, Astrophys. J. **276**, 169.

Becklin, E. E. and Neugebauer, G. 1968, Astrophys. J. **151**, 145.

Bohlin, R. C., Savage, B. D., and Drake, J. F. 1978, Astrophys. J. **224**, 132.

Boyce, B. M. 1977, Proc. SPIE **107**, 72.

Campbell, M. F., Hoffmann, W. F., Thronson, Jr., H. A., and Harvey, P. M. 1980, Astrophys. J. **238**, 122.

Catchpole, R. M., Glass, I. S., and Whitelock, P. 1989, in *IAU Symposium 136, The Center of the Galaxy*, ed. M. Morris (Dordrecht: Kluwer Academic Publishers), p. 75.

Cox, P. and Mezger, P. G. 1989, Astron. & Astrophys. Rev. **1**, 49.

Dame, T. M., Ungerechts, H., Cohen, R. S., de Geus, E. J., Grenier, I. A., May, J., Murphy, D. C., Nyman, L.-Å., and Thaddeus, P. 1987, Astrophys. J. **322**, 706.

Dinger, A. 1986, *Straylight Performance of the Spacelab-2 Infrared Telescope at E-Band*, NASA Tech. Note TN-86-7104-941-17, Rev. 1.

Drapatz, S. 1981, in *IAU Symposium 96, Infrared Astronomy*, ed. C. G. Wynn-Williams and D. P. Cruikshank (Dordrecht: D. Reidel), p. 261.

Facey, T. 1984, *Space Telescope Primary Mirror Surface Particulate Contamination after Cleaning*, Optical Telescope Assembly Project Report PR-952, Perkin-Elmer.

Fazio, G. G., Dame, T. M., and Kent, S. 1989, in *IAU Symposium 139, Galactic and Extragalactic Background Radiation*, to be published.

Frogel, J. A. 1988, Ann. Rev. Astr. Ap. **26**, 51.

Gatley, I., Joyce, R., Fowler, A., DePoy, D., and Probst, R. 1989, in *IAU Symposium 136, The Center of the Galaxy*, ed. M. Morris (Dordrecht: Kluwer

Academic Publishers), p. 361.

Giard, M., Pajot, F., Lamarre, J. M., Serra, G., Caux, E., Gispert, R., Léger, A., and Rouan, D. 1988, Astron. & Astrophys. **201**, L1.

Glass, I. S., Catchpole, R. M., and Whitelock, P. A. 1987, M.N.R.A.S. **227**, 373.

Güsten, R. and Mezger, P. G. 1982, Vistas Astron. **26**, 159.

Habing, H. J. 1988, Astron. & Astrophys. **200**, 40.

Harris, A. W., Lemke, D., and Hoffmann, W. 1980, Astrophys. Space Science **72**, 111.

Hayakawa, S., Matsumoto, T., Murakami, H., Uyama, K., Thomas, J. A., and Yamagami, T. 1981, Astron. & Astrophys. **100**, 116.

Hiromoto, N., Maihara, T., Mizutani, K., Takami, H., Shibai, H., and Okuda, H. 1984, Astron. & Astrophys. **139**, 309.

Hoffmann, W., Lemke, D., and Frey, A. 1978, Astron. & Astrophys. **70**, 427.

Jones, T. J., Ashley, M., Hyland, A. R., and Ruelas-Mayorga, A. 1981, M.N.R.A.S. **197**, 413.

Kawara, K., Kozasa, T., Sato, S., Kobayashi, Y., and Okuda, H. 1982, Publ. Astron. Soc. Japan **34**, 389.

Koch, D. G., Melnick, G. J., Fazio, G. G., Rieke, G. H., Low, F. J., Hoffmann, W., Young, E. T., Urban, E. W., Simpson, J. P., Witteborn, F. C., Gautier, III, T. N., and Poteet, W. 1988, Astrophys. Lett. and Comm. **27**, 211.

Lange, S. R., Breault, R. P., and Greynolds, A. W. 1977, Proc. SPIE **107**, 89.

Lebofsky, M. 1979, Astron. J. **84**, 324.

Lebofsky, M. J. and Rieke, G. H. 1987, in *American Institute of Physics Proc. 155, The Galactic Center*, ed. D. C. Baker (New York: AIP), p. 79.

Léger, A. and Puget, J. L. 1984, Astron. & Astrophys. **137**, L5.

Lemke, D. 1981, Proc. SPIE **265**, 366.

Little, S. J. and Price, S. D. 1985, Astron. J. **90**, 1,812.

Low, F. J. 1979, Proc. SPIE **183**, 11.

Matsumoto, T., Hayakawa, S., Koizumi, H., Murakami, H., Uyama, K., Yamagami, T., and Thomas, J. A. 1982, in *American Institute of Physics Proc. 83, The Galactic Center*, ed. G. R. Riegler and R. D. Blandford (New York: AIP), p. 48.

Melnick, G. J., Fazio, G. G., Koch, D. G., Rieke, G. H., Young, E. T., Low, F. J., Hoffmann, W. F., and Gautier, T. N. 1987, in *American Institute of Physics Proc. 155, The Galactic Center*, ed. D. C. Baker (New York: AIP), p. 157.

Mende, S. B. and Swenson, G. R. 1985, Second Workshop on Spacecraft Glow, J. H. Waite, Jr., and T. W. Moorehead, eds., NASA Conf. Publ. 2391, 1.

Mende, S. B., Banks, P. M. and Klingelsmith, D. A., III 1984, Geophys. Res. Lett. **11**, 527.

Neugebauer, G. *et al.* 1984, Astrophys. J. Lett. **278**, L1.

Noguchi, K., Hayakawa, S., and Matsumoto, T. 1981, Publ. Astron. Soc. Japan **33**, 583.

Oda, N., Maihara, T., Sugiyama, T., Okuda, H. 1979, Astron. & Astrophys. **72**, 309.

Oda, N. 1985, Astron. & Astrophys. **145**, 45.

Okuda, H. 1981, in *IAU Symposium 96, Infrared Astronomy*, ed. C. G. Wynn-Williams and D. P. Cruikshank (Dordrecht: D. Reidel), p. 247.

Okuda, H. 1983, preprint.

Okuda, H. 1985, in *IAU Symposium 106, The Milky Way Galaxy*, ed. H. van Woerden, R. J. Allen, and W. B. Burton (Dordrecht: D. Reidel), p. 123.

Price, S. D., Marcotte, L. P., and Murdock, T. L. 1982, Astron. J. **87**, 131.

Price, S. D. and Marcotte, L. P. 1980, AFGL Technical Report, AFGL-TR-80-0182 (AD-A0100-289).

Puget, J. L., Léger, A., and Boulanger, F. 1985, Astron. & Astrophys. **142**, L19.

Rantanen, R. O. and Strange Jensen, D.A. 1977, *Orbiter/Payload Contamination Control Assessment Support*, Martin Marietta Aerospace, MCR-77-107.

Rieke, G. H. 1989, in *IAU Symposium 136, The Center of the Galaxy*, ed. M. Morris (Dordrecht: Kluwer Academic Publishers), p. 21.

Simpson, J. P. and Witteborn, F. C. 1977, Applied Optics **16**, 2,051.

Simpson, J. P. and Witteborn, F. C. 1978, Proc. USAF-NASA International Spacecraft Contamination Conference, 7 March, Colorado Springs, AFML-TR-78-190, NASA-CP-2039, J. M. Jemiola, ed.

Strong, A. W., Bloemen, J. B. G. M., Dame, T. M., Grenier, I. A., Hermsen, W., Lebrun, F., Nyman, L.-Å., Pollock, A. M. T., and Thaddeus, P. 1988, Astron. & Astrophys. **207**, 1.

Urban, E. and Ladner, D. 1986, Proc. of the XI International Cryogenic Engineering Conference, Butterworth Publ. Ltd., London, 341.

Urban, E. W., Katz, L., Hendricks, J. B., and Karr, G. R. 1979, Proc. SPIE **183**, 40.

Urban, E. W., Katz, L., and Karr, G. R. 1975, Proc. 14th International Conference on Low Temperature Physics **4**, 37.

van de Hulst, H. C. 1957, *Light Scattering by Small Particles* (New York: Wiley, Chapman, and Hall).

van der Kruit, P. C. and Searle, L. 1981, Astron. & Astrophys. **95**, 105.

van der Kruit, P. C. 1986, Astron. & Astrophys. **157**, 230.

Young, E. T., Rieke, G. H., Gautier, T. N., Hoffmann, W. F., Low, F. J., Poteet, W., Fazio, G. G., Koch, D., Traub, W. A., Urban, E. W., and Katz, L. 1981, Proc. SPIE **280**, 12.

JSC 07700 – Level II Program Definition and Requirements for Space Shuttle System: Payload Accommodations

7. ACRONYMS

AM50	Aries Mean 1950 Coordinate System
APART	Arizona Paraxial Analysis of Radiation Transfer
BOAA	Bright Object Avoidance Algorithm
DGSE	Digital Ground Support Equipment
ECAS	Experiment Computer Applications Software
ECOS	Experiment Computer Operating System
EPDS	Electrical Power Distribution Subsystem
FES	Flash Evaporator System
FWHM	Full Width at Half Maximum
GMT	Greenwich Mean Time
GSFC	NASA Goddard Space Flight Center
GUERAP II	General Unwanted Energy Rejection Analysis Program
HITS/ECEP	HRM I/O Test System / Experiment Checkout Equipment Processor
HRM	High Rate Multiplexer
HST	Hubble Space Telescope
IPS	Instrument Pointing System
IR	Infrared
IRAS	Infrared Astronomy Satellite
IRT	Infrared Telescope on Spacelab-2
JFET	Junction Field Effect Transistor
JSC	NASA Johnson Space Center
KSC	NASA Kennedy Space Center
LOS	Loss of Signal
MET	Mission Elapsed Time
MSFC	NASA Marshall Space Flight Center
NEFD	Noise Equivalent Flux Density
NEP	Noise Equivalent Power
OANC	Orbiter Ancillary Channel (Data Tape)
OMS	Orbiter Maneuvering Subsystem
O&C	Operations and Checkout Building at KSC
PDP	Plasma Diagnostics Package on Spacelab-2
PMI	Permanently Missing Interval
POCC	Payload Operations Control Center
PST	Point Source Transmittance
QSO	Quasi-Stellar Object
RAU	Remote Acquisition Unit
RMS	Remote Manipulator system
SAA	South Atlantic Anomaly

SANC	Spacelab Ancillary Channel (Data Tape)
SAO	Smithsonian Astrophysical Observatory
SECT	Spacelab Experiment Channel Tape
SIRTF	Space Infrared Telescope Facility
SL-2	Spacelab-2
SR	Orbital Sunrise
SS	Orbital Sunset
UA	University of Arizona
UV	Ultraviolet
VCAP	Vehicle Charging and Potential Experiment on Spacelab-2
VRCS	Vernier Reaction Control System
XRT	X-Ray Telescope on Spacelab-2

APPENDIX A

IRT DOCUMENTS, PUBLICATIONS, AND PRESENTATIONS

Small Helium-Cooled Infrared Telescope

IRT DOCUMENTS, PUBLICATIONS AND PRESENTATIONS

15 February 1990

University of Arizona
Steward Observatory

Marshall Space Flight Center
Space Sciences Laboratory

Smithsonian Institution
Astrophysical Observatory
60 Garden Street
Cambridge, Massachusetts 02138

CONTENTS

A.1 IRT 100-199 Specifications and Requirements

IRT-101 "Cryostat Mechanical Design Parameters"
W. Traub — 16 December 1977

IRT-102 "Cryostat Scan Drive Requirements"
Committee — 13 December 1977
Rev. A 15 August 1978
Rev. B 8 September 1978
Rev. C 21 May 1980

IRT-103 "Summary of Detector Performance Predictions and Required Digitization"*
G. Rieke — August 1978
Rev. A

IRT-104 "Design and Performance Specification"
D. Harrison — January 1978
Rev. B March 1978

IRT-105 "High Rate Multiplexer Usage Requirements"
D. Harrison — 22 February 1978

IRT-106 "Design Considerations for Dewar Size"
E. Urban — 13 February 1978

IRT-107 "Ground Operations Requirements"
E. Urban — 9 March 1978

IRT-108 "EGSE Functional Requirements"
D. Koch — 9 June 1978
Rev. A 15 September 1978

IRT-109 "Command and Housekeeping Definition"
K. Fredholm — 21 November 1978
Rev. A 5 December 1978
Rev. B 25 September 1979
Rev. C 30 April 1980
Rev. D 20 September 1980 D. Koch
Rev. E 19 October 1981 D. Koch
Rev. F 20 September 1982 D. Koch

*IRT-103, originally "Technical Communications on Detectors and Electronics" by F. Low, was cancelled and the number reassigned.

IRT-110	"Subsystem Definition EL-1" S. Crosbie	13 October 1978	
IRT-111	"DGSE System Manual" J. Gettys D. Koch	9 January 1985 Rev. A	
IRT-112	"Connector Pin Lists: EL-2" K. Fredholm	30 July 1980 Rev. A 30 March 1981 Rev. B 7 May 1982 Rev. C 10 February 1983	 L. Coyle L. Coyle L. Coyle D. Koch
IRT-113	"Connector Pin Lists: EL-3" K. Fredholm	2 July 1980 Rev. A 30 March 1981 Rev. B 7 May 1982 Rev. C 10 February 1983	 L. Coyle L. Coyle L. Coyle D. Koch
IRT-114	"EL-2 -- Power Dissipation by Device" K. Fredholm	28 August 1979	
IRT-115	"EL-3 -- Power Dissipation by Device" K. Fredholm	28 August 1979	
IRT-116	"HRM Format Description" K. Fredholm	2 October 1979 Rev. A 15 October 1981 Rev. B 26 February 1982	 D. Koch D. Koch
IRT-117	"Preinstallation Test Requirements" R. Watts	(Draft) 30 November 1979	
IRT-118	"Connector Pin Lists: CGSE" K. Fredholm	20 August 1980 Rev. A 24 July 1981	 D. Bruno
IRT-119	"A DEP for the IRT System" R. Watts	18 May 1981	
IRT-120	[reserved for "POCC Requirements" (DRF's and related commentary)] R. Watts		
IRT-121	"IRT Verification Matrix" R. Watts	8 October 1980	

IRT-122	"Electrical Test Requirements for the Whittaker Valve-Motor Actuator" J. Montenegro	23 October 1980
IRT-123	[Reserved for "Heaters and Thermostats (Definitions)"] Katz/Urban	
IRT-124	[Reserved for "Cover Motors"] Katz/Urban	
IRT-125	"IRT Nomenclature" L. Katz	5 November 1980
IRT-126	"Electronics Materials List" SCI Systems, Inc.	18 March 1981
IRT-127	"IRT Connectors"	30 March 1981 Rev. A 21 April 1981 Rev. B 23 June 1981
IRT-128	"Quality Assurance, Verification, and Documentation Requirements" R. Watts	Draft 1 July 1981 Issued 10 March 1983
IRT-129 to IRT-138	inclusive reserved for documents generated by MSFC E&C Lab.	
IRT-139	"Contamination Control Requirements" G. Nystrom	5 November 1981
IRT-140	"Whittaker Valve Test Requirements" D. Koch	22 February 1982
IRT-141	[Reserved for "Whittaker Vacuum Cover Test Requirements"]	
IRT-142	"IRT Standard Configurations" D. Koch	(Draft) 9 September 1982
IRT-143	"Final Buildup and Test of the IRT" R. Watts	21 December 1983
IRT-144	"POCC Command List" D. Koch	5 March 1984 Rev. A 2 July 1984
IRT-145	"POCC Display Definitions" D. Koch	17 May 1984

IRT-146 "Umbilical Control Box to LPS Definitions"
J. Montenegro 24 May 1984

A.2 IRT 200-299 Plans and Policies

IRT-201	"Data System Description and Power Estimates"	
	D. Harrison	13 December 1977
		Rev. A 17 March 1978
IRT-202	"Preliminary Mission Plan for SL-2"	
	Committee	14 December 1977
		Rev. A 20 March 1978
IRT-203	"The Data Reduction Plan for the SL-2 Infrared Telescope"	
	D. Koch	27 January 1978
		Rev. A 9 March 1978
IRT-204	"EGSE Configuration and Capabilities"	
	T. Stephenson	19 March 1978
IRT-205	"Estimate of Processing Requirements"	
	D. Koch	23 March 1978
		Rev. A 11 April 1979
		Rev. B 14 November 1979
		Rev. C 29 July 1981
IRT-206	"Experiment Program Plan"	
	R. Watts	31 May 1978
IRT-207	"Groundrules for Handling IRT Flight Electronics"	
	R. Watts	11 February 1980*
IRT-208	"IRT Testing Policy"	
	R.N. Watts	20 December 1979
IRT-209	"Organization for IRT Ground Processing at KSC"	
	R.N. Watts	22 May 1979
		Rev. A 30 June 1982
IRT-210	"Scientific Goals of IRT Data Analysis"	
	G.G. Fazio	13 August 1979
	D. Koch	Rev. A 8 November 1979
	W. Hoffmann	
	G. Rieke	
IRT-211	"IRT Rules for Handling Flight Hardware"	

*IRT-207, originally "UA Experiment Program Plan," was cancelled and the number reassigned.

R.N. Watts 25 June 1980

IRT-212 "Acquisition Plan for a VAX 11/750 Computer for the Small Helium-Cooled Infrared Telescope Program"
R.N. Watts January 1981

IRT-213 "Procedures for IRT Operation"
D. Koch (Draft) August 1981

IRT-214 "Mission Operations Flow Chart"
D. Koch 30 October 1981
Rev. A 7 September 1982

IRT-215 "IRT Verification Plan"
R. Watts (Draft) July 1982

IRT-216 "IRT Major Component Installation"
R. Hughes 24 September 1982

IRT-217 "Verification Instructions"
R. Watts (Draft) 20 June 1983

IRT-218 "Mission Planning Information and Baseline Mission Plan"
R. S. Taylor 2 May 1984

IRT-219 "Observing Maps and BOAA Output"
D. Koch 20 September 1984

IRT-220 "Inertial Attitude Sky Maps"
D. Koch (~1/85 - being written)

A.3 IRT 300-399 Procedures

ET43-IRT-300 "Final Test Report: Small Helium Cooled Infrared Telescope Systems Testing at MSFC"
MSFC June 1984
See "Testing" File

IRT-301 "Qualification Procedure for Stow Latch Assembly 42A20143"*
Test Laboratory, MSFC

ET43-IRT-301 "Test Report: IRT 1-Inch Diameter Flexible Vent Line Bellows Hose -- Life Cycle Tests"
MSFC 10 July 1984
See "Testing" File

IRT-302 "IRT Observing Schedule"
D. Koch 7 November 1979

IRT-303 "Acceptance Procedure for Vacuum Cover Assembly 42A20134"**
Test Laboratory, MSFC

IRT-304 "Interface Verification Procedure"
R.N. Watts, Jr. (Draft) 8 February 1980

IRT-305 "Health Check"
R.N. Watts, Jr. (Draft) 6 February 1980

IRT-306 "Handling Sling and Adapter, IRT, Operating Instructions" 18 March 1981

IRT-307 "Handling Sling, Cryostat Assembly, Operating Instructions" 18 March 1981

IRT-308 "Handling Sling, Dewar Assembly, Operating Instructions" 18 March 1981

IRT-309 "Handling Sling, Dewar/Transfer Assembly, Operating Instructions" 18 March 1981

---

*"Acceptance Test Procedure" by Watts and Poteet, originally IRT-301, has been renumbered IRT-318 (9/81).

**"Functional Test Plan" by R. Watts, originally IRT-303, has been renumbered IRT-319 (9/81).

IRT-310 "IRT Electronics Test Procedure"
L. Coyle 23 March 1981

IRT-311 "Installation Procedure
Strut Attachments to Structure Assembly and
Pallet Assembly"
Structures and Propulsion Laboratory, MSFC 15 July 1980

IRT-312 "Acceptance Test Procedure for the Arizona-Built
Telescope in the IRT Cryostat"
W. Poteet 9 April 1982
Rev. A 7 June 1982
Rev. B 23 June 1982

IRT-313 "Investigation of Vacuum Ratings and
Leak Rates on the Infrared Telescope
Dewar"
Space Sciences Laboratory, MSFC 1 July 1980

IRT-314 "Investigation of Vacuum Ratings and
Leak Rates on the Infrared Telescope
Dewar Subsystem"
Space Sciences Laboratory, MSFC 14 July 1981

IRT-315 "Procedure for Connecting and Disconnecting
the Infrared Telescope Cryogenic Servicing
Lines"
Space Sciences Laboratory, MSFC September 1981

IRT-316 "Procedure for Evaluation of the Thermal
Performance of the Infrared Telescope
Dewar Subsystem"
Space Sciences Laboratory, MSFC October 1981

IRT-317 "Scan Drive Actuator Assembly and Alignment
Procedure"
Electronics and Control Laboratory, MSFC

IRT-318 "Acceptance Test Procedure"
R.Watts (Draft) October 1979
W. Poteet

IRT-319 "Functional Test Plan"
R.N. Watts, Jr. (Draft) 8 February 1980

IRT-320 "EL-3 Verification Procedure"
D. Koch 26 April 1982

IRT-321 "Heater Control Electronics Bench Functional Test Procedure, Assembly No. 5061052-1"
[MSFC Procedure EC24-0501]
Part A
J. Montenegro 4/27/81

IRT-321 "Heater Control Electronics Thermal Test Procedure, Assembly No. 5061052-1"
[MSFC Procedure EC24-0501]
Part B
J. Montenegro 4/27/81

IRT-322 "Cover Motor Driver and Pyro Initiator Bench Functional Test Procedure, Assembly No. 5061074"
[MSFC Procedure EC24-0502]
Part A
B.R. Hollis, Jr. 4/27/81

IRT-322 "Cover Motor Driver and Pyro Initiator Thermal Test Procedure, Assembly No. 5061074"
[MSFC Procedure EC24-0502]
Part B
B.R. Hollis, Jr. 4/27/81

IRT-323 "Valve Driver Electronics Bench Functional Test Procedure, Assembly No. 5061050"
[MSFC Procedure EC24-0503]
Part A
J. Montenegro 5/11/81

IRT-323 "Valve Driver Electronics Thermal Test Procedure, Assembly No. 5061050"
[MSFC Procedure EC24-0503]
Part B
J. Montenegro 5/11/81

IRT-324 "Input Commands Bench Functional Test Procedure, Assembly No. 5061046-1"
[MSFC Procedure EC24-0505]
W.C. Sutherland 7/1/81

IRT-325 "Input Commands Bench Functional Test Procedure, Assembly No. 5061046-2"
[MSFC Procedure EC24-0506]
W.C. Sutherland 5/11/81

IRT-326 "Space Vent Controller Bench Functional Test Procedure, Assembly No. 5061044-1"
[MSFC Procedure EC24-0507]
W.C. Sutherland 6/23/81

IRT-327 "IRT Signal Conditioners (T-2,8,6-5) Bench Functional Test Procedure, Assembly No. 5061042-1"
[MSFC Procedure EC24-0508]
B.R. Hollis, Jr. 11/20/81

IRT-328 "Signal Conditioners (T1,5,6,7, + Bridge) Bench Functional Test Procedure, Assembly No. 5061040-1"
[MSFC Procedure EC24-0509]
B.R. Hollis, Jr. 11/20/81

IRT-329 "Signal Conditioners (T-3,4,12,13,15,16) Bench Functional Test Procedure, Assembly No. 5061038-1"
[MSFC Procedure EC24-0510]
B.R. Hollis, Jr. 11/20/81

IRT-330 "Signal Conditioners (T-17,18,19,20,21) Bench Functional Test Procedure, Assembly No. 506038-2"
[MSFC Procedure EC24-0511]
B.R. Hollis, Jr. 11/20/81

IRT-331 "Digital Controller and Housekeeping Signals Bench Functional Test Procedure, Assembly Nos. 5061054-1, 5061056-1, 5061058-1, 5061048-1"
[MSFC Procedure EC24-0512]
W.C. Sutherland 8/27/81

IRT-332 "Scan Drive Electronics Bench Functional Test Procedure, Assembly No. 5061060"
[MSFC Procedure EC24-0513]
Part A
J. Montenegro 4/29/81

IRT-332 "Scan Drive Electronics Thermal Test Procedure, Assembly No. 5061060"
[MSFC Procedure EC24-0513]
Part B
J. Montenegro 5/11/81

IRT-334 "IRT EL-1 Electronics Assembly Acceptance and Functional Test Procedure, Assembly No. 5061100-1" [MSFC Procedure EC24-0515]
B.R. Hollis, Jr. 31 March 1982
W.C. Sutherland
J. Montenegro

IRT-335 "Umbilical Mode Electronics Functional Test Procedure (IRT GSE Electronics), Assembly No. 42A22407" [MSFC Procedure EC24-0551]
J. Montenegro Rev. B 28 May 1982

IRT-336 "Umbilical Mode Electronics Functional Test Procedure (IRT GSE Electronics), Assembly No. 42A22409" [MSFC Procedure EC24-0552]
J. Montenegro 19 May 1982

IRT-337 "Absolute Position Encoder Bench Functional Test Procedure, Model No. 5V68OBG-2" [MSFC Procedure EC24-0553]
W.C. Sutherland 29 June 1982

IRT-338 "Dewar Fill Electronics Functional Test Procedure (IRT GSE Electronics), Assembly No. 42A22810" [MSFC Procedure EC24-0554]
J. Montenegro 25 June 1982

IRT-339 "GSE Umbilical Control Electronics Functional Test Procedure, Assembly No. 42A20464-1" [MSFC Procedure EC24-0555]
J. Montenegro 25 June 1982

IRT-340 "Dewar Fill Mode Functional Test Procedure (IRT GSE Electronics), Assembly No. 42A22800-1" [MSFC Procedure EC24-0556]
J. Montenegro 14 July 1982

IRT-347 "Performance Evaluation of the Arizona-Built Telescope in the IRT Cryostat"
W. Poteet (Draft) 13 April 1982

IRT-348 "Qualification Thermal/Vacuum Test of Valve Actuator Motor" [Whittaker Motor Test Procedure] [MSFC No. MTCP-C-IRT-306]
John H. Lowery 4 May 1982

IRT-355 MSFC-PROC-EB24-0569 "42A20464-1, Umbilical Control and Display Box (UCB) for the Infrared Telescope Operators

Instruction Manual"

29 March 1985 Rev-C

IRT-364 "Log Book EL-2"
R. Watts

IRT-365 "Log Book EL-3"
R. Watts

IRT-321 to IRT-346 inclusive reserved for PC card procedures generated by MSFC E&C Lab.

IRT-349 to IRT-363 inclusive reserved by E.C. Smith for procedures (10/7/82).

IRT-366 "Acceptance Test Procedure for Electronics Subsystems EL-2 and EL-3"
L. Coyle
30 December 1982
Rev. A 7 February 1983
Rev. B 1 March 1983

IRT-367 "Instructions for Use of the CGSE and Related Software"
G. Melnick
29 December 1982
Rev. A 19 February 1983
Rev. B 8 September 1983

IRT-368 "Instructions for Accessing the CFA VAX with the HP Terminal and Modem"
G. Melnick
29 December 1982

IRT-369 "Vibration Test Procedure for Electronics Subsystem EL-2 [As Run]"
MSFC
approx. 1 February 1983

IRT-370 "Vibration Test Procedure for Electronics Subsystem EL-3 [As Run]"
MSFC
approx. 1 February 1983

IRT-371 "EMI Test Procedure for Electronic Subsystems EL-2 and EL-3"
R. N. Watts
25 February 1983

IRT-372 "Thermal-Vacuum Test Procedure for Electronic Subsystems EL-2 and EL-3"
R. N. Watts
10 March 1983
Rev. A 22 March 1983
Rev. B 6 April 1983

IRT-373 "P4 Pressure Gauge Verification"

MTCP-C-IRT-374 "Electrical Systems Verification Testing of Infrared Telescope (IRT)"
MSFC

MTCP-C-IRT-375 "Procedure for Infrared Telescope (IRT) Systems Verification Testing with Cryogens"
MSFC

MTCP-C-IRT-376 "Acoustic Testing of Infrared Telescope (IRT)"
MSFC

MTCP-C-IRT-377 "Procedure for Infrared Telescope (IRT) Systems Reverification Testing with Cryogens Following Acoustic Test"
MSFC

MTCP-C-IRT-378 "Thermal/Vacuum Testing of Infrared Telescope (IRT)"
MSFC

IRT-379 "CGSE EL-2 Interface Test Procedure"
L. Coyle
D. Koch
20 March 1984

IRT-380 "Infrared Telescope Vacuum Cover Assembly NSI/Pressure Cartridge Installation"
MSFC

MTCP-C-IRT-381 "Pre-Shipment Electrical Functional Test of Infrared Telescope"
J. H. Lowery
As-Run 31 March 1984 – 7 April 1984

IRT-382 "Post-Shipment Functional Test Procedure"
L. Coyle
D. Koch
14 April 1984

IRT-383 "IRT High Vacuum Acquisition"
E. Urban
As Run on 18-20 April 1984

IRT-384 "PDSS EL-2 Interface Test Procedure"
L. Coyle
D. Koch
As Run on 18 April 1984

IRT-385 "Procedure for Installing the IRT onto the Spacelab Pallet"
D. Koch
10 May 1984

IRT-386 "KSC Level-IV Procedure for Adjustment of Electronic Baseline"
E. Young 25 May 1984 Rev. A

IRT-387 "Cold Functional Test Preparation Sheet"
KSC 9 July 1984

IRT-388 "Proposed Method of Detecting the Spacecraft Glow"
D. Koch 6 September 1984 Rev. A
13 February 1985 Rev. B

IRT-389 "Recovery from ECOS Crash"
D. Koch 25 September 1984

IRT-390 "Health Check Procedure for IRT Detector Subsystem"
E. Young 12 September 1983
Rev. A 11 October 1983
Rev. B 31 October 1983

IRT-391 "Experiment 5 Timeline for Spacelab-2"
D. Koch 14 March 1985

IRT-392 "Postmission Functional Test"
D. Koch ~15 August 1985
(revised from IRT-382)

A.4 IRT 400-499 Reports

IRT-401 "APART and GUERAP II Analysis of the Small Helium-Cooled Infrared Telescope for Spacelab-2"
Breault Research Organization — 30 December 1977

IRT-402 "Spacelab Focal Plane Heat Exchanger (Cold Finger)"
T.N. Gautier
W.M. Poteet — 14 November 1978

IRT-403 "A Small Helium-Cooled Infrared Telescope for Spacelab 2"
T.N. Gautier, III,
G.H. Rieke
F.J. Low and
W.F. Hoffmann — 14 March 1979

IRT-404 "Tests of Low Background Photo Conductors"
E.T. Young
F.J. Low — 14 March 1979

IRT-405 "Long Wavelength Spectral Response"
G.H. Rieke — 13 August 1979

IRT-406 "Cryogenic Subsystems Review of Small Helium-Cooled Infrared Telescope Experiment No. 5 of Spacelab 2 MSFC's Components"
E.W. Urban
L. Katz — 24 September 1979

IRT-407 "Leak Tests of SV3 Seal-Off Valves"
L. Katz — 24 September 1979

IRT-408 "Emergency Relief Venting of the Infrared Telescope Liquid Helium Dewar"
E.W. Urban — March 1980 (NASA TM-78271) Rev. A April 1981 (renumbered TM-82420 for Rev. A)

IRT-409 "Expected Measurements by the Quartz Crystal Microbalance (QCM) and the Cold Cathode Ionization Gauge (CCIG)"
G.G. Fazio — (Draft) 31 July 1981

IRT-410 "Prevention of Ice Blockage of Infrared Telescope Cryogenic Plumbing"

E.W. Urban 17 July 1980

IRT-411 "Subsystem Descriptions for EL-2 and EL-3"
K. Fredholm 26 January 1981
Rev. B 26 June 1981

IRT-412 "Cryostat Scan Drive Control System Design and Definition"
C.S. Cornelius 23 December 1980

IRT-413 "Burst Disk Test Summary"
G.R. Karr 29 January 1981

IRT-414 "IRT Weld Materials Controls and Analysis"
A.J. Verble, Jr. 18 March 1981

IRT-415 "Infrared Telescope Cryogen and Gas Servicing System (CGSS) Hazard Analysis"
E. Urban
L. Katz 23 March 1981

IRT-416 "Test Results of Spacelab-2 Infrared Telescope Focal Plane"
E.T. Young, et al. 16 April 1981

IRT-417 "IRT RAU Simulator Design Report"
A. Roy 4 May 1981

IRT-418 "Spacelab Gamma Irradiation Test"
University of Arizona 25 June 1981

IRT-419 "IRT Emergency Vent Plume"
E. Urban
D. Ladner 7 October 1981

IRT-420 "Safety Analysis of the IRT Dewar Subsystem"
R. Watts March 1982

IRT-421 "Using the IRT for Comet Halley Observations"
R. Watts 25 March 1982

IRT-422 "Linearity Test of the Flight Electronics"
G. Melnick (Preliminary) 21 April 1982

IRT-423 "Scan Drive Limits and Switching"
William C. Sutherland (approx. August 1982)

IRT-424 "Subsystem Summary"
R. Watts Initial Release 27 October 1982
to be updated frequently

IRT-425 "Encoder Calibration Data"
E.C. Smith 18 October 1982
D. Koch

IRT-426 "POCC PI Team Familiarization Handout Package: PI Team Familiarization at MSFC Huntsville Operation Support Center, October 16-18, 1984"
19 October 1984

IRT-427 "Analysis of Operation of the Scan Drive System When the Scan Limit Maximum Angle is Less Than the Minimum Angle"
MSFC 7 January 1985
Guidance Control and
Optical System Div.

IRT-428 "Integration Readiness Review Phase II"
MSFC 20 December 1984

IRT-429 "Final Technical Report, NASA Contract NAS8-32818, Infrared Telescope"
G. Karr, J. Hendricks (no date)
UAH Research Report #427

IRT-430 "Small Helium-Cooled Infrared Telescope Troubleshooting of IRT Deadband"
E. Young 22 February 1985

IRT-431 "Preliminary Mission Report and Amendment to Infrared Telesocpe (IRT) SL-2 Exp. 5"
G. Fazio 6 August 1985

IRT-432 "Summary of Operations"
D. Koch 1 October 1985

IRT-433 "Ninety-Day Science Report"
January 1986

IRT-434 "Spacelab-2 90-Day Post-Mission Science Report"
E.W. Urban November 1985

IRT-435 "Thermal Performance Evaluation of the Infrared Telescope Dewar Subsystem"
E.W. Urban April 1986

A.5 IRT 500-599 Software Documentation

IRT-501 "Flight Software Summary and Operating Guidelines"
D. Koch
5 August 1982
Rev. A 26 November 1982

A.6 IRT 1100-1199 Reflight Specifications and Requirements

(no documents issued)

A.7 IRT 1200-1299 Reflight Plans and Policies

(no documents issued)

A.8 IRT 1300-1399 Reflight Procedures

IRT-1301 "Post-Mission Functional Test Procedure"
L. Coyle, D. Koch 1 October 1985

IRT-1302 "NSI/Pressure Cartridge Removal"
E. Nash ~3/28/86
(E. Nash will send a copy as soon as it's signed off)

IRT-1303 "Sunshade Test and IRT Closeout"
E. Nash ~20 Oct 1986

A.9 IRT 1400-1499 Reflight Reports

(no documents issued)

A.10 IRT 1500-1599 Reflight Software Documentation

(no documents issued)

A.11 IRT 3000-3099 Procedures for Tests Conducted at KSC

This section is reserved for KSC test procedures written by E. Urban.

IRT SERVICING PROCEDURES:

IRT-3000	"IRT Level IV Vacuum and Cryogen Servicing"
IRT-3001	"IRT CITE Vacuum and Cryogen Servicing"
IRT-3002	"IRT Level I -- OPF Cryogen Servicing"
IRT-3003	"IRT Level I -- PAD Vacuum and Cryogen Servicing"
IRT-3004	"IRT Post Flight Vacuum and Cryogen Servicing"
IRT-3005	"IRT High Vacuum Acquisition"
IRT-3006	"IRT Liquid Helium Fill/Topoff"
IRT-3007	"IRT Liquid Helium Conversion and Low Pressure Fill"
IRT-3008	"IRT Low Pressure Helium Fill/Topoff"
IRT-3009	"IRT Fill Apparatus Closeout"
IRT-3010	"IRT Vent Apparatus Closeout"
IRT-3011	"IRT Cold Valve Operations"
IRT-3012	"IRT Valve Actuator Cover Operations"
IRT-3013	"IRT Supply Dewar (SD) Fill"
IRT-3014	"IRT Supply Dewar (SD) Conversion to Superfluid (SHe) and SHe Storage"
IRT-3015	"IRT Supply Dewar (SD) Refill"
IRT-3016	"IRT Liquid Nitrogen Trap Fill (Leak Checker and RP1)"
IRT-3017	"IRT Evacuation Valve O-Ring Service (V3, V4, V8, V21, V22)"
IRT-3018	"IRT GN_2 Pressurization and Backfill"
IRT-3019	"IRT GHe Pressurization and Backfill"

IRT-3020 "IRT Vacuum System Leak Checks"

A.12 IRT Publications

"Infrared Background Starlight: Observations and Galaxy Models," Fazio, G.G., Dame, T.M., and Kent, S. 1989, to be published in Proc. IAU Symposium 139, *Galactic and Extragalactic Background Radiation*, Heidelberg.

"Overview of Measurements from the Infrared Telescope on Spacelab-2," Koch, D.G., Melnick, G.J., Fazio, G.G., Rieke, G.H., Low, F.J., Hoffmann, W., Young, E.T., Urban, E.W., Simpson, J.P., Witteborn, F.C., Gautier, T.N., III, and Poteet, W. 1988, Astrophysical Letters and Communications **27**, 211.

"Preliminary Results of the Spacelab-2 Infrared Telescope Survey of the Galactic Plane at 2.4μm," Melnick, G.J., Fazio, G.G., Koch, D.G., Rieke, G.H., Young, E.T., Low, F.J., Hoffmann, W.F., Gautier, T.N. 1987, in *The Galactic Center* (AIP Conference Proceedings) **155**, 157.

"Infrared Observations of Contaminants from Shuttle Flight 51-F," Koch, D.G., Fazio, G.G., Hoffmann, W., Melnick, G., Rieke, G., Simpson, J., Witteborn, F., and Young, E. 1987, *Advances in Space Research* **7**, No. 5, 211.

"Preliminary Flight Performance of the Infrared Telescope on Spacelab 2," Urban, E.W. and Ladner, D.R. 1986, Cryogenics **26**, 122.

"First Results from Spacelab-2," Urban, E.W. 1986, Nature **319**, 540.

"Thermal Performance Evaluation of the Infrared Telescope Dewar Subsystem," Urban, E.W. April 1986, NASA Technical Memorandum 86543.

"Operation of the Cryogenic System of the Infrared Telescope on Spacelab-2," Urban, E. and Ladner, D. 1986, *Proc. of XI International Cryogenic Engineering Conf.*, (London: Butterworth), p. 341.

"Spacelab 2: Science in Orbit," Smith, H. and Page, T.L., November 1986, *Sky and Telescope*, pp. 438-445.

"Straylight Performance of the Spacelab-2 Infrared Telescope at E-Band," Dinger, A. 1986, NASA Technical Note TN-86-7104-941-17, Rev. 1.

"Infrared Measurements of Spacecraft Glow Planned for Spacelab 2," Fazio, Giovanni G. and Koch, David G. 1985, *Second Workshop on Spacecraft Glow*, eds. J.H. Waite, Jr., and T.W. Moorehead (NASA Conf. Publ. 2391).

"Infrared Telescope (IRT) System Cryogenic Performance," Urban, E.W. and Ladner, D.R. 1984, Proc. SPIE **509**, 216.

"The Infrared Telescope on Spacelab Two," Koch, D., Fazio, G.G., Traub, W.A., Rieke, G.H., Gautier, T.N., Hoffmann, W.F., Low, F.J., Poteet, W., Young, E.T., Urban, E.W., and Katz, L. 1982, Space Optics **183**, 16; revised version: 1982, Optical Engineering **21**, 141.

"Sensitive Observations with the Spacelab-2 Infrared Telescope," Young, E.T., Rieke, G.H., Gautier, T.N., Hoffmann, W.F., Low, F.J., Poteet, W., Fazio, G.G., Koch, D., Traub, W.A., and Urban, E.W. 1982, Proc. SPIE **363**, 39.

"Performance of the He II Dewar Subsystem for the Spacelab-2 Infrared Telescope," Karr, G.R., Hendricks, J.B., Urban, E.W., and Ladner, D.R. 1982, *Proc. Ninth International Engineering Conference*, eds. K. Yasukochi and H. Nagano (London: Butterworth), p. 49.

"Emergency Relief Venting of the Infrared Telescope Liquid Helium Dewar," Urban, E.W. April 1981, NASA Technical Memorandum 82420 (2d edition).

"Application of JFets to Low Background Focal Planes in Space," Low, F.J. 1981, *Infrared Astronomy -- Scientific/Military Thrusts and Instrumentation* **280**, 56.

"Test Results of Spacelab-2 Infrared Telescope Focal Plane," Young, E.T., Rieke, G.H., Gautier, T.N., Hoffmann, W.F., Low, F.J., Poteet, W., Fazio, G.G., Koch, D., Traub, W.A., Urban, E.W., and Katz, L. 1981, *Infrared Astronomy -- Scientific/Military Thrusts and Instrumentation* **280**, 12.

"Mapping the Infrared Background Radiation from the Shuttle," Koch, D., Fazio, G.G., Traub, W.A., Urban, E.W., Katz, L., Rieke, G.H., Gautier, T.N., Hoffmann, W.F., Low, F.J., Poteet, W., and Young, E.T. 1981, *Shuttle Pointing of Electro-Optical Experiments* **265**, 257.

"Development and Integration of the Infrared Telescope for Spacelab," Urban, E.W., Katz, L., and Watts, R. 1981, ASME Journal of Proceedings, p. 1.

"A Cryogenic System for the Small Infrared Telescope for Spacelab 2," Urban, E.W., Katz, L., Hendricks, J.B., and Karr, G.R. 1981, *Proc. Conference on Refrigeration for Cryogenic Sensors and Electronic Systems*, Boulder, Colorado, October 1980. NBS Special Publication No. 607, 117.

"Cryogenic Subsystem Performance of the Infrared Telescope for Spacelab 2," Karr, G.R., Hendricks, J.B., Urban, E.W., Katz, L., and Ladner, D. 1980, *International Cryogenic Engineering Conferences* **8**, 38.

"The Spacelab 2 Infrared Telescope Cryogenic System," Urban, E.W., Katz, L., Hendricks, J.B., and Karr, G.R. 1979, Space Optics **183**, 40.

"A Small Helium-Cooled Infrared Telescope for Spacelab 2," Gautier, T.N., III, Rieke, G.H., Low, F.J., and Hoffmann, W.F. 1979, *Instrumentation in Astronomy III* **172**, 264.

"Tests of Low Background Photo Conductors," Young, E.T. and Low, F.J. 1979, *Instrumentation in Astronomy III* **172**, 184.

"Cryogenic Helium II Systems for Space Applications," Urban, E.W., Katz, L., Hendricks, J.B., and Karr, G.R. *Proceedings of International Symposium on Spacecraft Thermal and Environmental Control Systems*, Münich, October 1978, 507; ESA SP-139.

"A Cryogenic Helium II System for Spacelab," Urban, E.W., Katz, L., Hendricks, J.B., and Karr, G.R. *Proceedings of the Seventh International Cryogenic Engineering Conference*, London, July 1978, 113.

A.13 IRT Presentations

"Preliminary Results of the Spacelab-2 Infrared Telescope Survey of the Galactic Plane at 2.4μm", Melnick, G.J., Fazio, G.G., Koch, D.G., Rieke, G.H., Young, E.T., Low, F.J., Hoffmann, W.F., Gautier, T.N., presented at the Symposium on the Galactic Center, in honor of Charles Townes, 25 October 1986, U. Cal., Berkeley.

"Infrared Observations of Contaminants from Shuttle Flight 51-F", Koch, D.G., Fazio, G.G., Hoffmann, W.F., Melnick, G.J., Rieke, G., Simpson, J., Witteborn, F., Young, E., presented at the Twenty-sixth Plenary meeting of COSPAR, Workshop XII, July 1986, Toulouse France. To appear in *Advances in Space Research 1986.*

"Preliminary Results of the Spacelab-2 Infrared Telescope Experiment", Koch, D.G., Fazio, G.G., Melnick, G.J., Rieke, G.H., Low, F.J., Young, E.T., Hoffmann, W.F., Gautier, T.N., Urban, E.W., Ladner, D.R., Witteborn, F.C., Simpson, J.P. Presented at the 168th AAS Meeting, Session 10, 23-24 June 1986, Ames, Iowa.

"The Spacelab-2 Helium-Cooled Infrared Telescope Experiment," Fazio, G.G. Presented at the Shuttle Environmental Workshop, 5-7 October 1982, Calverton, Maryland.

"Sensitive Observations with the Spacelab 2 Infrared Telescope," Young, E.T., Rieke, G.H., Gautier, T.N., Hoffmann, W.F., Low, F.J., Poteet, W., Fazio, G.G., Koch, D., Traub, W.A., and Urban, E.W. Presented at the SPIE Seminar on Advanced Remote Sensing, 27 August 1982, San Diego, California.

"IR Detectors for Space Astronomy", Young, E.T., presented at COSPAR Meeting, May 1982.

"Development and Integration of the Infrared Telescope for Spacelab," Urban, E.W., Katz, L., and Watts, R. Presented at the Eleventh Intersociety Conference on Environmental Systems, 13-15 July 1981, San Francisco, California.

APPENDIX B

SAMPLE PLOTS OF THE DATA

APPENDIX B

SAMPLE PLOTS OF THE DATA

Data plots illustrative of the various signals seen in the data are provided for Day 212/20:08 to 212/20:48 for S-, A-, and E-bands so the effects at different wavelengths can be seen. Features of the plots are as follows: The narrow upper plot is of the telescope scan angle which generally varies from 45 to 135 degrees, except that this is shortened to avoid the sun by 45 degrees and the moon by 20 degrees. The moon avoidance can be seen from 20:37 to 20:43. Referring to Figure 2 in in the main text of this report, 90° is vertical out of the Shuttle bay, 135° is to port, and 45° is to starboard. Between the upper and lower plot there is a black bar which indicates day (blank) or night (black bar). This is accurate to within about one minute of actual sunrise/sunset. The letter notation under various features has the following meanings:

G	A result of a scan towards or across the galactic plane
T	A thruster firing
M	Stray light from the moon
D	A dust particle
CR	A cosmic ray (only a few typical events marked)

Plots are provided at different vertical scales so that both the astrophysical signal

can be seen and the full amplitude of the thruster can be seen. The S and A detectors saturated at 32768 counts.

The zero flux level (cold shutter closed) for each band was at about 550 counts in S, about 1100 counts in A, and about 80 counts in E3. The high background in A (from 2600 to 3000 counts) was due to the local environment and varied considerably with time. The high background in E3 (about 1500 counts) was due to scattering from the primary mirror of radiation from the warm forebaffle. The flux calibrations for each band are given in Table 12 of the main text.

Figures B1 – B4

These figures cover the time period 212/20:08 to 20:48 for the 2–3 μm data. The data were averaged over 200 samples (the original data were sampled at 1024 samples per second). These data also had the effects of an electronic RC tail removed for the most part. This is evident from Figure B-1a which is just the raw data averaged. The justification for this was the persistence of the tail following a thruster firing while the cold shutter was closed. The tail appears to be insignificant in the other detector bands. Also in Figure B-1a none of the cosmic ray hits have been edited out.

Figures B-5 – B-8

These figures are similar to Figures B-1 – B-4 except that the vertical scale goes to saturation at 32000.

Figures B-9 – B-12

These figures cover the time period 212/20:08 to 20:48 for the 4.5–9.5 μm data. The data were averaged over 200 samples (the original data were sampled at 1024 samples per second).

Figures B-13 – B-16

These figures are similar to Figures B-9 – B-12 except that the vertical scale goes to saturation at 32000.

Figures B-17 – B-21 cover the time period 212/20:08 to 20:48 for the 77–115 μm data. The data were averaged over 200 samples (the original data were sampled at 1024 samples per sec). The structure with the major peaks occurring at 135 degrees is for the most part due to spacecraft contamination. Unfortunately, when the scans are across the galactic plane from 20:15 to 20:30 there is a data

gap. Therefore, as an intensity comparison Figure B-21 is a scan of the same region but from the next orbit, 21:45 to 21:55. In Figure B-21, from 21:50:09 to 21:50:43 and from 21:50:51 to 21:52:09, the cold shutter was closed.

Figures B-22 – B-25

These figures are similar to Figures B-17 – B-20 except that the vertical scale has been expanded to permit plotting of the full amplitude of the thrusters.

Figures B-26 and B-27

These figures have both the amplitude and time scales expanded to provide better resolution of the details of the thruster firings at 24:14 and 20:46.

Figure B-28

This figure shows the sky coverage in galactic coordinates for the time period 212/20:08 to 20:48. The sun was at $l = -150$, $b = 34.63$, the moon was at $l = 42.3$, $b = -52.13$. The scan angle minimums about 45 degrees were towards the galactic center.

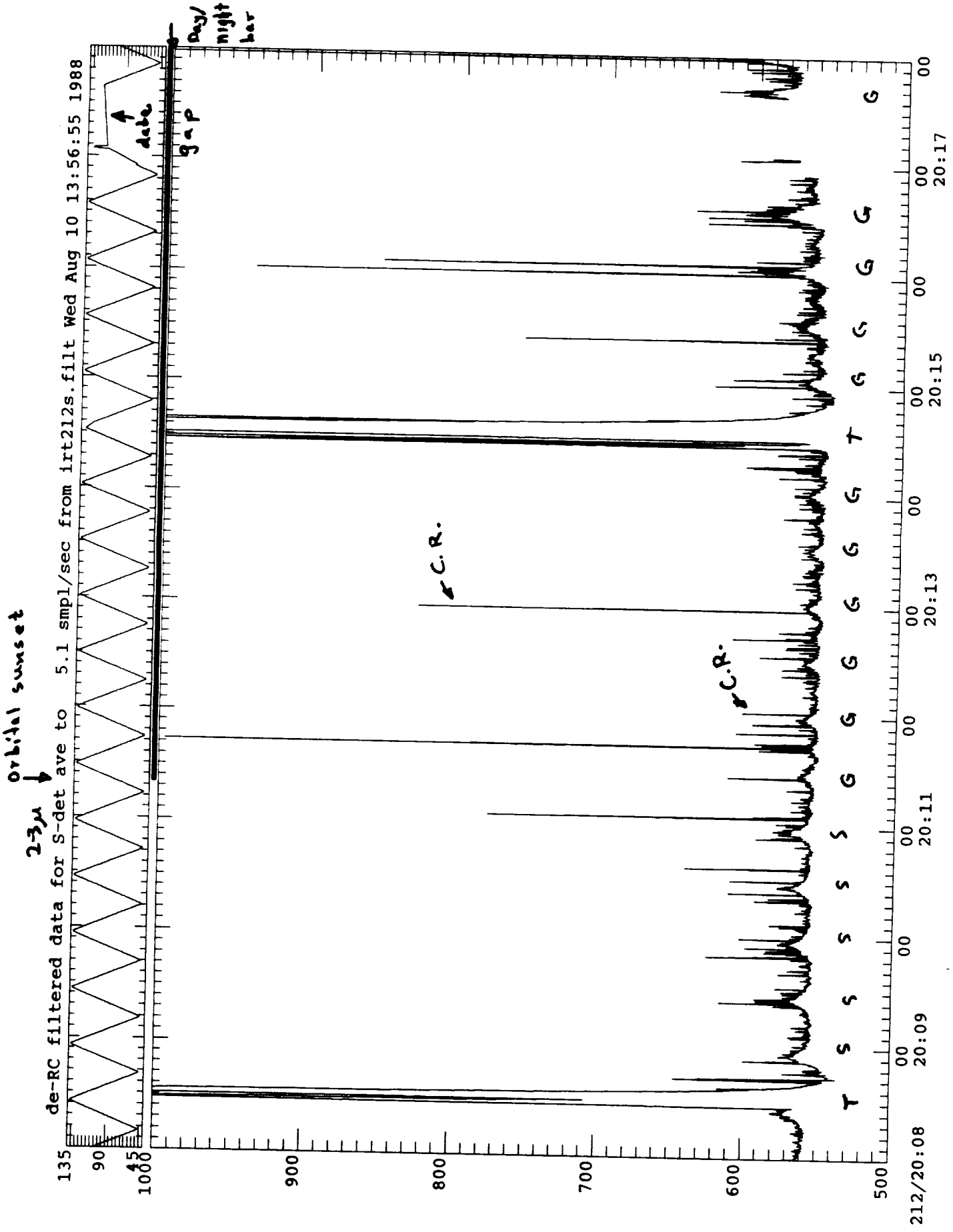
de-RC filtered data for S-det ave to 5.1 smpl/sec from irt212s.filt Wed Aug 10 13:56:55 1988
orbital sunset
2.3μ
Day/night bar
gap
data
C.R.
C.R.
135
90
45
1000
900
800
700
600
500
212/20:08
20:09
20:11
20:13
20:15
20:17

Figure B-1

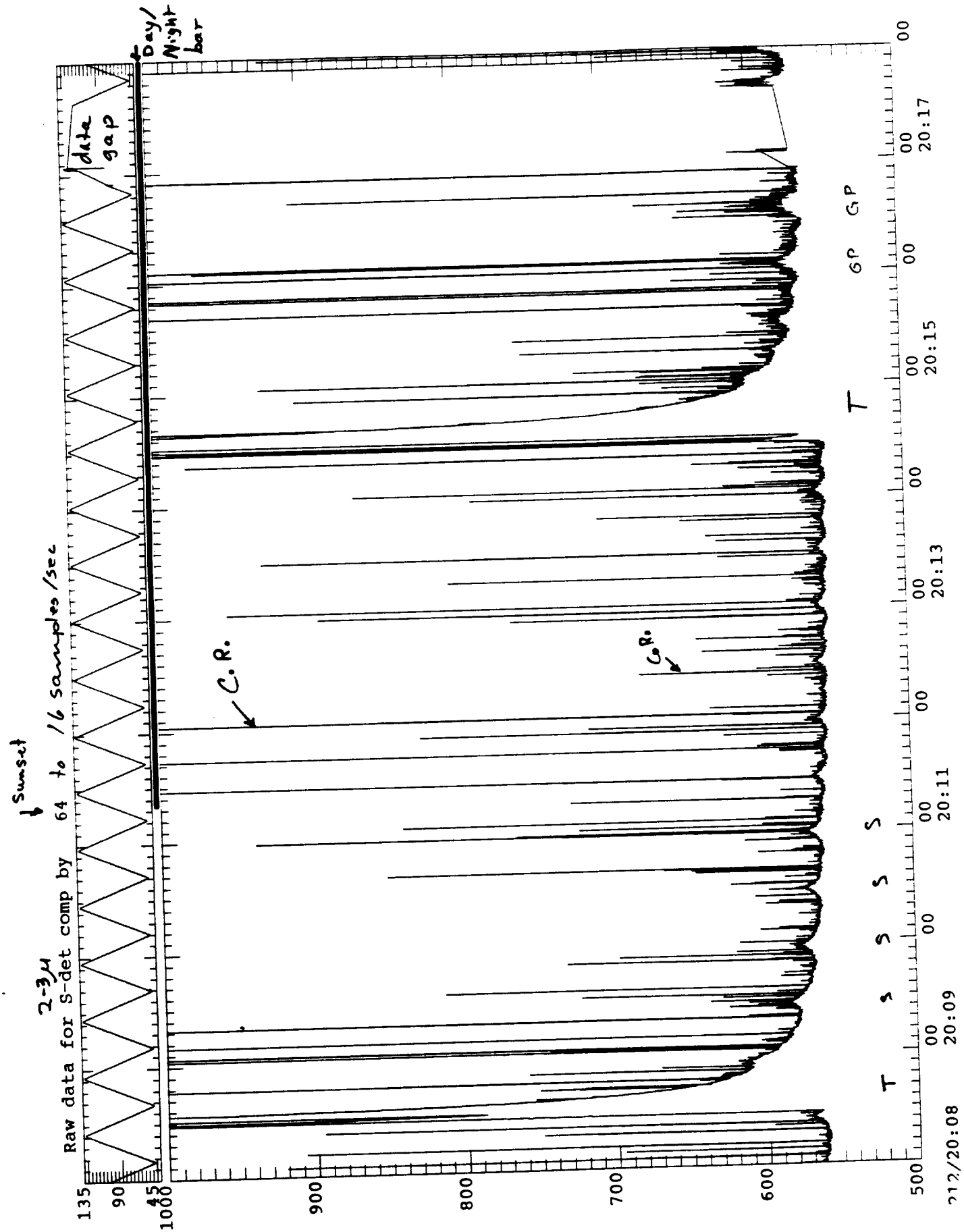
Day/
Night
bar
data
gap
Sunset
2-3μ
Raw data for S-det comp by 64 to 16 samples/sec
C.R.
C.R.
135
90
45
1000
900
800
700
600
500
T S S S S
T GP GP
00
20:09
20:11
20:13
20:15
20:17
212/20:08

Figure B-1a

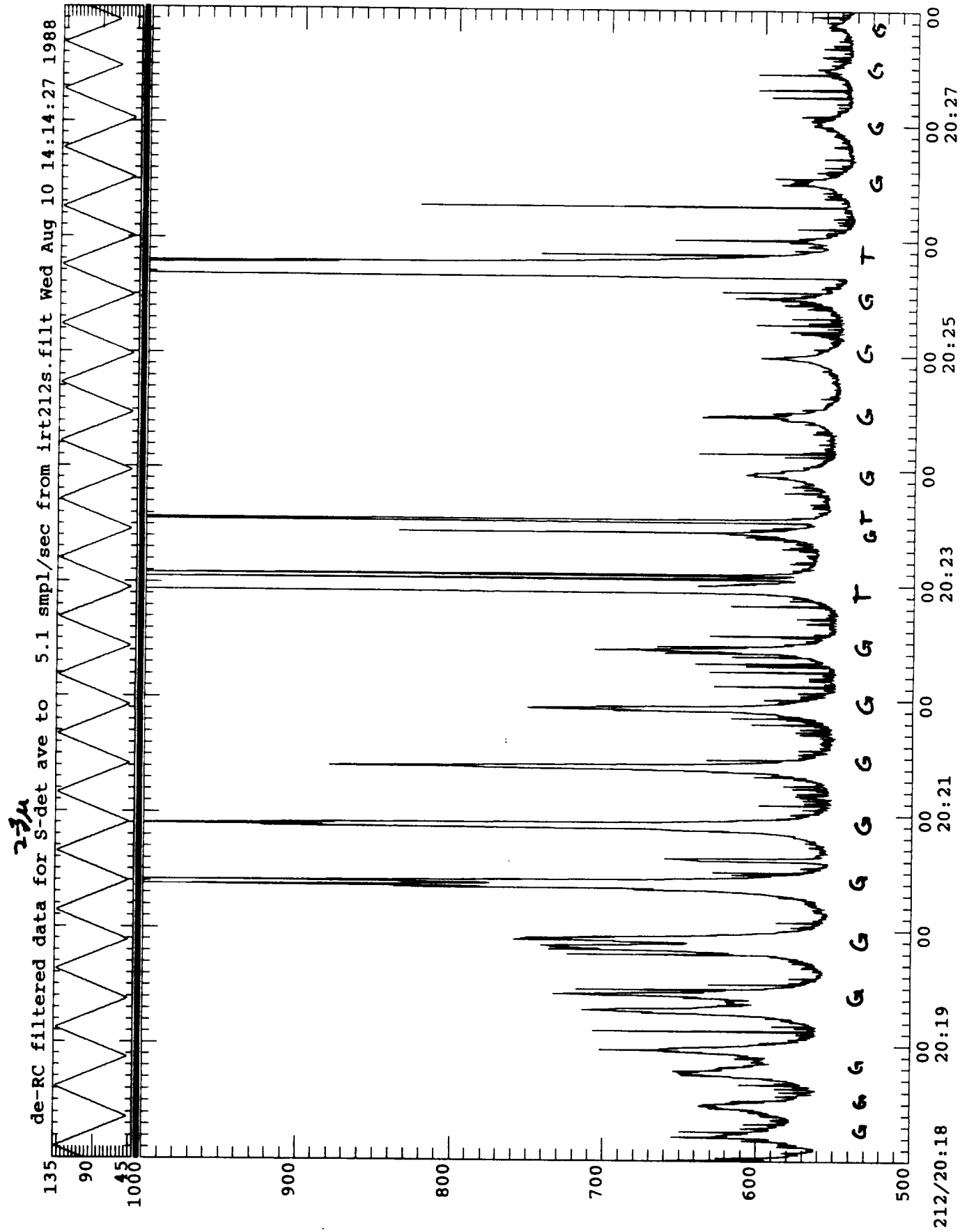
de-RC filtered data for S-det ave to 5.1 smpl/sec from irt212s.filt Wed Aug 10 14:14:27 1988
2.3μ
135
90
45
0
1000
900
800
700
600
500
212/20:18
00
20:19
00
20:21
00
20:23
00
20:25
00
20:27
00

Figure B-2

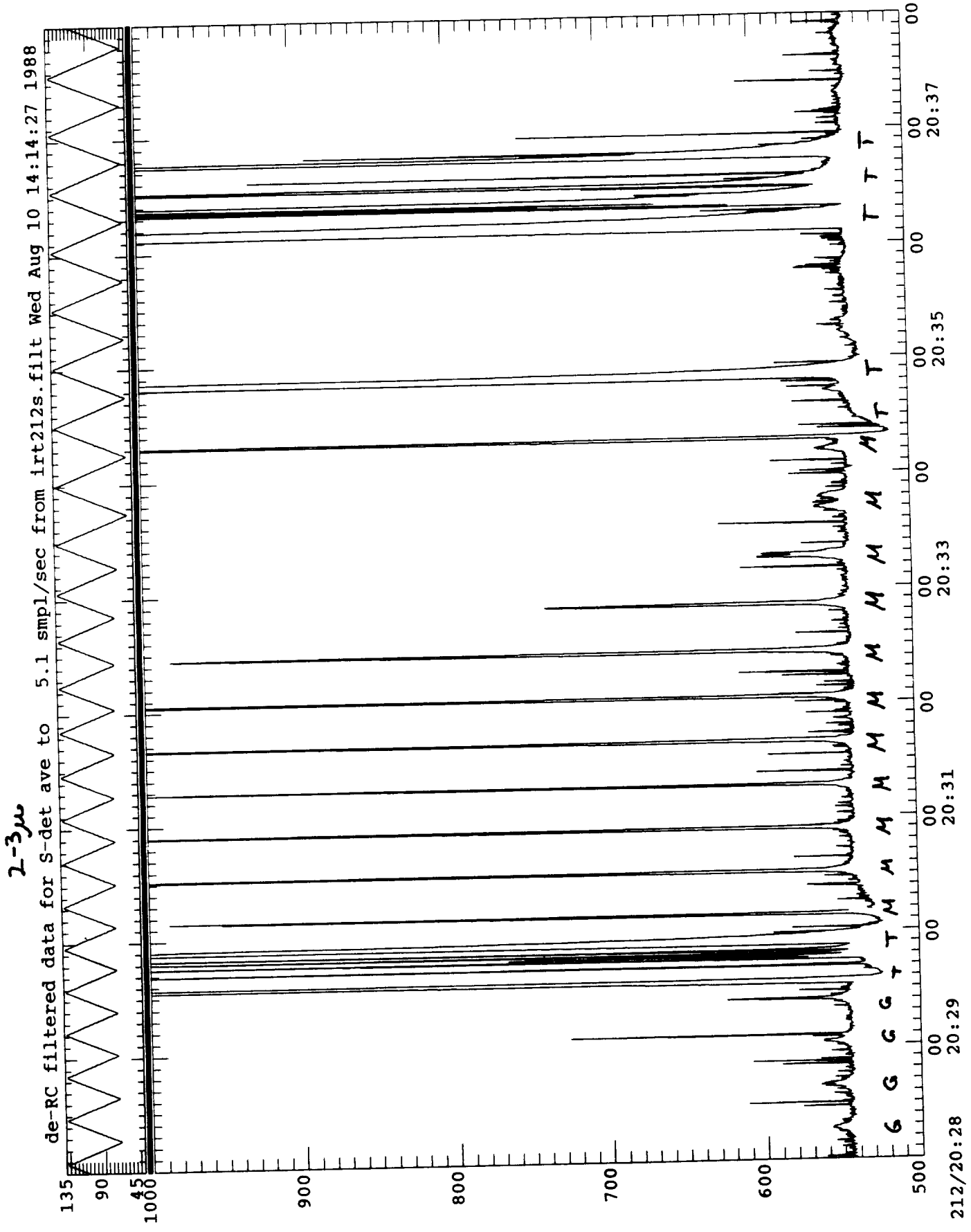
2-3μm
de-RC filtered data for S-det ave to 5.1 smpl/sec from irt212s.filt Wed Aug 10 14:14:27 1988
135
90
45
1000
900
800
700
600
500
212/20:28
20:29
20:31
20:33
20:35
20:37

Figure B-3

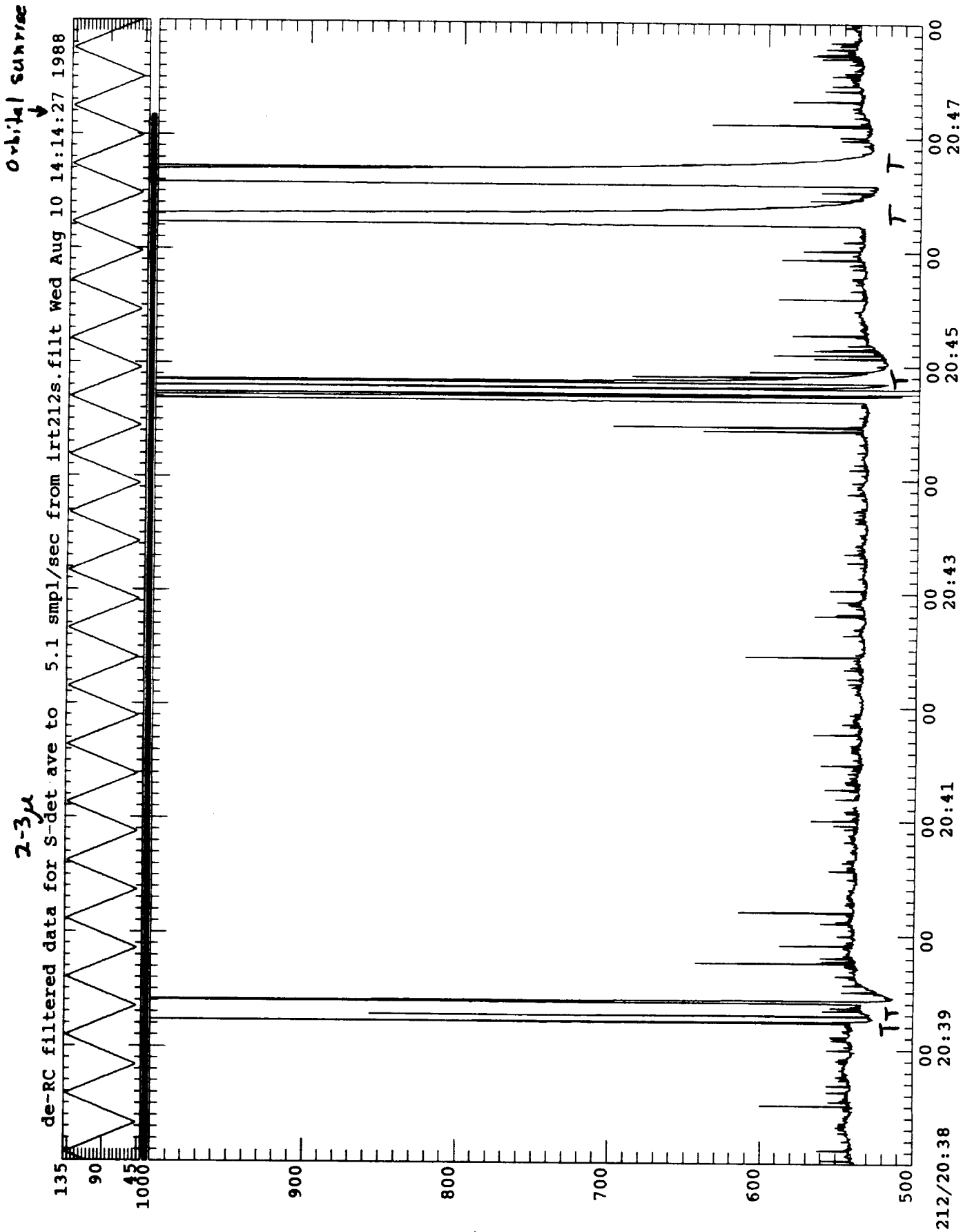
Orbital sunrise
2-3μ
de-RC filtered data for S-det ave to 5.1 smpl/sec from lrt212s.filt Wed Aug 10 14:14:27 1988
135
90
45
1000
900
800
700
600
500
212/20:38
00
20:39
00
20:41
00
20:43
00
20:45
00
20:47
00

Figure B-4

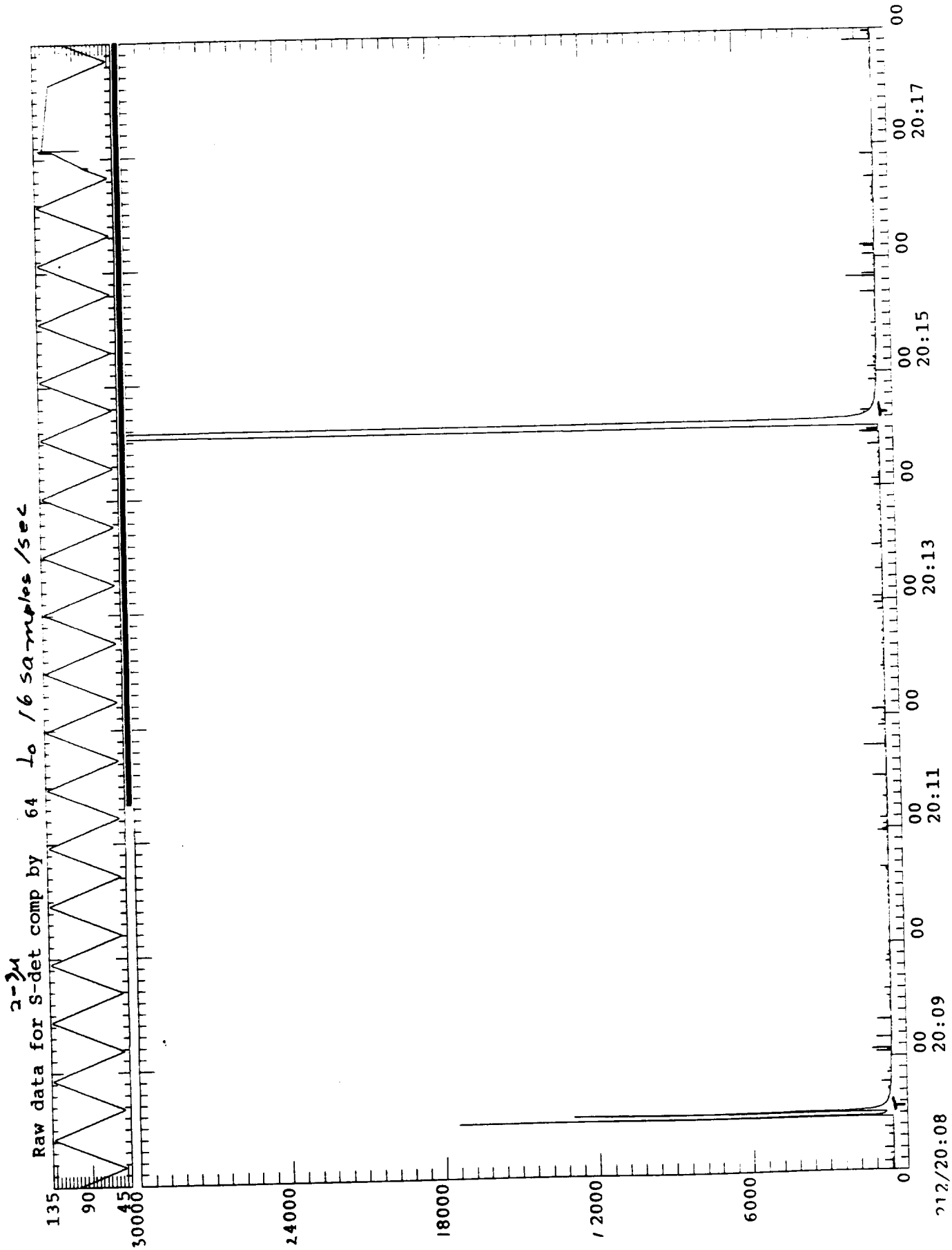
2-3μ
Raw data for S-det comp by 64 to 16 samples/sec
135
90
45
0
30000
24000
18000
12000
6000
0
00
20:09
00
20:11
00
20:13
00
20:15
00
20:17
00
212/20:08

Figure B-5

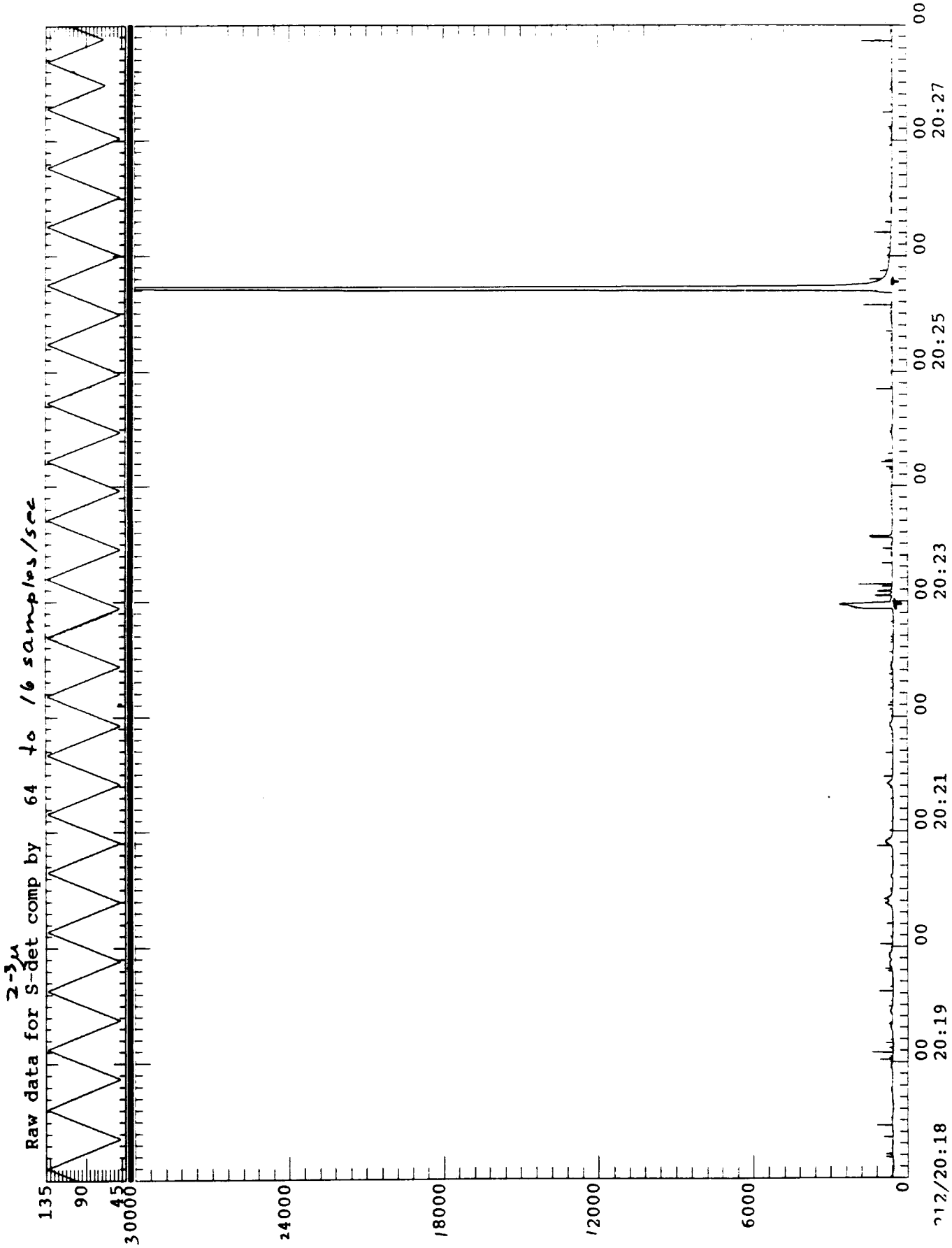
Raw data for S-det comp by 64 to 16 samples/sec
2-3μ
135
90
45
0
30000
24000
18000
12000
6000
0
00
20:18
20:19
20:21
20:23
20:25
20:27

Figure B-6

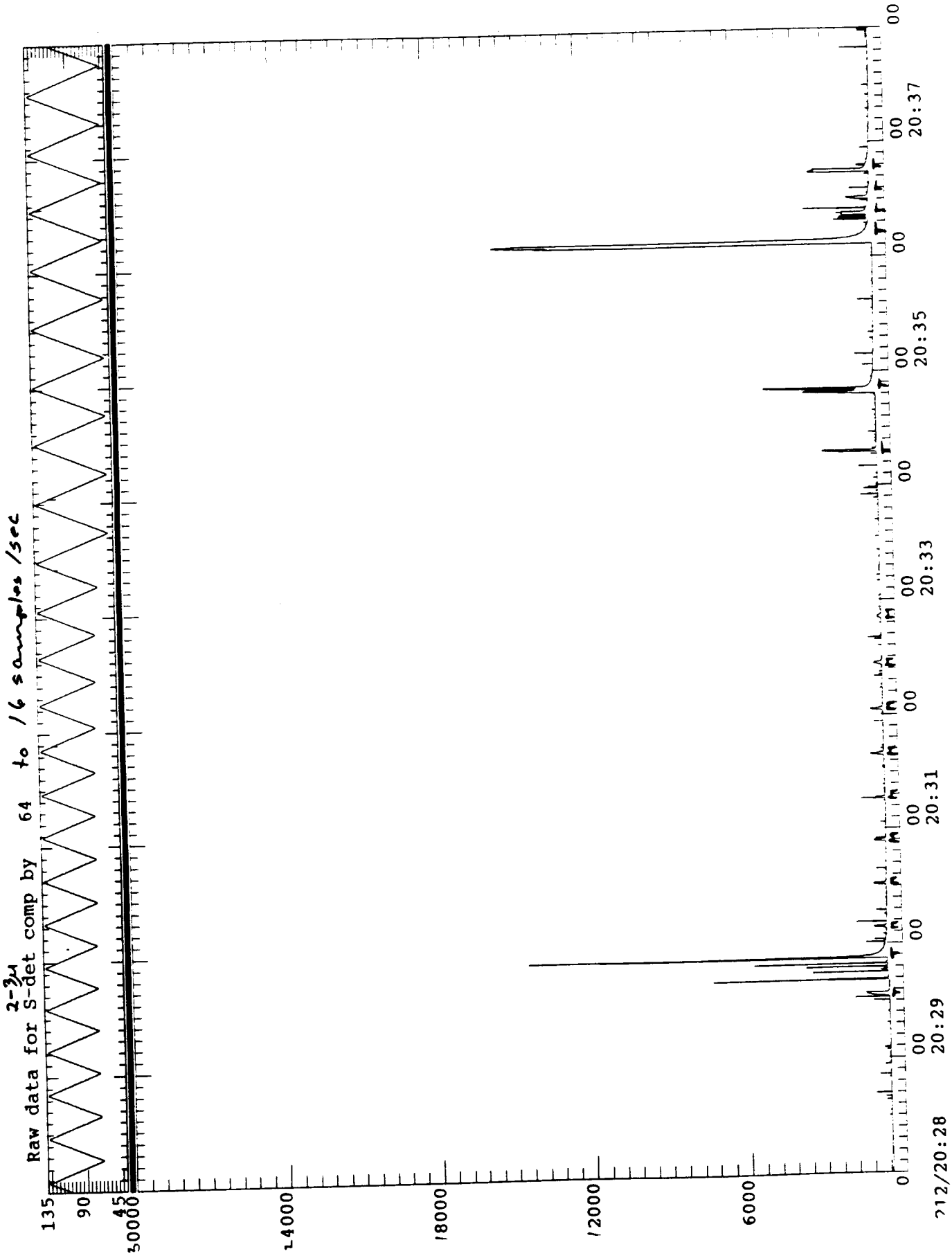
Raw data for S-det comp by 64 to 16 samples/sec
2-3μ
135
90
45
30000
24000
18000
12000
6000
0
00
20:29
00
20:31
00
20:33
00
20:35
00
20:37
00
212/20:28

Figure B-7

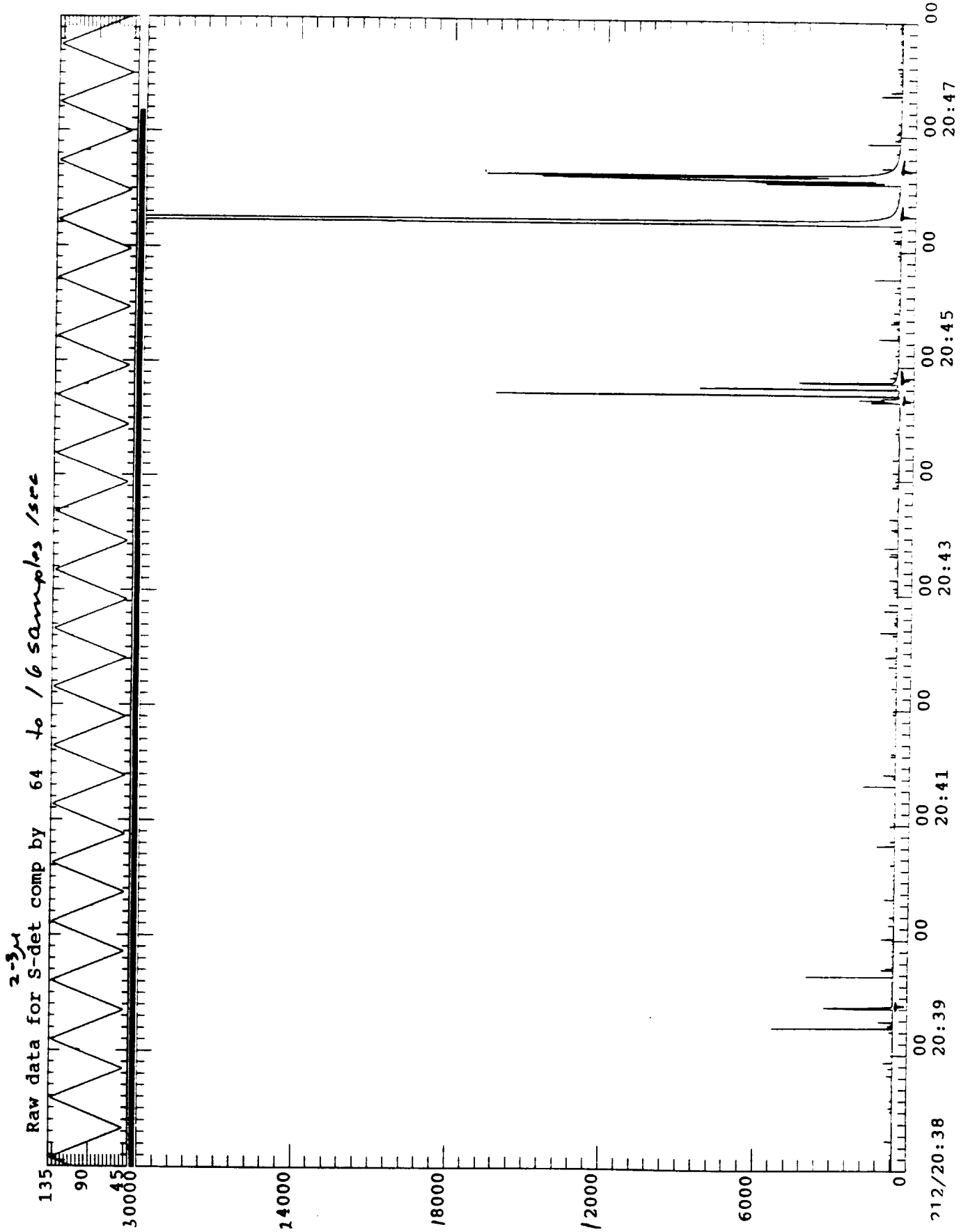
2-3μ
Raw data for S-det comp by 64 to 16 samples/sec
135
90
45
30000
14000
18000
12000
6000
0
212/20:38
00
20:39
00
20:41
00
20:43
00
20:45
00
20:47
00

Figure B-8

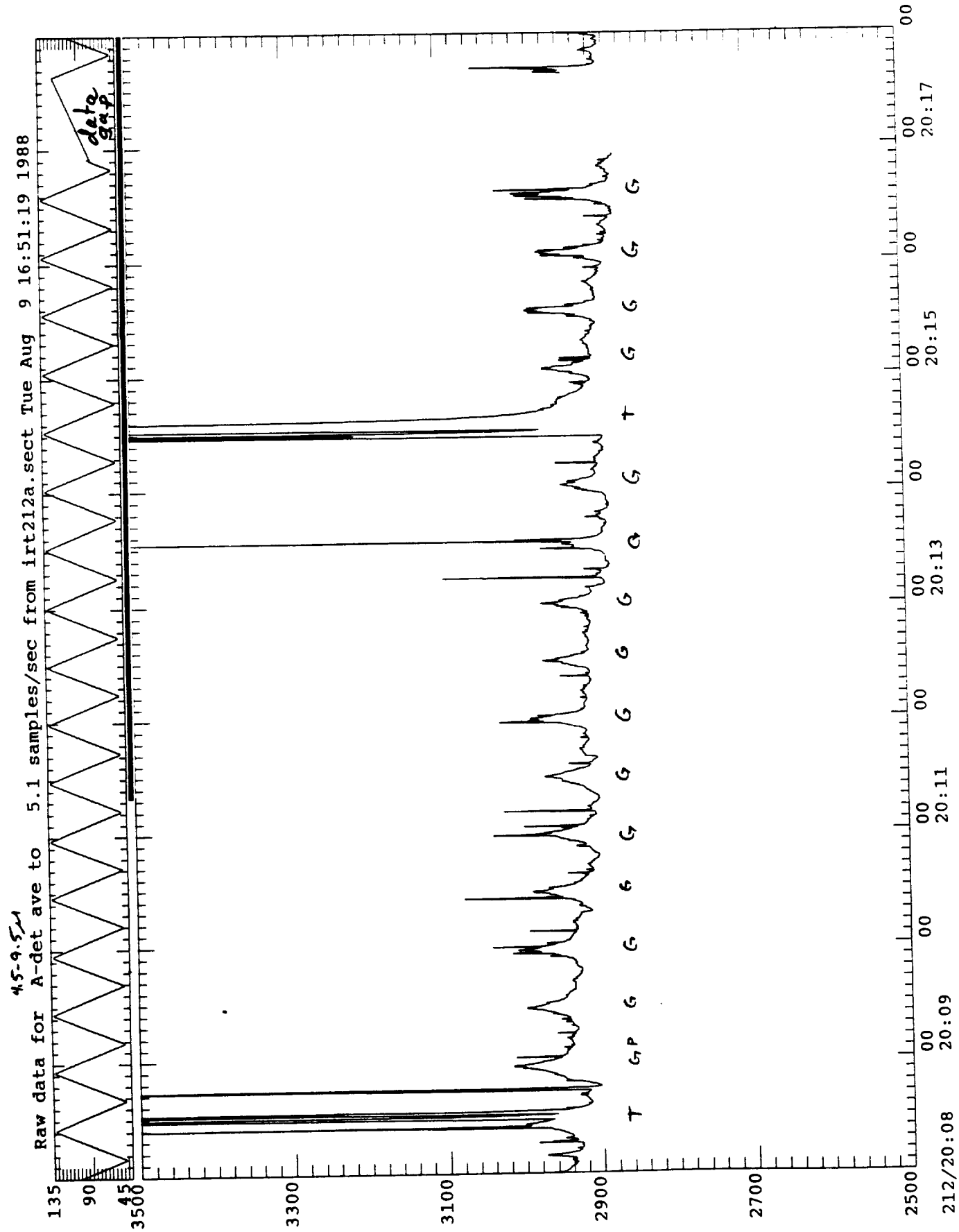
45-9.5m
Raw data for A-det ave to 5.1 samples/sec from irt212a.sect Tue Aug 9 16:51:19 1988
data gap
135
90
45
3500
3300
3100
2900
2700
2500
212/20:08
20:09
20:11
20:13
20:15
20:17

Figure B-9

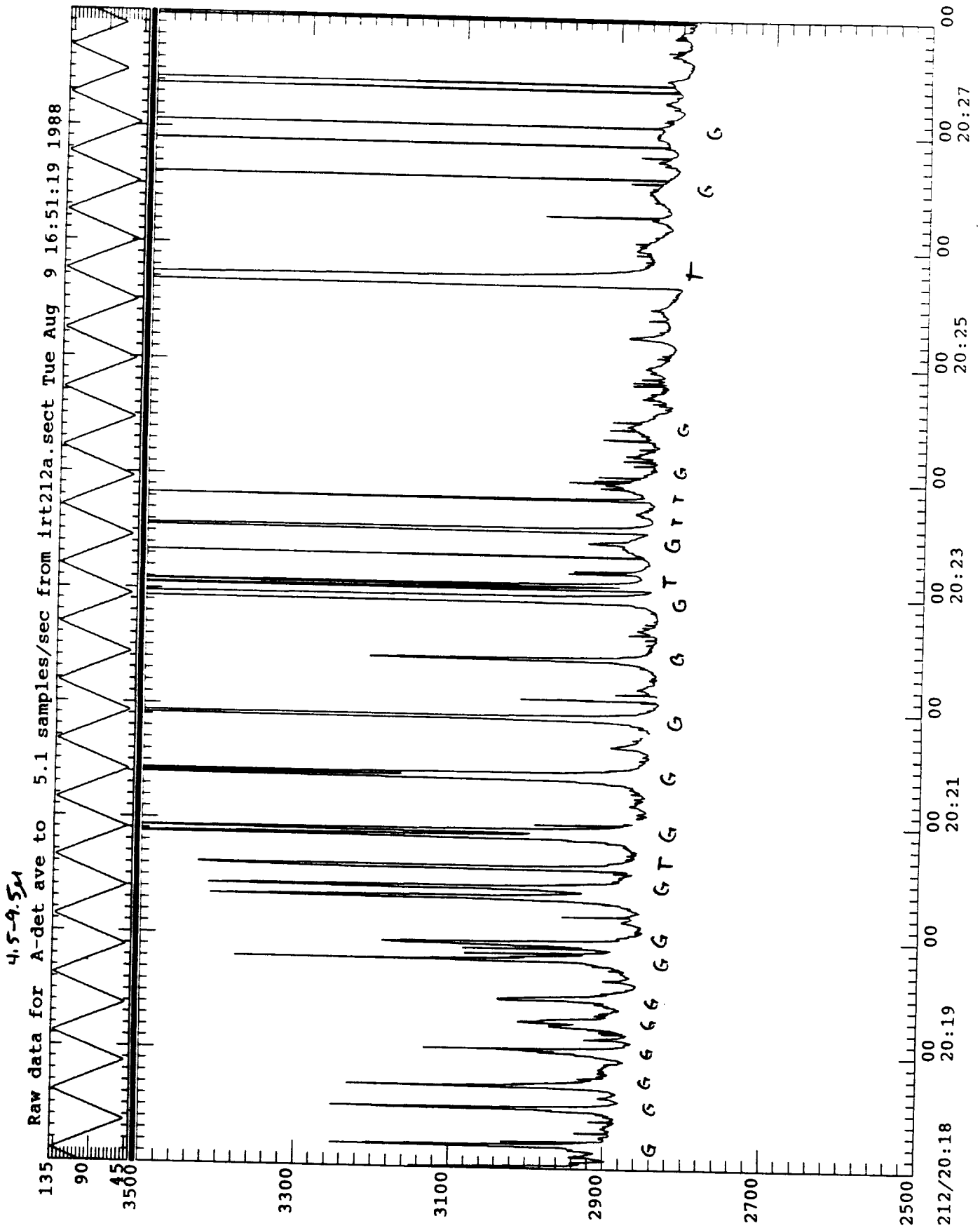
4.5-9.5μ
Raw data for A-det ave to 5.1 samples/sec from lrt212a.sect Tue Aug 9 16:51:19 1988
135
90
45
0
3500
3300
3100
2900
2700
2500
212/20:18
20:19
20:21
20:23
20:25
20:27
00

Figure B-10

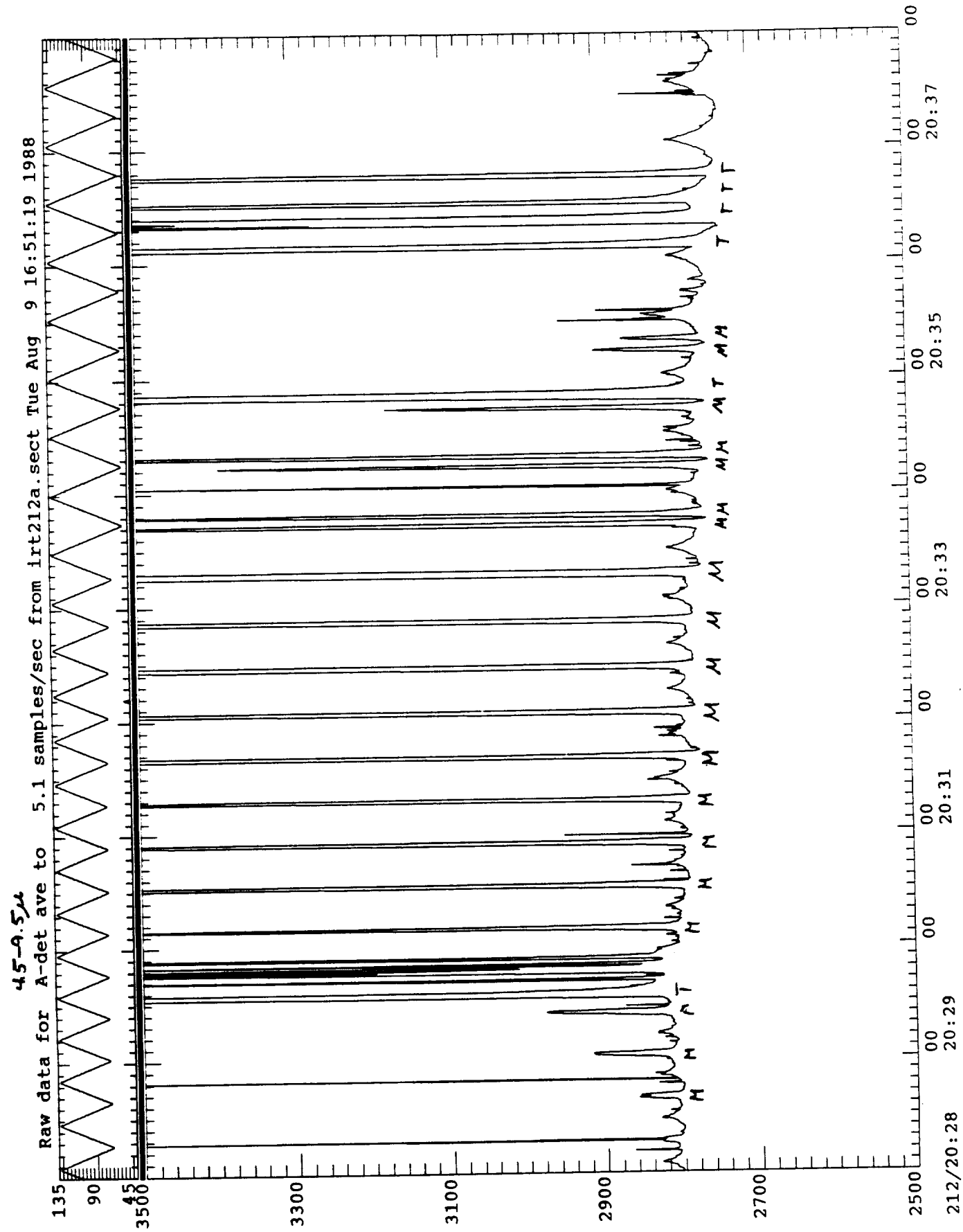
45-9.5μ
Raw data for A-det ave to 5.1 samples/sec from irt212a.sect Tue Aug 9 16:51:19 1988
135
90
45
3500
3300
3100
2900
2700
2500
212/20:28
00
20:29
00
20:31
00
20:33
00
20:35
00
20:37
00

Figure B-11

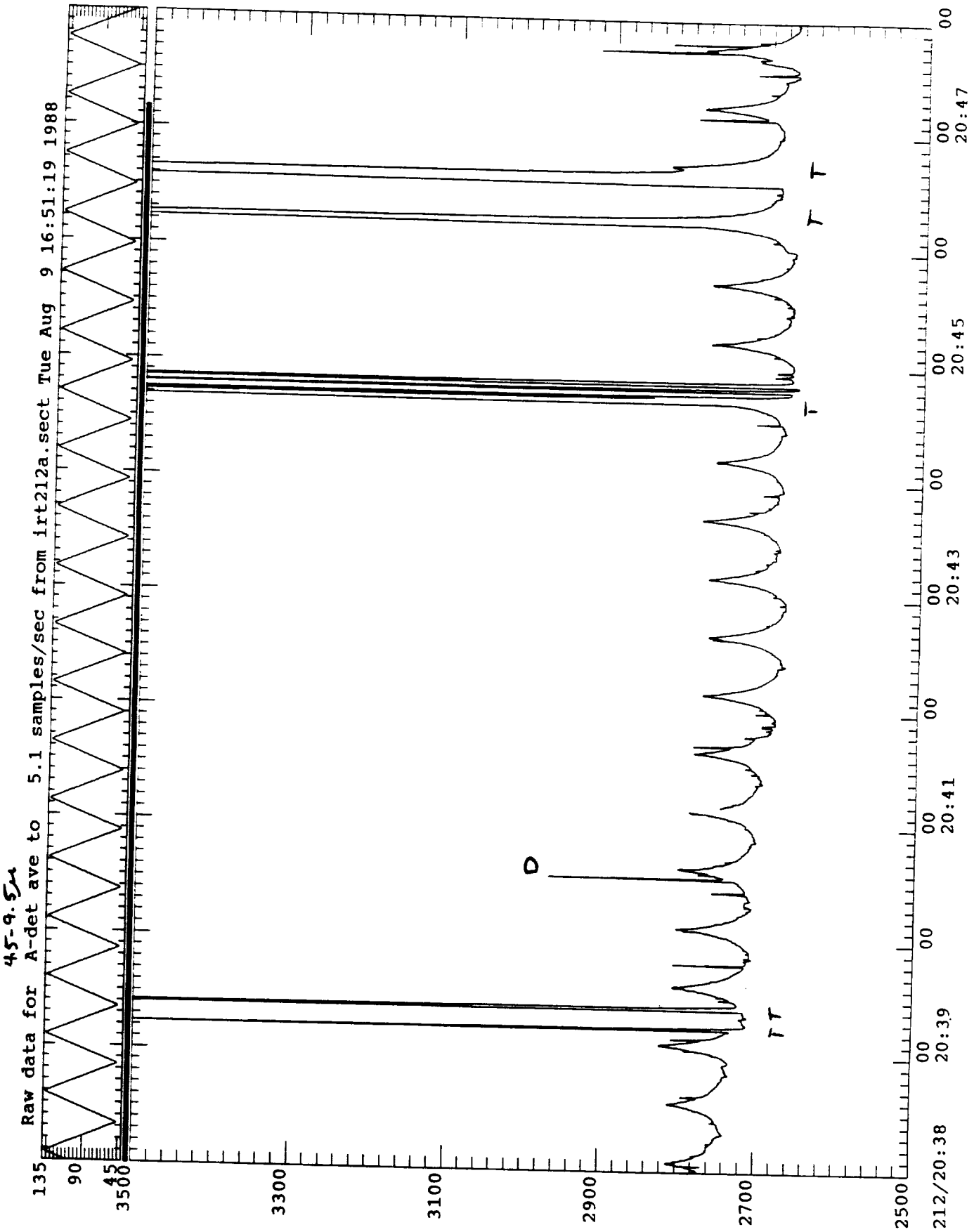
45-9.5m
Raw data for A-det ave to 5.1 samples/sec from irt212a.sect Tue Aug 9 16:51:19 1988
135
90
45
3500
3300
3100
2900
2700
2500
D
T
T
T
T
T
212/20:38
00
20:39
00
20:41
00
20:43
00
20:45
00
20:47
00

Figure B-12

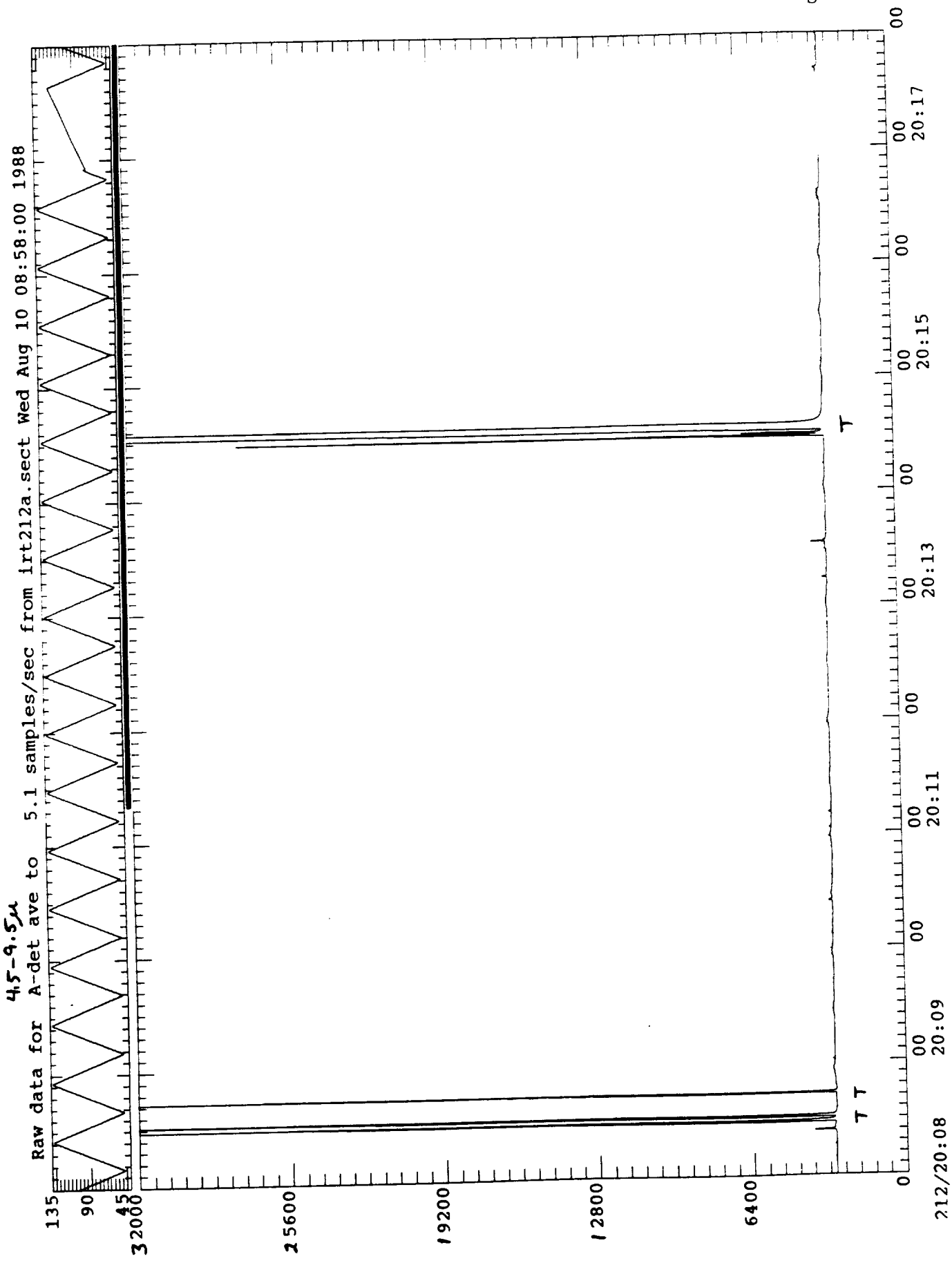
4.5-9.5μ
Raw data for A-det ave to 5.1 samples/sec from irt212a.sect Wed Aug 10 08:58:00 1988
135
90
45
0
32000
25600
19200
12800
6400
0
212/20:08
00
20:09
00
20:11
00
20:13
00
20:15
00
20:17
00

Figure B-13

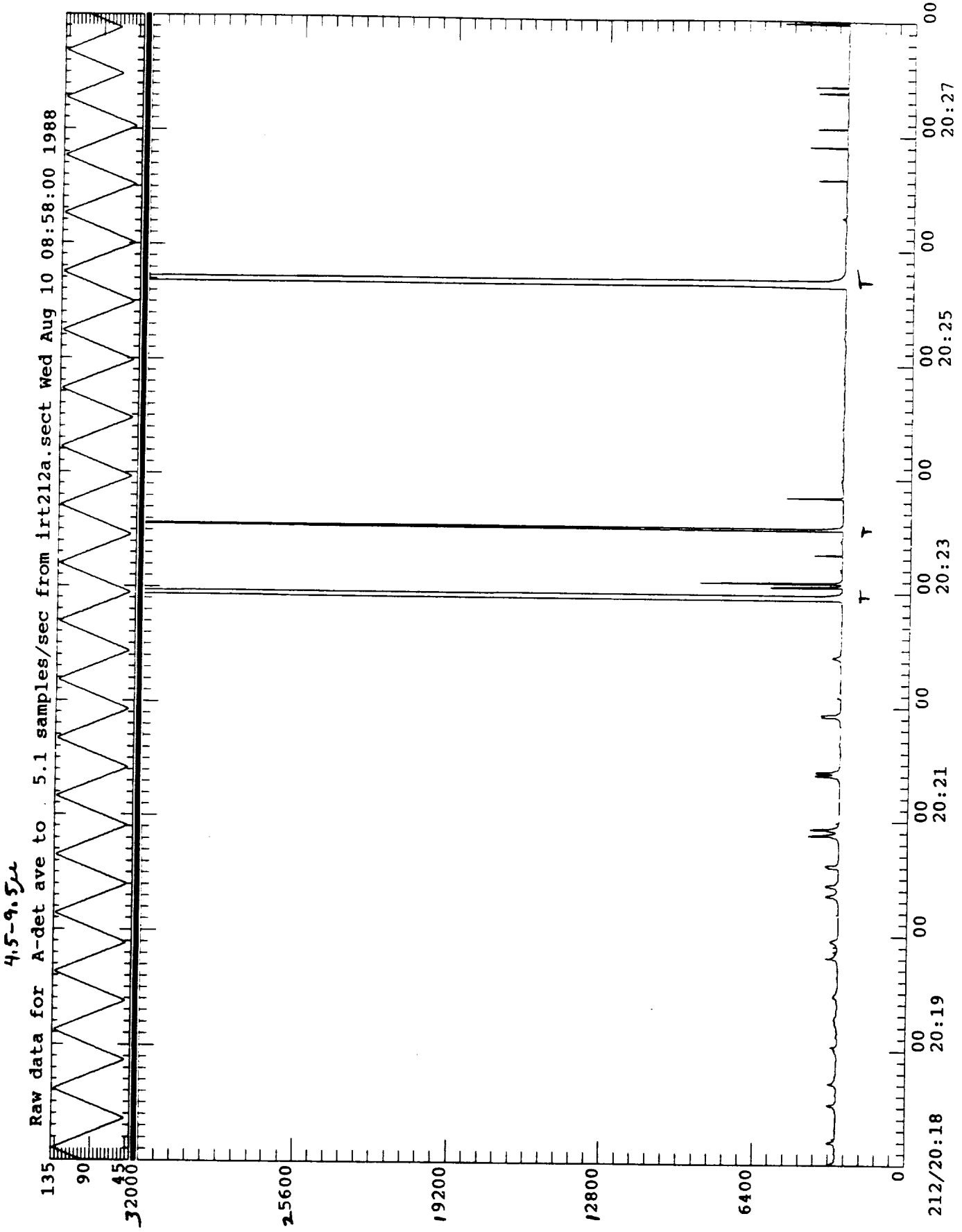
4.5-9.5μ
Raw data for A-det ave to 5.1 samples/sec from irt212a.sect Wed Aug 10 08:58:00 1988
135
90
45
0
32000
25600
19200
12800
6400
0
212/20:18
20:19
20:21
20:23
20:25
20:27

Figure B-14

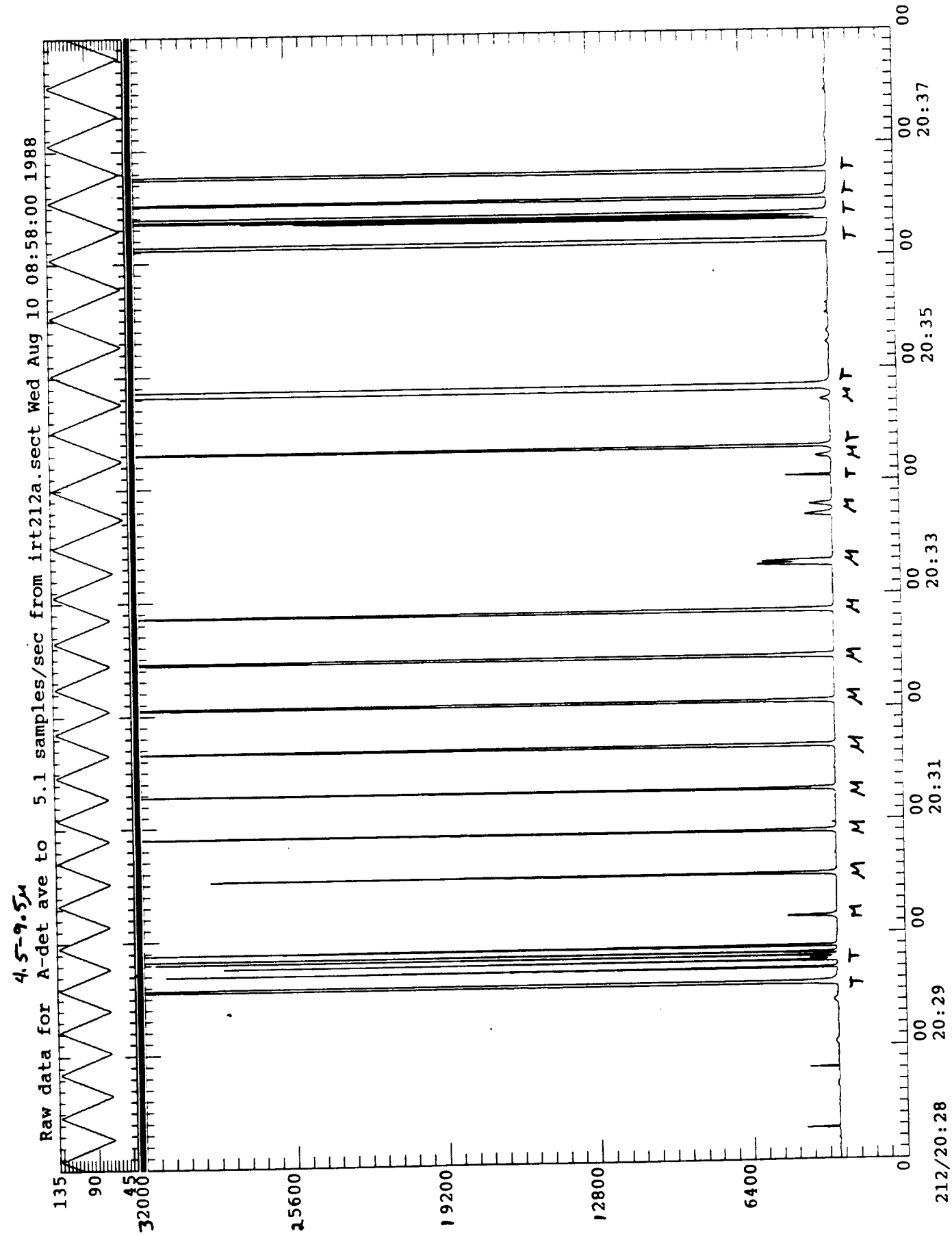
4.5-9.5μ
Raw data for A-det ave to 5.1 samples/sec from irt212a.sect Wed Aug 10 08:58:00 1988
135
90
45
32000
25600
19200
12800
6400
0
212/20:28
20:29
20:31
20:33
20:35
20:37

Figure B-15

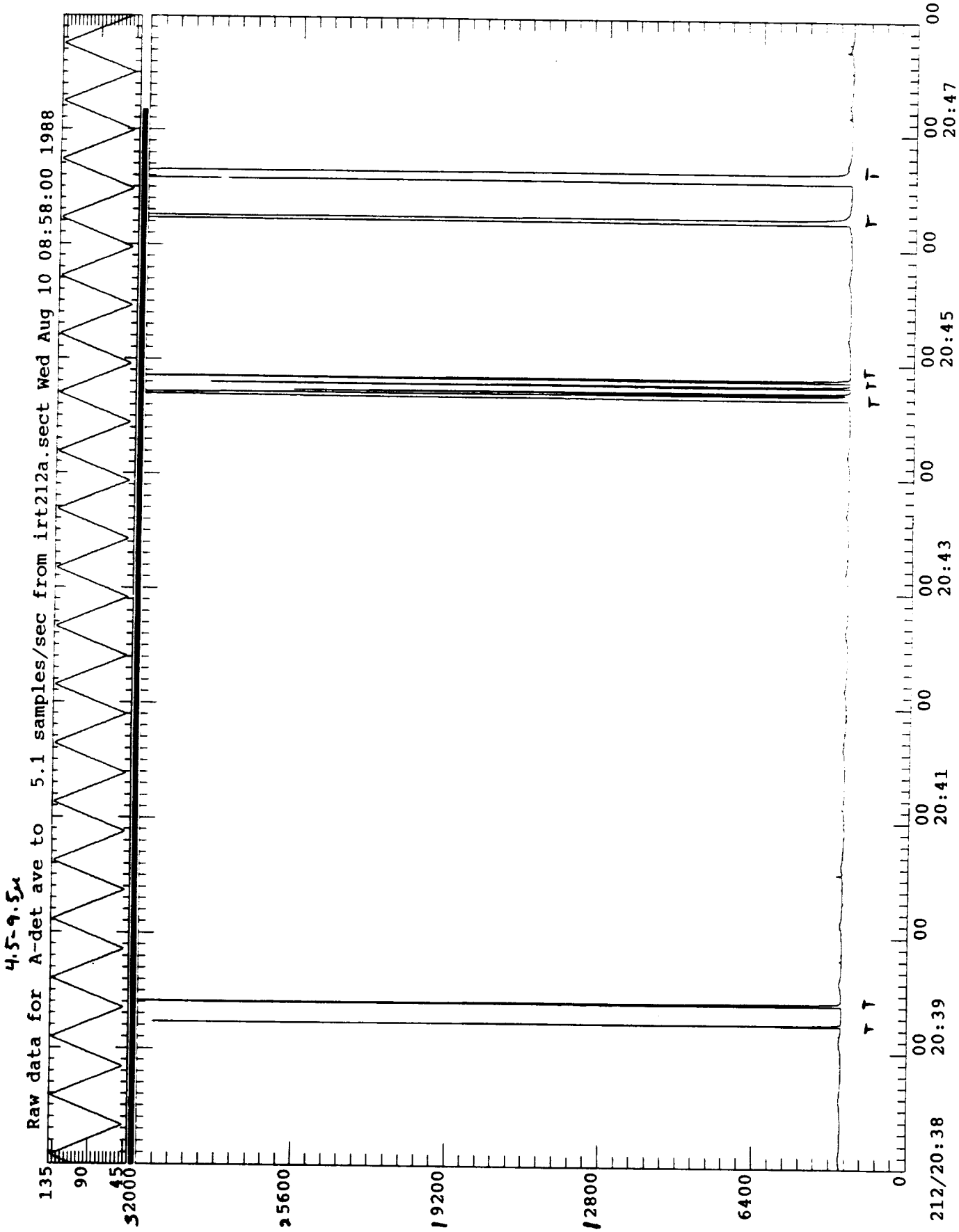
4.5-9.5μ
Raw data for A-det ave to 5.1 samples/sec from irt212a.sect Wed Aug 10 08:58:00 1988
135
90
45
0
32000
25600
19200
12800
6400
0
212/20:38
00
20:39
00
20:41
00
20:43
00
20:45
00
20:47
00

Figure B-16

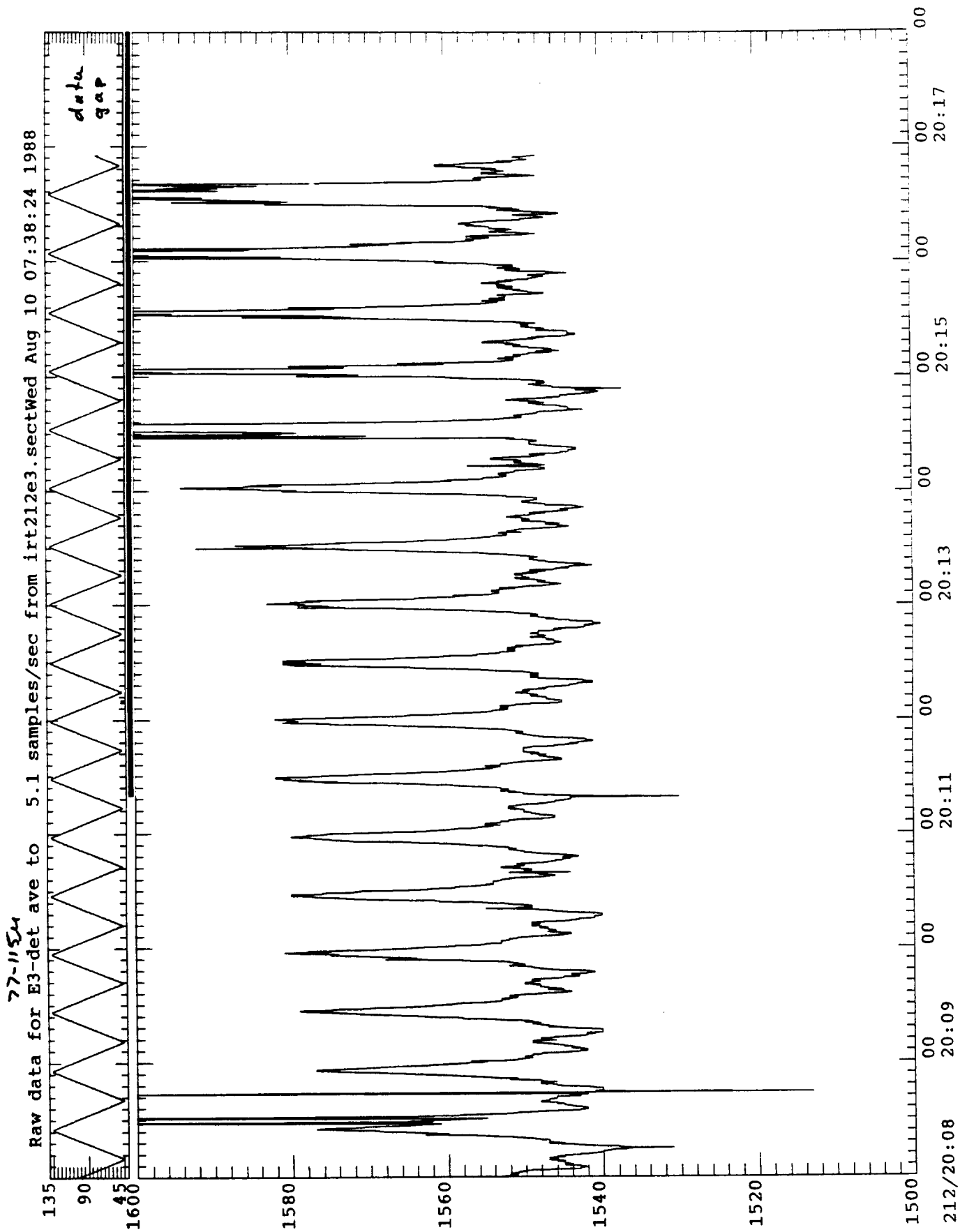
77-115m
Raw data for E3-det ave to 5.1 samples/sec from irt212e3.sectWed Aug 10 07:38:24 1988
data gap
135
90
45
1600
1580
1560
1540
1520
1500
212/20:08
00
20:09
00
20:11
00
20:13
00
20:15
00
20:17
00

Figure B-17

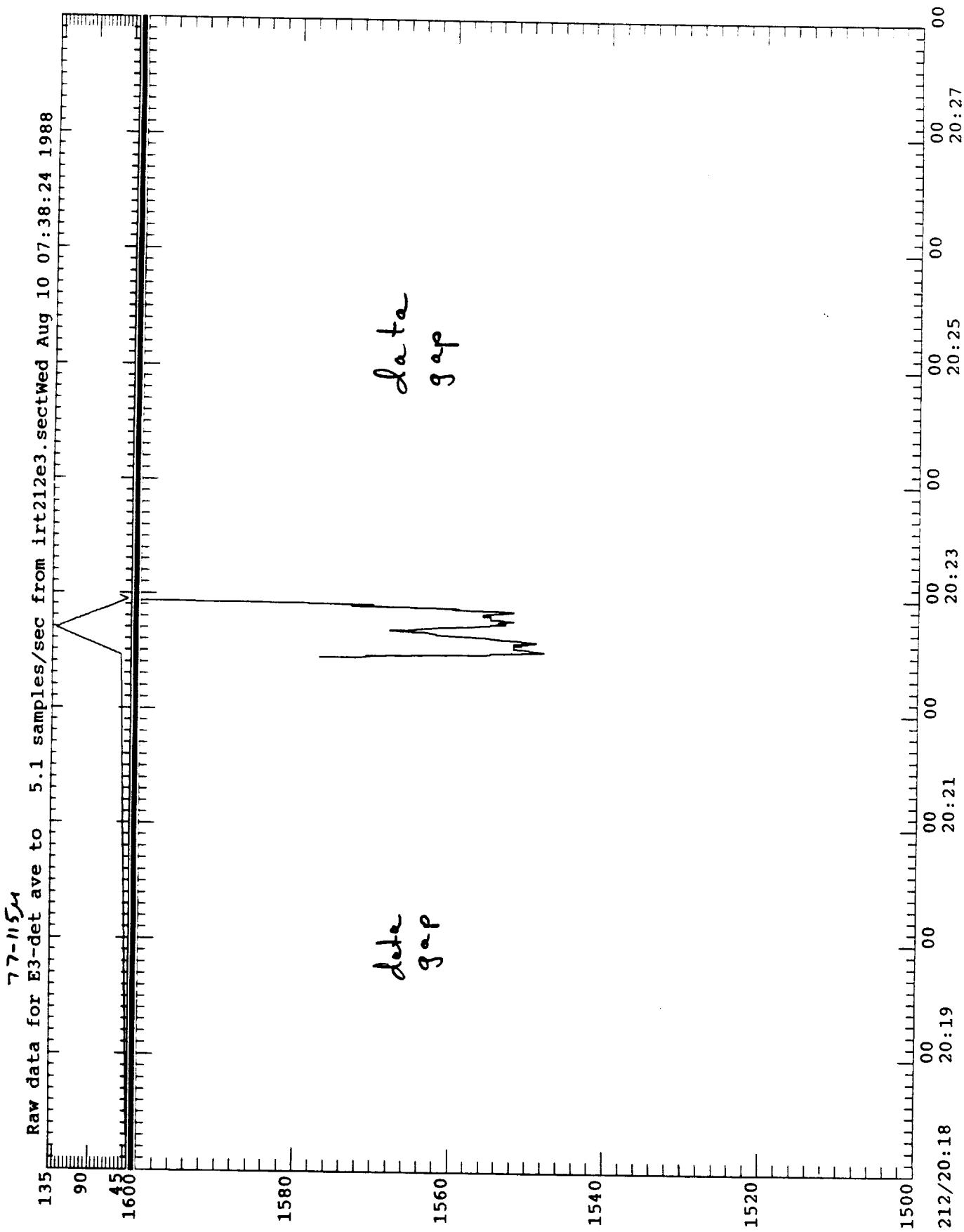
77-115m
Raw data for E3-det ave to 5.1 samples/sec from irt212e3.sectWed Aug 10 07:38:24 1988
135
90
45
1600
1580
1560
1540
1520
1500
212/20:18
00
20:19
00
20:21
00
20:23
00
20:25
00
20:27
data gap
data gap

Figure B-18

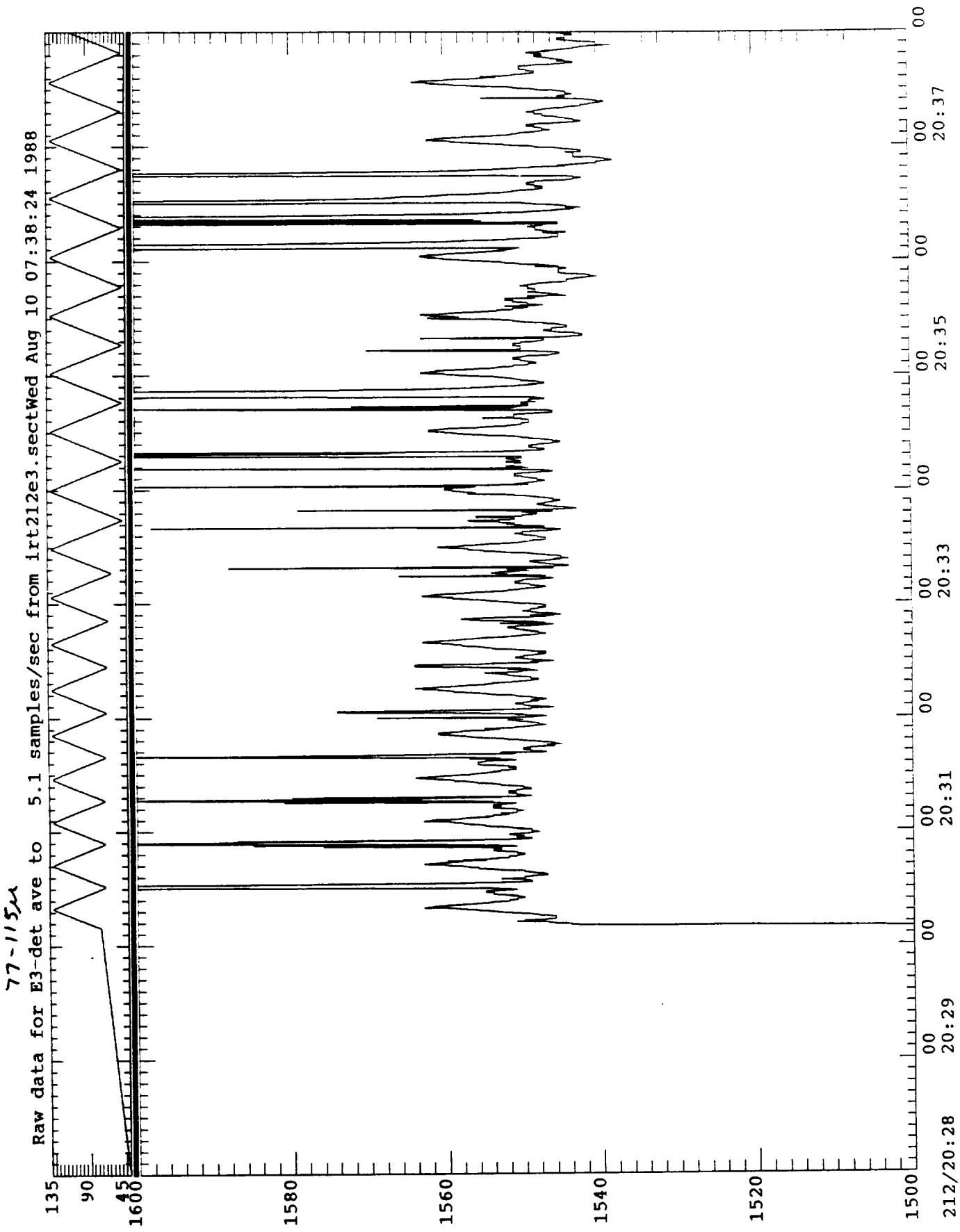
77-115m
Raw data for E3-det ave to 5.1 samples/sec from irt212e3.sectWed Aug 10 07:38:24 1988
135
90
45
1600
1580
1560
1540
1520
1500
212/20:28
00
20:29
00
20:31
00
20:33
00
20:35
00
20:37
00

Figure B-19

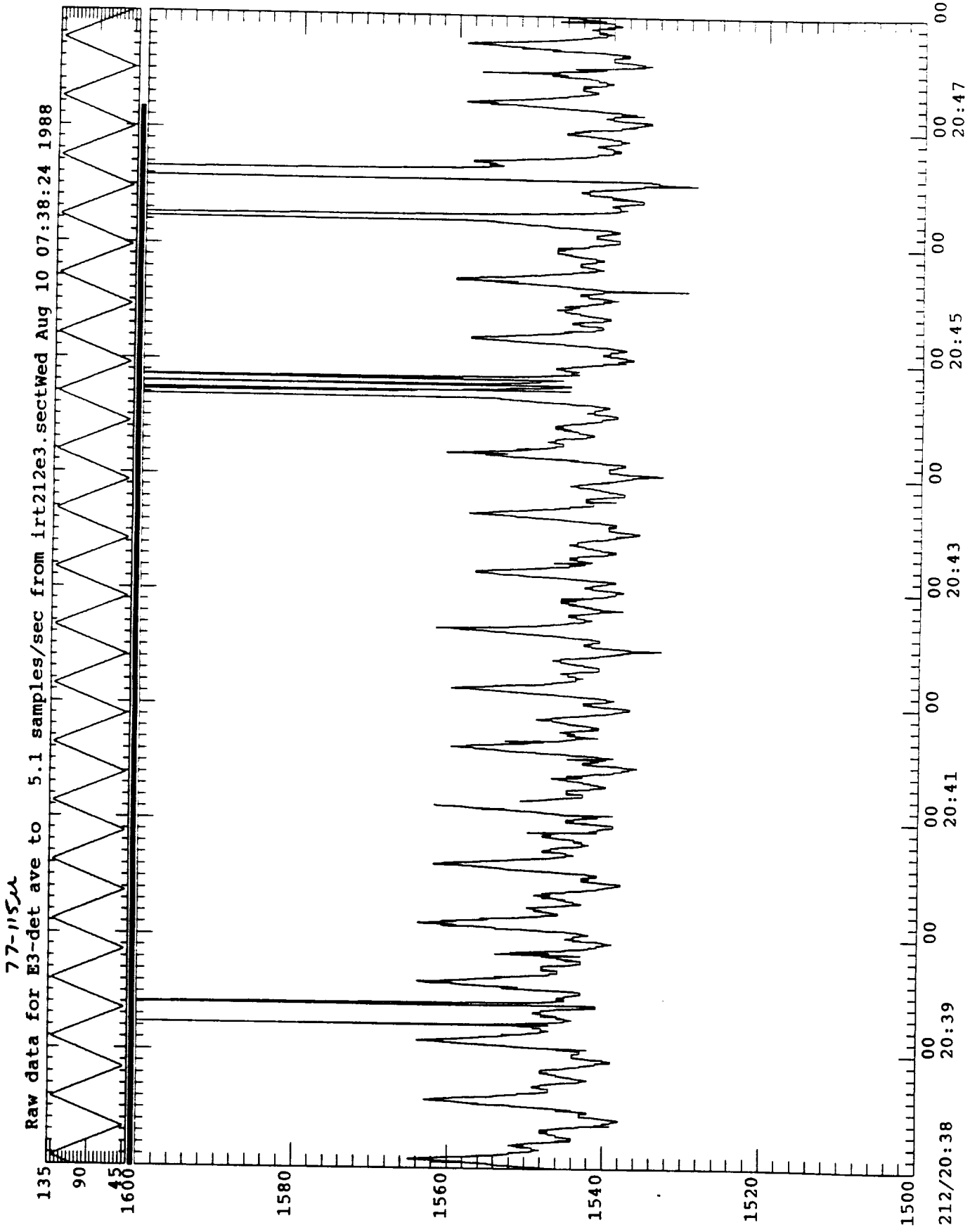
77-115m
Raw data for E3-det ave to 5.1 samples/sec from irt212e3.sectWed Aug 10 07:38:24 1988
135
90
45
0
1600
1580
1560
1540
1520
1500
212/20:38
00
20:39
00
20:41
00
20:43
00
20:45
00
20:47
00

Figure B-20

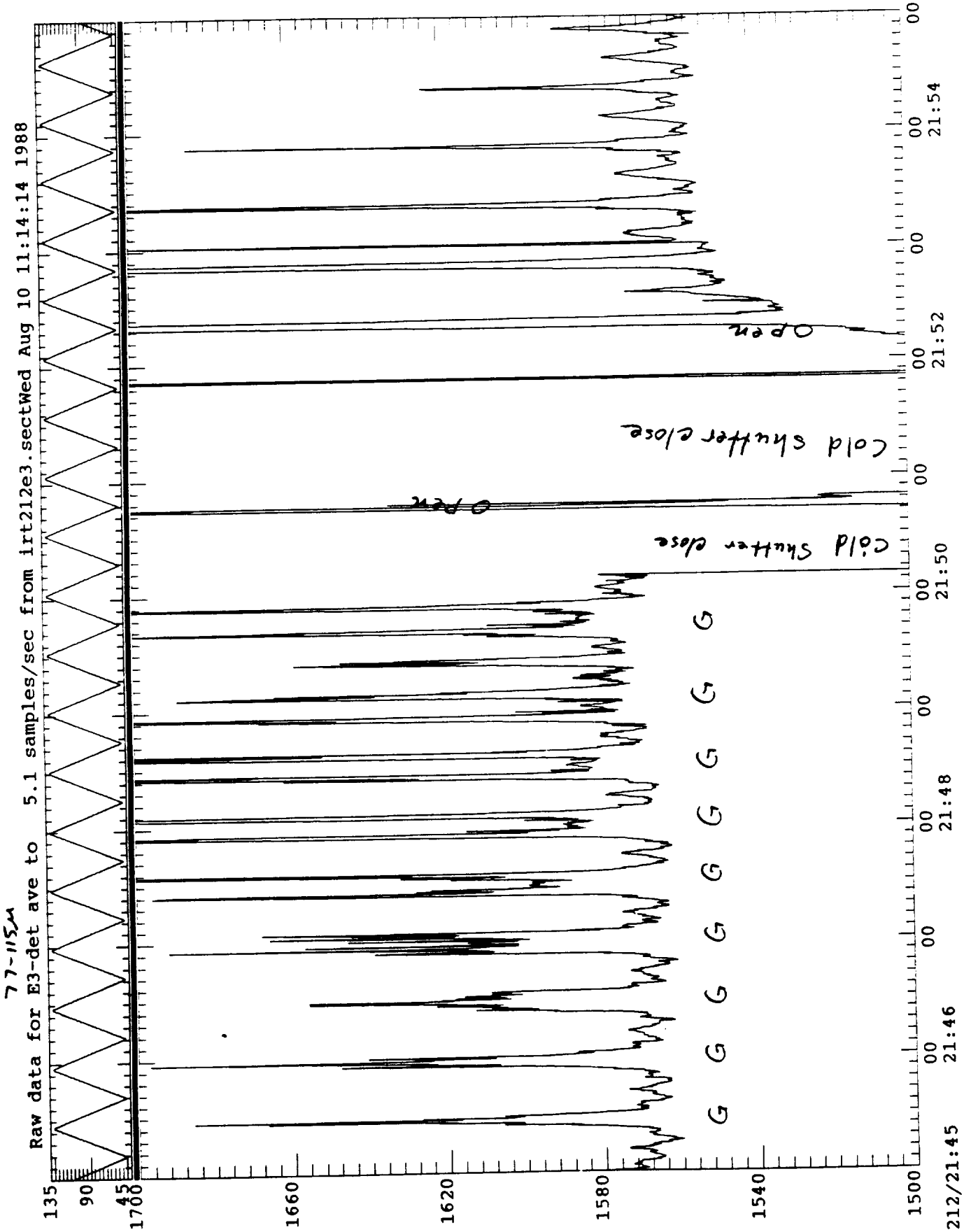
77-115m
Raw data for E3-det ave to 5.1 samples/sec from irt212e3.sectWed Aug 10 11:14:14 1988
135
90
45
1700
1660
1620
1580
1540
1500
212/21:45
21:46
21:48
21:50
21:52
21:54
Cold Shutter close
Open
Cold Shutter close
Open
G G G G G G G G G G

Figure B-21

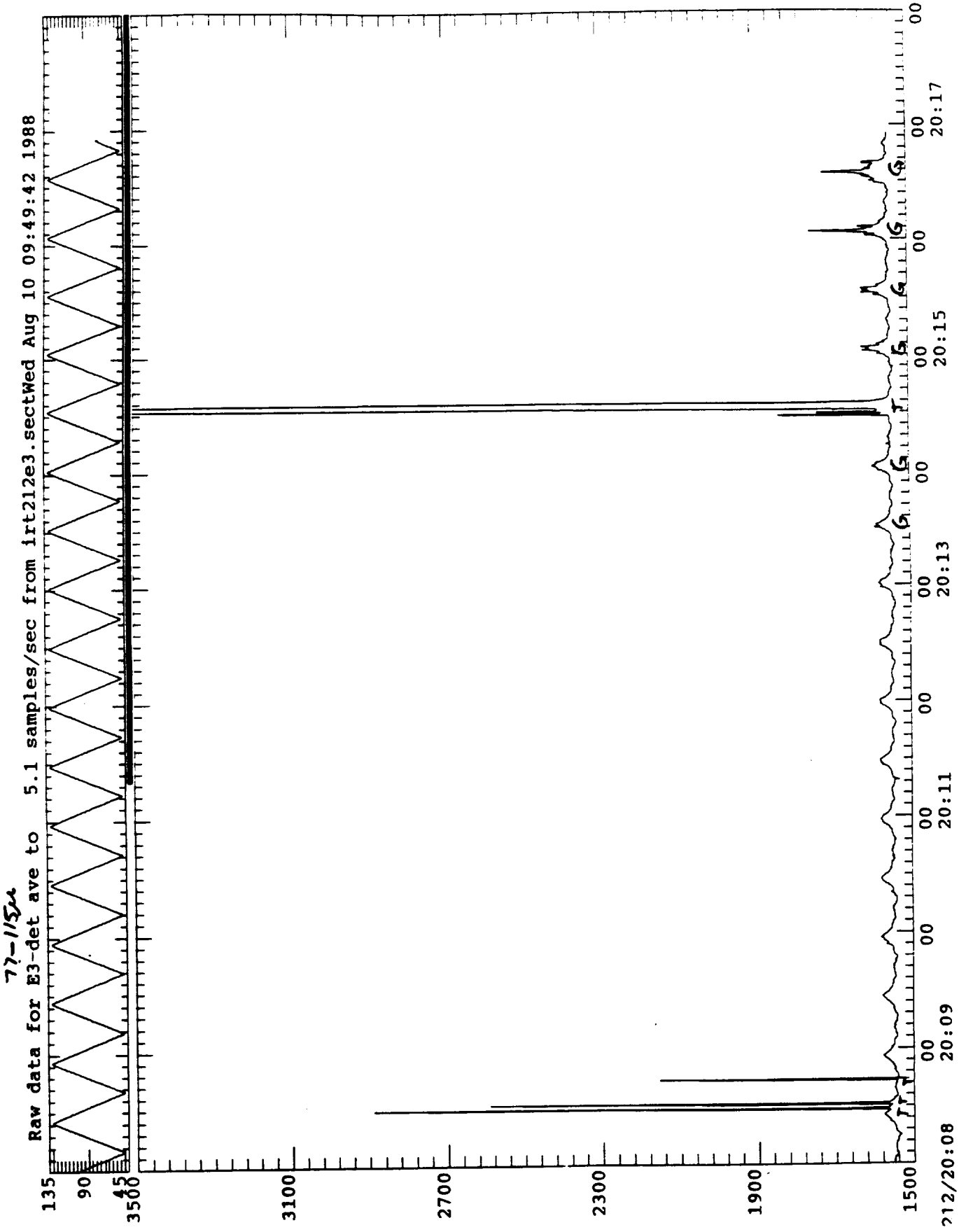
77-115a
Raw data for E3-det ave to 5.1 samples/sec from irt212e3.sectWed Aug 10 09:49:42 1988
135
90
45
3500
3100
2700
2300
1900
1500
212/20:08
20:09
20:11
20:13
20:15
20:17

Figure B-22

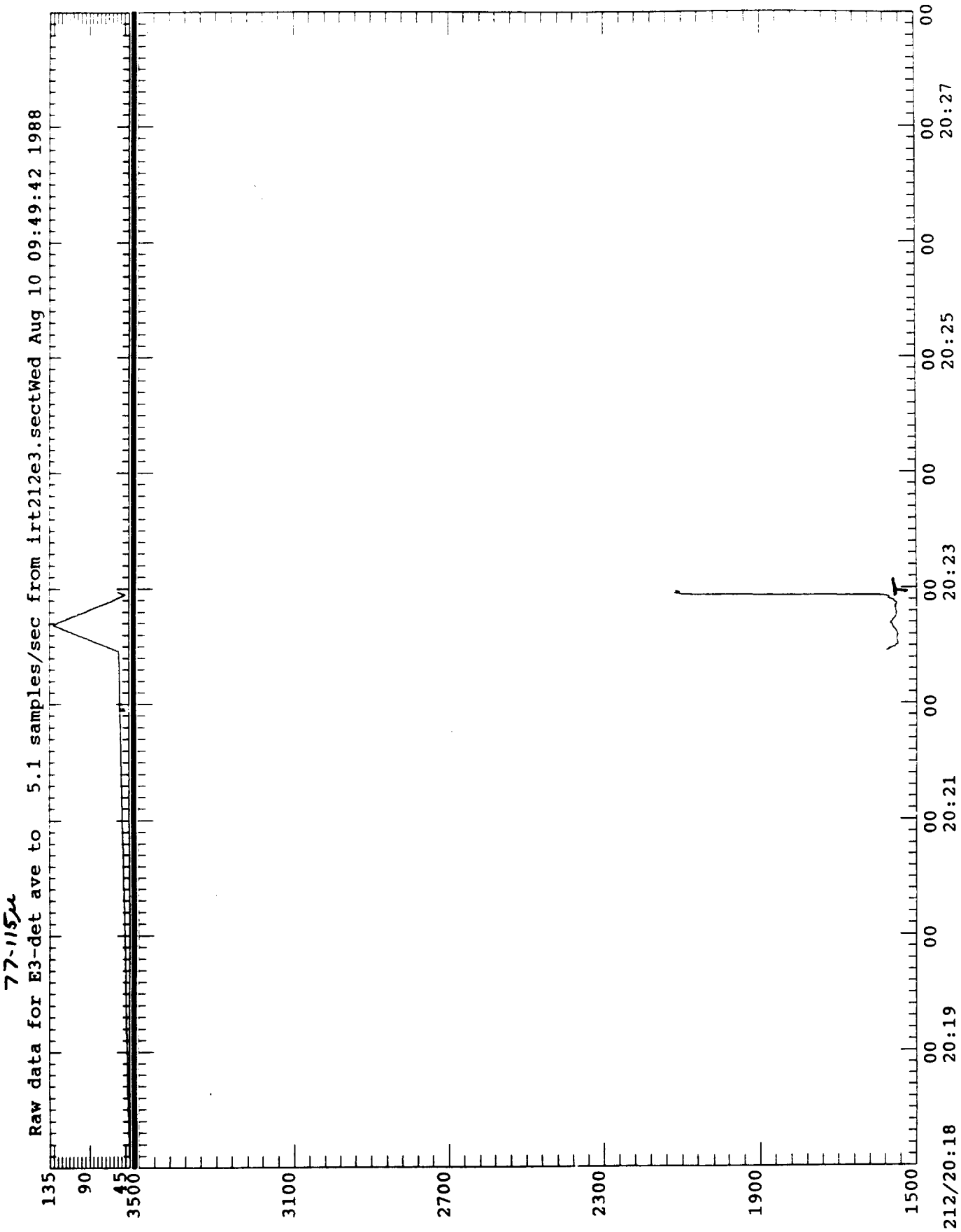
77-115m
Raw data for E3-det ave to 5.1 samples/sec from irt212e3.sectWed Aug 10 09:49:42 1988
135
90
45
3500
3100
2700
2300
1900
1500
212/20:18
00
20:19
00
20:21
00
20:23
00
20:25
00
20:27
00

Figure B-23

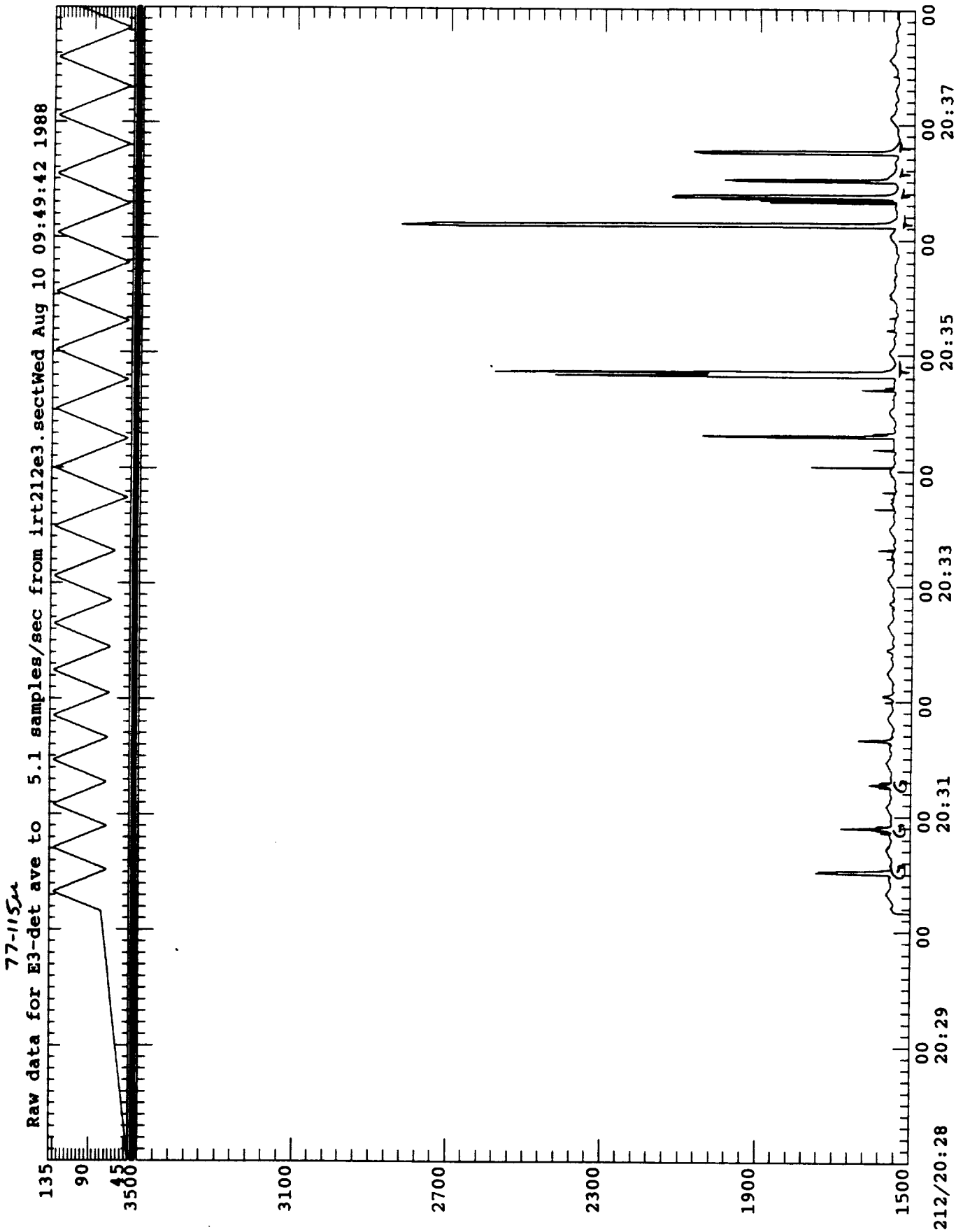
77-115m
Raw data for E3-det ave to 5.1 samples/sec from irt212e3.sectWed Aug 10 09:49:42 1988
135
90
45
3500
3100
2700
2300
1900
1500
212/20:28
00
20:29
00
20:31
00
20:33
00
20:35
00
20:37
00

Figure B-24

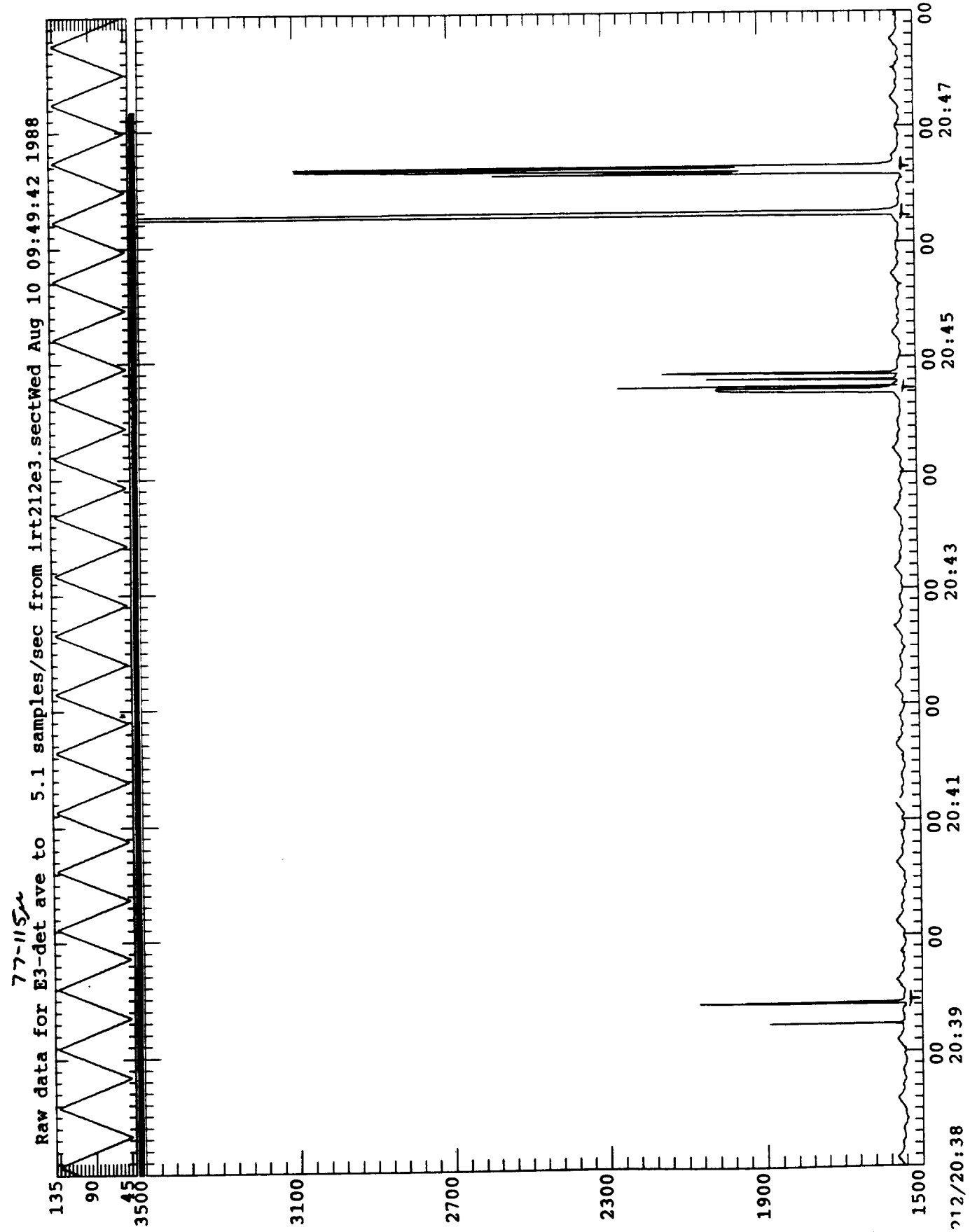
77-115m
Raw data for E3-det ave to 5.1 samples/sec from irt212e3.sectWed Aug 10 09:49:42 1988
135
90
45
3500
3100
2700
2300
1900
1500
00
20:47
00
20:45
00
20:43
00
20:41
00
20:39
212/20:38

Figure B-25

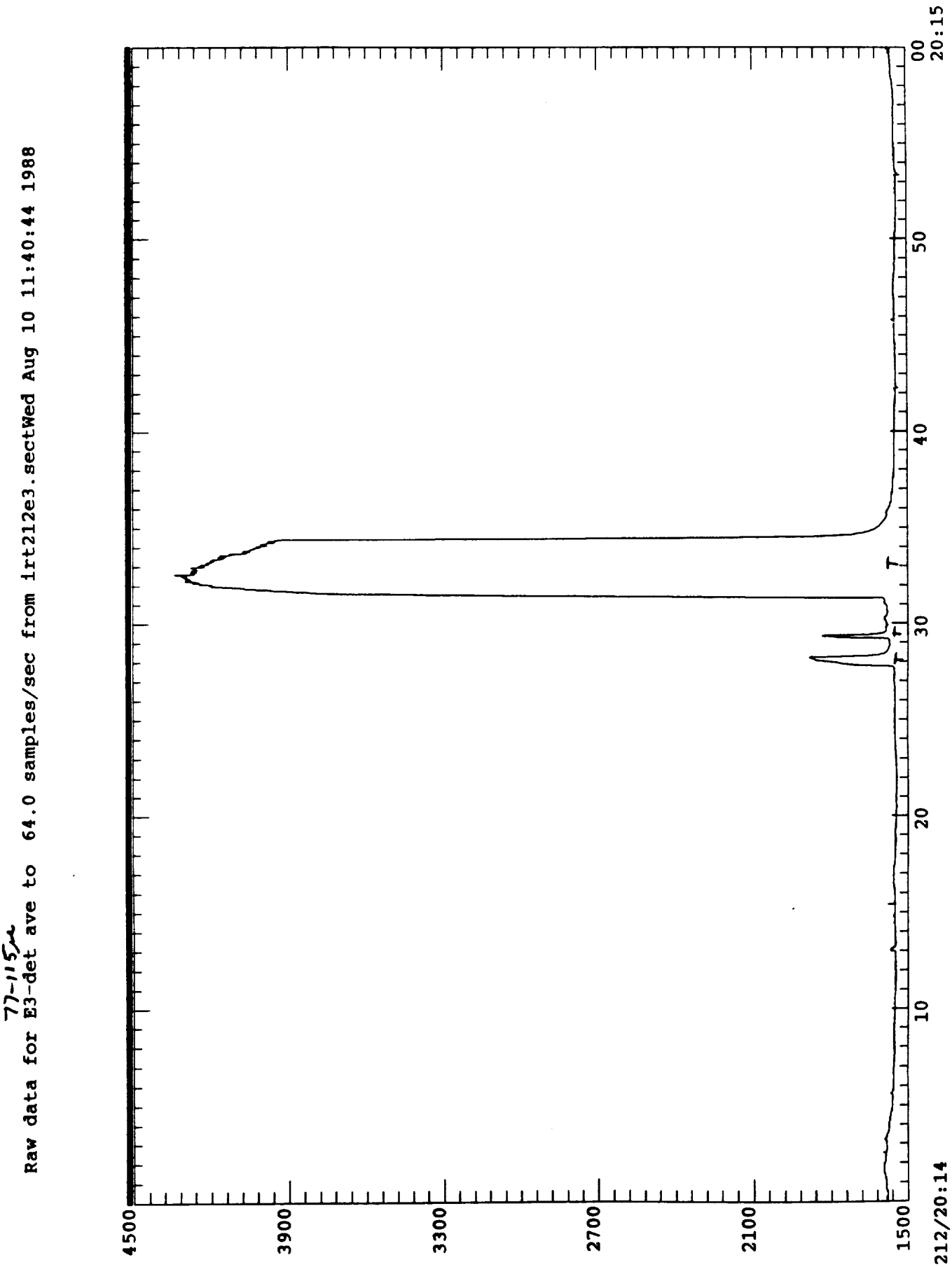
77-115m
Raw data for E3-det ave to 64.0 samples/sec from 1rt212e3.sectWed Aug 10 11:40:44 1988
4500
3900
3300
2700
2100
1500
212/20:14
10
20
30
40
50
00
20:15

Figure B-26

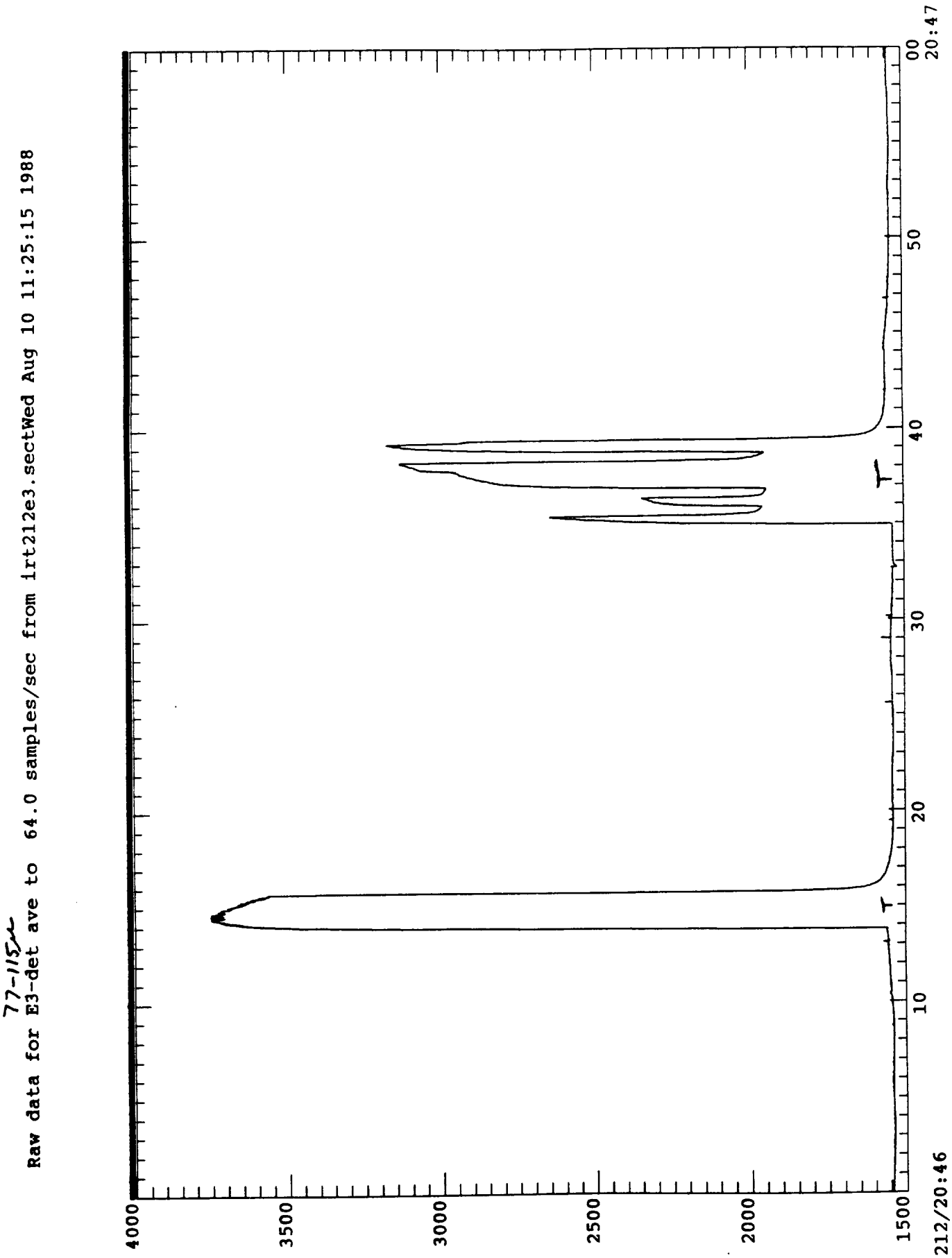
77-115m
Raw data for E3-det ave to 64.0 samples/sec from 1rt212e3.sectWed Aug 10 11:25:15 1988
4000
3500
3000
2500
2000
1500
212/20:46
00
20:47
50
40
30
20
10
T
T

Figure B-27

IRT det. 2: S 2-3 microns (N-slit)
Data file "irt212s.filt"

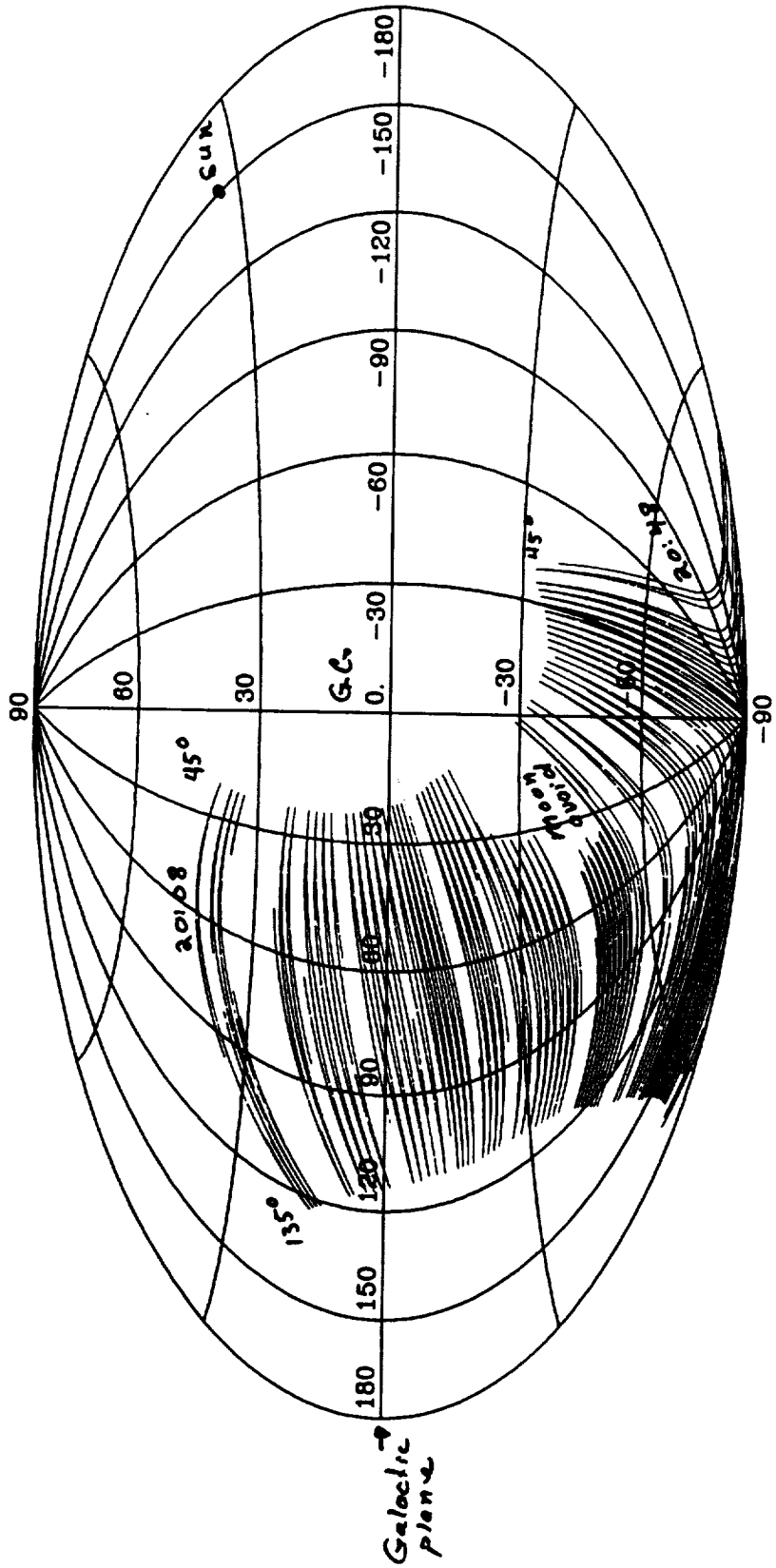

Figure B-28

PREPARATION OF THE REPORT DOCUMENTATION PAGE

The last page of a report facing the third cover is the Report Documentation Page, RDP. Information presented on this page is used in announcing and cataloging reports as well as preparing the cover and title page. Thus it is important that the information be correct. Instructions for filling in each block of the form are as follows:

Block 1. Report No. NASA report series number, if preassigned.

Block 2. Government Accession No. Leave blank.

Block 3. Recipient's Catalog No. Reserved for use by each report recipient.

Block 4. Title and Subtitle. Typed in caps and lower case with dash or period separating subtitle from title.

Block 5. Report Date. Approximate month and year the report will be published.

Block 6. Performing Organization Code. Leave blank.

Block 7. Author(s). Provide full names exactly as they are to appear on the title page. If applicable, the word editor should follow a name.

Block 8. Performing Organization Report No. NASA installation report control number and, if desired, the non-NASA performing organization report control number.

Block 9. Performing Organization Name and Address. Provide affiliation (NASA program office, NASA installation, or contractor name) of authors.

Block 10. Work Unit No. Provide Research and Technology Objectives and Plans (RTOP) number.

Block 11. Contract or Grant No. Provide when applicable.

Block 12. Sponsoring Agency Name and Address. National Aeronautics and Space Administration, Washington, D.C. 20546-0001. If contractor report, add NASA installation or HQ program office.

Block 13. Type of Report and Period Covered. NASA formal report series; for Contractor Report also list type (interim, final) and period covered when applicable.

Block 14. Sponsoring Agency Code. Leave blank.

Block 15. Supplementary Notes. Information not included elsewhere: affiliation of authors if additional space is required for block 9, notice of work sponsored by another agency, monitor of contract, information about supplements (film, data tapes, etc.), meeting site and date for presented papers, journal to which an article has been submitted, note of a report made from a thesis, appendix by author other than shown in block 7.

Block 16. Abstract. The abstract should be informative rather than descriptive and should state the objectives of the investigation, the methods employed (e.g., simulation, experiment, or remote sensing), the results obtained, and the conclusions reached.

Block 17. Key Words. Identifying words or phrases to be used in cataloging the report.

Block 18. Distribution Statement. Indicate whether report is available to public or not. If not to be controlled, use "Unclassified-Unlimited." If controlled availability is required, list the category approved on the Document Availability Authorization Form (see NHB 2200.2, Form FF427). Also specify subject category (see "Table of Contents" in a current issue of STAR), in which report is to be distributed.

Block 19. Security Classification (of this report). Self-explanatory.

Block 20. Security Classification (of this page). Self-explanatory.

Block 21. No. of Pages. Count front matter pages beginning with iii, text pages including internal blank pages, and the RDP, but not the title page or the back of the title page.

Block 22. Price Code. If block 18 shows "Unclassified-Unlimited," provide the NTIS price code (see "NTIS Price Schedules" in a current issue of STAR) and at the bottom of the form add either "For sale by the National Technical Information Service, Springfield, VA 22161-2171" or "For sale by the Superintendent of Documents, U.S. Government Printing Office, Washington, DC 20402-0001," whichever is appropriate.

NASA National Aeronautics and Space Administration

Report Documentation Page

1. Report No.	2. Government Accession No.	3. Recipient's Catalog No.

4. Title and Subtitle

Small Helium-Cooled Infrared Telescope Experiment for Spacelab-2 -- Final Report

5. Report Date

March 1990

6. Performing Organization Code

7. Author(s)

Dr. Giovanni G. Fazio, Principal Investigator

8. Performing Organization Report No.

10. Work Unit No.

9. Performing Organization Name and Address

Smithsonian Astrophysical Observatory
60 Garden Street
Cambridge, Massachusetts 02138

11. Contract or Grant No.

NAS8-32845

13. Type of Report and Period Covered

Final
10/3/77 - 12/31/88

12. Sponsoring Agency Name and Address

National Aeronautics and Space Administration
Washington, D.C. 20546-0001

NASA Marshall Space Flight Center

14. Sponsoring Agency Code

15. Supplementary Notes

NASA Technical Officer is Tom R. Smith, JA53, NASA Marshall Space Flight Center, Huntsville, Alabama.

16. Abstract The Infrared Telescope (IRT) experiment, flown on Spacelab-2 in July/August 1985, was used to make infrared measurements between 2 μm and 120 μm. The objectives were multidisciplinary in nature with astrophysical goals of mapping the diffuse cosmic emission and extended infrared sources and technical goals of measuring the induced Shuttle environment, studying properties of superfluid helium in space, and testing various infrared telescope system designs.

Astrophysically, new data were obtained on the structure of the Galaxy at near-infrared wavelengths. A summary of the large-scale diffuse near-infrared observations of the Galaxy by the IRT is presented, as well as a summary of the preliminary results obtained from this data on the structure of the galactic disk and bulge. The importance of combining CO and near-infrared maps of similar resolution to determine a three-dimensional model of galactic extinction is demonstrated. The IRT data are used, in conjunction with a proposed galactic model, to make preliminary measurements of the global scale parameters of the Galaxy.

During the mission substantial amounts of data were obtained concerning the induced Shuttle environment. An experiment was also performed to measure space-craft glow in the IR.

17. Key Words (Suggested by Author(s))

infrared astronomy, space shuttle environment, superfluid helium in space, diffuse cosmic radiation, Spacelab-2, galactic structure, infrared telescope in space, spacecraft glow

18. Distribution Statement

Unclassified - Unlimited

19. Security Classif. (of this report)	20. Security Classif. (of this page)	21. No. of pages	22. Price
N/A	N/A	166	N/A